Chem Soc Rev

The Charge Carrier Dynamics, Efficiency and Stability of Two-Dimensional Material-Based Perovskite Solar Cells

Journal:	*Chemical Society Reviews*
Manuscript ID	CS-REV-04-2019-000254.R1
Article Type:	Review Article
Date Submitted by the Author:	30-Jun-2019
Complete List of Authors:	Wang, Bing; Nanjing University, Iocozzia, James; Georgia Institute of Technology, Materials Science and Engineering Zhang, Meng; Georgia Institute of Technology, Materials Science and Engineering Ye, Meidan; Xiamen University, Research Institute for Soft Matter and Biomimetics, School of Physics and Mechanical & Electrical Engineering Yan, Shi Cheng; Nanjing University, College of Engineering and Applied Sciences Jin, Huile; Wenzhou University, College of Chemistry and Materials Engineering wang, shun; Wenzhou University, Zou, Zhigang; Nanjing University, Physics Lin, Zhiqun; Georgia Institute of Technology, Materials Science and Engineering

The Charge Carrier Dynamics, Efficiency and Stability of Two-Dimensional Material-Based Perovskite Solar Cells

Bing Wang[†], James Iocozzia[†], Meng Zhang[†], Meidan Ye[‡], Shicheng Yan[§], Huile Jin,[#] Shun Wang,[*#] Zhigang Zou[*§], and Zhiqun Lin[*†]

† School of Materials Science and Engineering, Georgia Institute of Technology, Atlanta GA 30332, USA. E-mail: zhiqun.lin@mse.gatech.edu.

‡ Department of Physics, School of Physics and Mechanical and Electrical Engineering, Research Institute for Soft Matter and Biomimetics, Xiamen University, Xiamen 361005, People's Republic of China.

§ Eco-materials and Renewable Energy Research Center, National Laboratory of Solid State Microstructures, College of Engineering and Applied Sciences, Nanjing University, Nanjing 210093, People's Republic of China. E-mail: zgzou@nju.edu.cn.

College of Chemistry and Materials Engineering, Wenzhou University, Wenzhou 325035, PR China. E-mail: shunwang@wzu.edu.cn

Abstract

Perovskites have been firmly established as one of the most promising materials for third-generation solar cells. There remain several great and lingering challenges to be addressed regarding device efficiency and stability. The photovoltaic efficiency of perovskite solar cells (PSCs) depends drastically on the charge-carrier dynamics. This complex process includes charge-carrier generation, extraction, transport and collection, each of which needs to be modulated in a favorable manner to achieve high performance. Two-dimensional materials (TDMs) including graphene and its derivatives, transition metal dichalcogenides (e.g. MoS_2, WS_2), black phosphorus (BP), metal nanosheets and two-dimensional (2D) perovskite active layers have attracted much attention for applications in perovskite solar cells due to their high carrier mobility and tunable work function properties which greatly impact the charge carrier dynamics of PSCs. To date, significant advances have been achieved for TDMs-based PSCs. In this review, the recent progress in the development and application of TDMs (i.e., graphene, graphdiyne, transition metal dichalcogenides, BP, and others) as electrodes, hole transporting layers, electron transporting layers and buffer layers in PSCs is detailed. 2D perovskites as active absorber materials in PSCs are also summarized. The effect of TDMs and 2D perovskites on the charge carrier dynamics of PSCs is discussed to provide a comprehensive understanding of their optoelectronic processes. The challenges facing the PSC devices are emphasized with corresponding solutions to these problems provided with the overall goal of improving the efficiency and stability of photovoltaic devices.

1. Introduction

Photovoltaic solar cells can convert energy from the sun into direct current electricity using the photovoltaic effect. Such devices have been regarded as a very promising energy generation source and attracted much attention from the academic community. Several photovoltaic solar cells have helped to shape the environment of renewable sources of energy, including silicon solar cells, III-V solar cells, quantum dot-sensitized solar cells, dye-sensitized solar cells, organic solar cells and perovskite solar cells (PSCs). Crystalline silicon is nontoxic and abundantly available, and allows for the fabrication of solar cells with up to 27% conversion efficiencies with negligible degradation. For these reasons, it has been the long term market leader. However, this mature technology is constrained by some fundamental drawbacks, such as high temperature and energy intensive manufacturing processes, and a relatively large global demand for Si. The effectiveness of crystalline solar cells depends strongly on their continuous structure with minimal grain boundaries to facilitate the movement of photo-generated carriers. The main commercial motivation for developing highly efficient photovoltaic solar cells is to reduce production costs and produce high-quality semiconductors. PSCs have rapidly emerged as one such candidate. The development of PSCs is on its way to challenging the dominance of polycrystalline silicon and other thin film technologies. High power conversion efficiencies can be achieved by simple low cost processing.[1]

The term “perovskite” is used to describe compounds with the formula ABO_3, in which A denotes the larger atom (cuboctahedral coordination), B denotes the smaller atoms. In general, A and B are two cations while O is an anion that bonds to both. The coordination

may deviate from ideal due to the differences in the atomic radii of the constituents. This deviation from ideality is defined by the Goldschmidt tolerance factor (*t*). The Goldschmidt tolerance factor can predict the stability and distortion of the crystal structure of ABO_3 perovskite materials and is defined by the expression $t = (r_A + r_O) / [\sqrt{2}(r_B + r_O)]$, where r_A, r_B, and r_O are the ionic radii of A, B, and O, respectively.[2] Distortions from the cubic structure can arise from a size-mismatch of the ions resulting in additional perovskite structures, such as layered two-dimensional (2D) perovskites.[3, 4] The Ruddlesden-Popper (RP) phase is a form of layered perovskite structure which consists of 2D perovskite slabs interlayered with cations. The general formula of the RP phase can be written as $A_{n+1}B_nO_{3n+1}$ (with $n \geqslant 1$ representing the number of connected layers of vertex-sharing BO_6 octahedra).[3, 5] The layer thickness of $A_{n+1}B_nO_{3n+1}$ increases as n rises. Perovskites are a 2D material at low n value. As n increases, structural gradients from 2D to 3D perovskites coexist.[6] When $n=\infty$, perovskites turn into a pure 3D form. **Figure 1** shows the ideal tetragonal unit cells for n = 1, 2, and 3 of RP-type 2D perovskites. Compared to typical three-dimensional (3D) ABO_3 perovskites, 2D perovskites have attracted a great deal of attention in recent years due to their combination of an advantageous 2D shape for facilitating charge carrier migration and perovskite composition possessing intrinsic photovoltaic properties.[7] Similar to conventional two-dimensional materials (TDMs), 2D perovskites can be assembled into uniform and ultrathin flexible films with highly oriented microstructures.[8] Layered perovskites can be grown in different forms by tailoring the alignment of crystallographic planes of their 2D slabs.[9] They also have long charge carrier diffusion lengths，high quantum yields, high light absorption coefficients, and low rates of non-radiative charge recombination inherited from

3D perovskites.[10] Unlike 3D perovskites, 2D perovskites have tunable photoelectric properties and excellent environmental stability.[11] Solar cells based on layered 2D perovskites are detailed in this review.

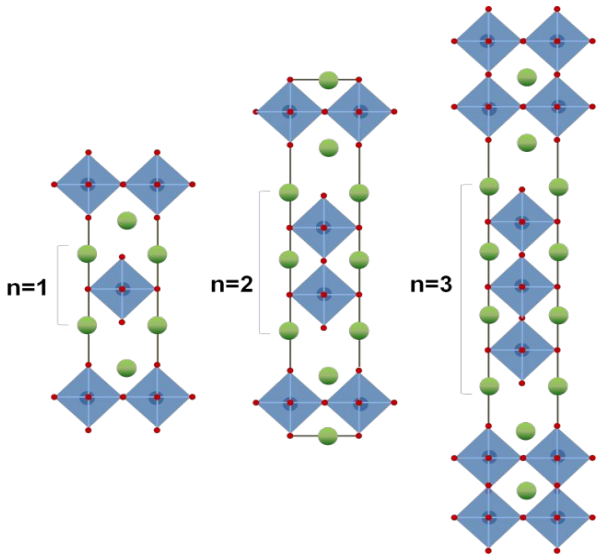

Figure 1. The ideal Ruddlesden–Popper-type perovskite structure, $A_{n+1}B_nO_{3n+1}$ (n = 1, 2, 3; A atoms are the green balls, B atoms are the blue balls in the center of each octahedron, and O atoms are the red balls at the ends of each octahedron).

Organic-inorganic metal halide perovskites are a class of compounds in the perovskite family with alternating layered structures of organic and inorganic constituents. Methylammonium lead iodide ($CH_3NH_3PbI_3$, or $MAPbI_3$) is one of the most common materials. This consists of a large organic cation, methylammonium ($CH_3NH_3^+$), lead (Pb) as the smaller cation and iodine as the halogen anion. This structure was first used in solar cells by Miyasaka et al. in 2009.[12] $CH_3NH_3PbX_3$ (X = Br, I) perovskite materials adsorbed on mesoporous TiO_2 were applied as a sensitizer in a dye-sensitized solar cell (DSSC) with a liquid electrolyte. Initially, $MAPbI_3$ dyes produced efficiencies around 3.8%.[12] However,

liquid electrolytes often contain volatile and corrosive components which often leak within the device and reduce the lifetime of solar cells. In 2012, Park et al. used perovskite absorbers as the primary photoactive layer to fabricate solid-state meso-superstructured PSCs.[13] Spiro-MeOTAD and mesoporous TiO_2 were employed as the hole and electron transporting layers, respectively. The fabricated solar cell delivered a power conversion efficiency (PCE) of 9.7%.[13] Subsequently, extensive work has been devoted to improving the performance of PSCs by controlling the composition,[14-18] interfacial engineering,[19-22] and optimizing the device architecture.[18, 23-26] These efforts resulted in a maximum reported certified PCE of 24.2%.[27] The general structure of a PSC is composed of a electrode layer, perovskite photoactive layer, and charge transport layers (i.e. a hole transporting layer (HTL) and an electron transporting layer (ETL)). In addition, buffer layers have also be inserted at the interfaces between the perovskite and HTL/ETL or HTL/ETL and electrode layers to improve the performance of PSC devices.[20, 21, 28, 29] Bound electron-hole pairs are generated in the energy conversion process of PSCs. The charge carriers are then separated and shuttled to the corresponding electrode. As perovskites can conduct both electrons and holes,[30] the HTL and ETL layers are not necessary to fabricate a working PSC.[31, 32] However, the use of charge transport layers can enhance the separation of electrons and holes. Most PSCs have adopted a structure in which the active perovskite compound is placed between the HTL and ETL. Depending on the structure, PSCs generally have two types of solid-state device architectures:[33, 34] mesoporous-structured PSCs that incorporate a mesoporous layer or a mesoporous-planar bilayer (p-i-n or n-i-p structure), and planar PSCs (p-i-n or n-i-p structure) in which all layers are planar (**Figure 2).**

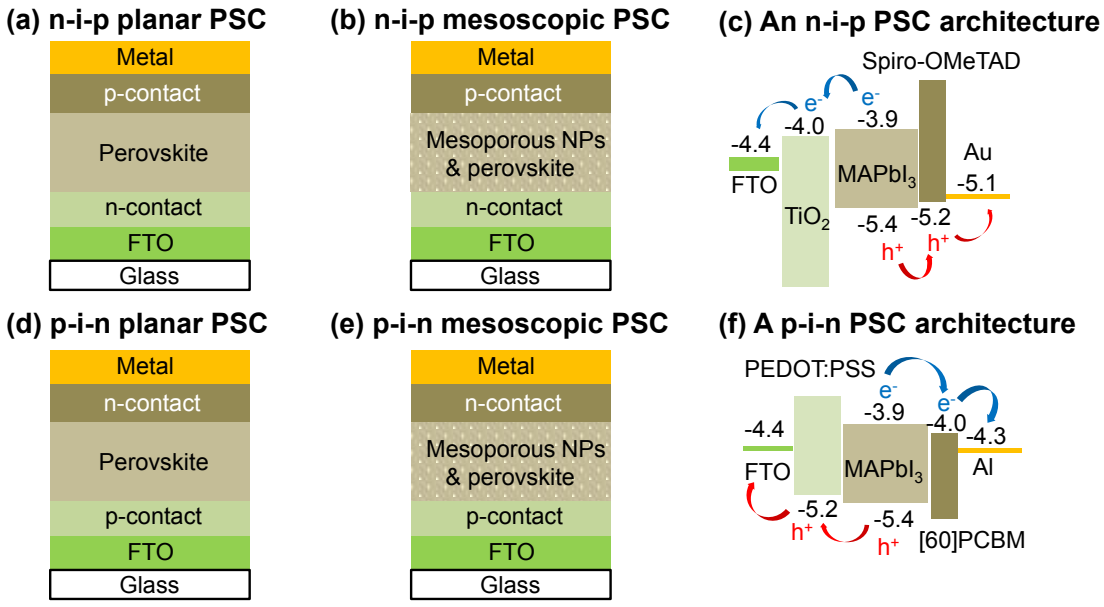

Figure 2. Solid-state device architectures of (a) n-i-p planar and (b) n-i-p mesoscopic PSCs. (c) Energy band diagram of an n-i-p PSC architecture: FTO/TiO_2/$MAPbI_3$/Spiro-OMeTAD/Au. Solid-state device architectures of (d) p-i-n planar and (e) p-i-n mesoscopic PSCs. (f) Energy band diagram of a p-i-n PSC architecture: FTO/PEDOT:PSS/$MAPbI_3$/[60]PCBM/Al. (Note: NPs refers to nanoparticles)

To date, numerous TDMs have been reported, and they can be categorized into groups based on their structural similarities:[35] (1) materials with atomic layers arranged in hexagonal honeycomb lattices, such as graphene,[36] borophene,[37] germanene,[38] hexagonal-boron nitride (h-BN),[39] and black phosphorus (BP);[40] (2) transition metal dichalcogenides[41, 42] with a general stoichiometric formula of MX_2 (where M represents the transition metal and X represents the chalcogen, e.g., MoS_2, $MoSe_2$ and WS_2); and (3) metal oxide nanosheets/nanoplates,[43-48] such as titania nanosheets[45, 46] and ZnO nanoplates.[48] Due to their unique optical and electronic properties (**Table 1**), these TDMs have been widely investigated

for many optoelectronic applications, such as solar cells,[49] photodetectors,[50, 51] and light emitting devices.[52] In the context of PSCs, TDMs have been extensively explored as functional interlayers in different device architectures. In typical PSCs, the undesirable recombination of electrons and holes usually occurs during the charge transport process in which electrons in the perovskite layer recombine with holes in the HTL, and electrons in ETL recombine with holes in the perovskite layer. Inhibiting charge recombination is an effective way to improve the performance of PSCs. The interfaces within PSCs can be engineered through the addition of TDMs to enhance charge transport and improve performance. Consequently, the controlled synthesis of TDMs with well-defined structures and superior properties is essential for their large scale application in photovoltaics. Primary methods for the synthesis of TDMs include exfoliation[53-56] and chemical vapor deposition (CVD)[28, 57-62] which will be discussed in the following sections.

Table 1 Optical and electrical properties of two-dimensional materials.

2D materials	Band gap (eV)	Band type	Carrier mobility ($cm^2V^{-1}s^{-1}$)	Ref.
Graphene	0	Direct	10^3-2×10^5	63, 64
Graphdiyne	1.26	Direct	2×10^5	65
BP	1.60	Direct	10^4-2.6×10^4	66, 67
Monolayer MoS_2	1.715	Direct	10-130	63
Bulk MoS_2	1.710-0.788	Indirect	30-500	63
Monolayer WSe_2	1.7	Direct	140-250	63
Bulk WSe_2	1.2	Indirect	500	63
h-BN	5.9	Direct	NA	63
SnO_2 nanosheet	3.6	Direct	100-200	68
ZnO nanosheet	3.4	Direct	20-40	69

2. Synthesis of Traditional Two-Dimensional Materials and Layered Perovskites

2.1 Preparation of Two-Dimensional Materials

2.1.1 Exfoliation Methods

The preparation of TDMs by exfoliation is cost-efficient and versatile because it can be combined with other chemical treatments to produce a variety of functionalized TDMs.[20, 35, 70-72] The mechanical exfoliation method is widely used to prepare single or few layered TDMs by the application of mechanical forces to solutions of layered materials via stirring, shaking, or ultra-sonication.[53-55] Surfactants are commonly employed to reduce van der Waals interactions which hold layers together as well as keep the exfoliated products suspended in the solvent.[53] Since most TDMs are hydrophobic, it is difficult to dissolve them directly in common solvents (such as water, ethanol, and acetone) without prior surface treatment. This challenge has been recently addressed by Lee et al.[56] They exfoliated bulk-layered materials (graphene, h-boron nitride, MoS_2, etc.) by controlling the temperature of the sonication bath. As shown in **Figure 3**, the exfoliated 2D platelets remain well dispersed in water without using any surfactants for over a month.[56] The stability of the exfoliated nanoplatelets is attributed to the surface charges on the TDMs as a result of edge functionalization (hydroxyl- and carboxyl- functional groups on graphene materials) or their intrinsic polarity.[56] Compared with pristine graphene, carboxyl- and hydroxyl-functionalized graphene has a stronger positive and negative charge, respectively.[56] For h-BN, there are alternating layers of charge distribution resulting in strong polarity across the B and N termination edges. In contrast, MoS_2 exhibits moderate polarity due to the negative charge on the sulfur surface and counter

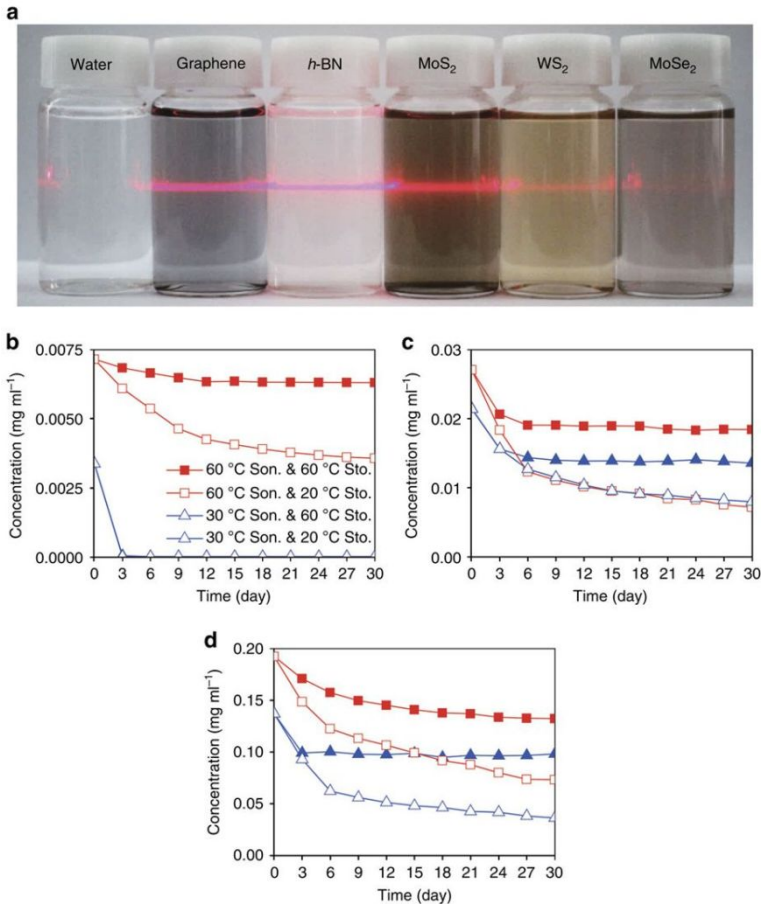

Figure 3. (a) Digital images of five different TDM aqueous solutions one month after dispersion. The long-term solution stabilities of (b) graphene, (c) h-BN and (d) MoS_2 sonicated at 60 °C and 30 °C and stored at 60 °C and 20 °C. Squares and triangles refer to sonication at 60 °C and 30 °C, and solid and blank denote storage at 60 °C and 30 °C, respectively. Reproduced from ref. [56] with permission from Springer Nature, copyright 2015.

charges on the inner molybdenum surface.[56] In addition to mechanical exfoliation, chemical exfoliation methods including ion intercalation[73] and solvent-based exfoliation[74] are employed to produce TDMs of one or a few layers. Chemical exfoliation methods are generally employed to exfoliate graphene oxide (GO) from oxidized graphite[75] by reacting

graphite with strong acids (e.g. nitric acid) and/or oxidants (e.g. $KMnO_4$), known as the modified Hummers method.[76] Unfortunately, these methods are not suitable for synthesizing large area TDMs due to the low yield and inability to control sheet size and layer number.

2.1.2 Chemical Vapor Deposition

Compared to exfoliation method, chemical vapor deposition (CVD) has been recognized as a popular method to grow high-quality TDM films on a large reproducible scale.[28, 57-62] CVD growth of TDMs involves activated chemical reactions of precursors in a specially-controlled environment. It uses transition metals (e.g. Pt, Ni) as catalysts. It is possible to change the process of TDM production by adjusting the catalyst to prepare films with different qualities. **Figure 4** summarizes the general experimental setup of a CVD experiment for preparing two-dimensional graphene. The setup consists of a furnace, a quartz chamber, a control system and mass flow controllers (MFC) for reactant gases.[62] The precursors, conditions, atmosphere, substrates and catalysts are several key factors affecting the final quality of TDMs.

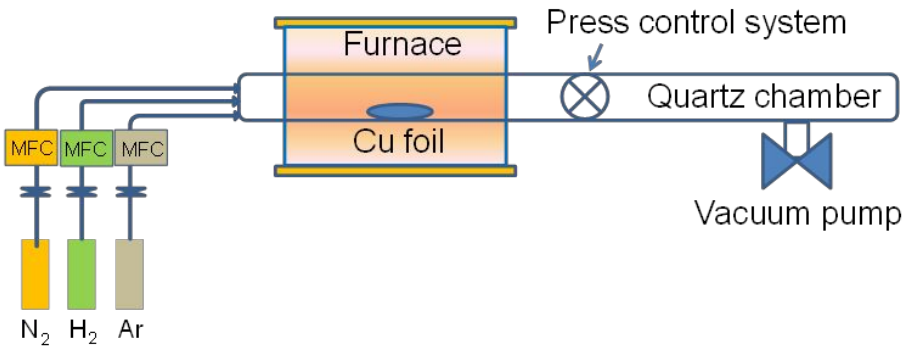

Figure 4. Schematic showing a typical chemical-vapor-deposition setup. Mass flow controllers (MFC) supply reactant gases at the necessary flow rate. Pressure and vacuum control systems are used to adjust TDM growth conditions, and Cu foil is used as a catalyst.

2.2 Layered Two-Dimensional Perovskites

2.2.1 The Structure of Two-Dimensional Perovskite

Two-dimensional perovskites have a layered structure. The most commonly reported layered 2D perovskite possesses an orientation.[77, 78] The general formula of layered perovskite compounds is $L_2(ABX_3)_{n-1}BX_4$ where L represents long chain organic cations (e.g. octylammonium and butylammonium), A represents monovalent metal or organic molecular cations (e.g. Cs^+, $CH_3NH_3^+$ and $C_2H_5NH_3^+$), B represents divalent metal cations (e.g. Pb^{2+}, Cu^{2+}, Sn^{2+}, Ni^{2+}, and Ge^{2+}), X represents halide anions (e.g. Cl^-, Br^-, and I^-), and n represents the number of metal halide octahedral layers between the two layers of the long chain organic cations ($n \geq 1$). As the perovskite layer number is reduced, the bandgap gradually increases from E_g = 1.60 eV ($n = \infty$) to 1.89 eV (n = 4), 2.00 eV (n = 3), 2.14 eV (n = 2) and 2.40 eV (n = 1) for the perovskite $MAPbI_3$, as shown in **Figure 5**.[79-81] Due to the presence of stable excitons with a large binding energy, 2D perovskites exhibit attractive optical properties. For example, it is reported that 2D perovskites can exhibit a four times stronger third harmonic generation in the mid-infrared range over the 3D counterpart because of strong quantum confinement.[81] The substantial carrier mobility in the plane of the perovskite sheet can be realized due to its controlled long-range out-of-plane orientation for nondispersive charge transport. This property makes such systems strongly applicable to optical devices.[82, 83]

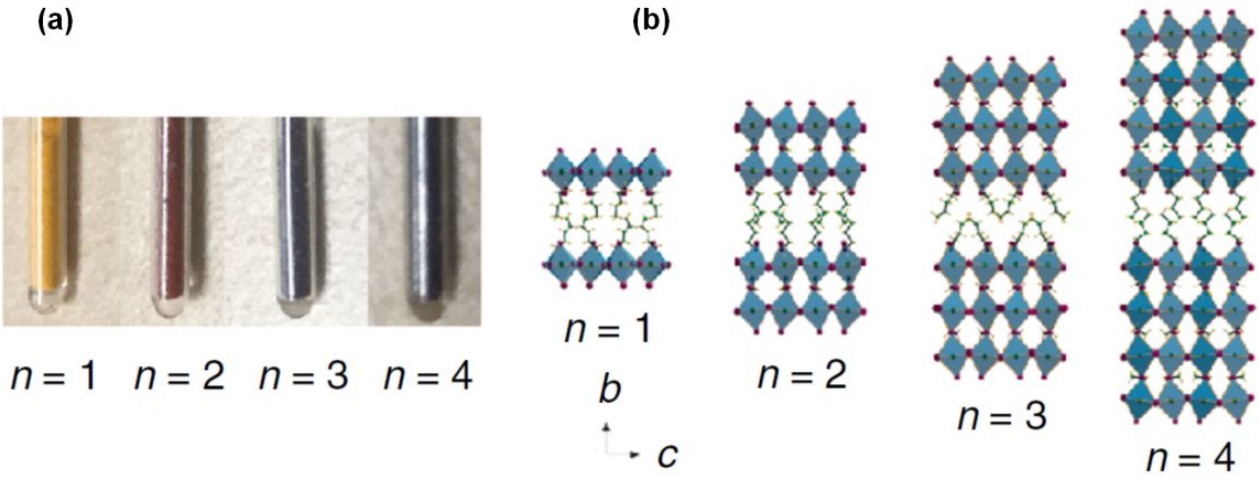

Figure 5. (a) A photograph of perovskite sample powders; the colors indicate a blue shift in the band gap with a reduction in layer number, n. (b) Crystal structures viewed along the (100) crystallographic projection. Pb^{2+} atoms are dark green balls, I^- atoms are purple balls, N atoms are dark blue balls, H atoms are yellow balls, and C atoms are light green balls. Reproduced from ref. [81] with permission from Springer Nature, copyright 2017.

2.2.2 Preparation of Two-Dimensional Perovskites

2.2.2.1 Liquid Phase Methods

An efficient method to produce hybrid 2D perovskites is to exchange the cations present in perovskite nanocrystals with long chain alkyl cations. **Figure 6a** shows the process whereby 2D perovskite layers can be produced from 3D crystal structures by blocking the interaction of layered perovskites using long organic molecular chains in the "A" position.[84] In this method, self-assembly between metal halides and organic chains is driven by coordination, hydrogen bonding and Van der Waals forces upon mixing. The length of the chains is crucial as it drives the reorganization to form 2D structures. Liquid phase methods

using organic alkyl ammonia derivatives as the long alkyl chain source are the most commonly used for synthesizing perovskites with different morphologies,[85-87] including perovskite nanosheets and nanoplatelets, due to their simplicity and low cost. The size and morphology of 2D perovskite can be tuned by controlling the surfactant and mass ratio of organic cations in the perovskite. 2D perovskites prepared by a liquid phase method was firstly reported by Tisdale et al. in early 2015.[85] 2D $CH_3NH_3PbBr_3$ perovskite nanoplatelets (single unit cell is shown in **Figure 6b**) are synthesized with octylammonium bromide $CH_3(CH_2)_7NH_3Br$ as the long-chain ligand. 2D nanoplatelets of $CH_3NH_3PbBr_3$ with different thicknesses were obtained by a slight modification of the synthesis method. 2D all-inorganic perovskite $CsPbBr_3$ nanosheets[88, 89] and $CsPb_2Br_5$[90, 91] can also be synthesized in the liquid phase with ammonium derivatives as the long chain source. The as-synthesized nanosheets can be well dispersed for fabricating solution-based optoelectronic devices. Balakrishnan and Kamat used an ammonium salt with long alkyl chains, dodecyl dimethylammonium bromide (DDAB), to induce the exfoliation of perovskite nanocrystals by forming an intermediate $PbBr^{3-}$ complex followed by reorganization to transform $CsPbBr_3$ nanocrystals into crystalline two-dimensional $CsPb_2Br_5$ nanosheets (**Figure 6c**).[90] Such structural transformations are important for surface treatment to passivate defect sites and design 2D interfaces.

2.2.2.2 Vapor Phase Methods

Vapor phase methods transform the perovskite precursor into the gas phase through sublimation, evaporation or decomposition. Then, the saturated vapor is condensed into a crystal. The methods include both chemical vapor deposition[92] and Van der Waals expitaxy.[93]

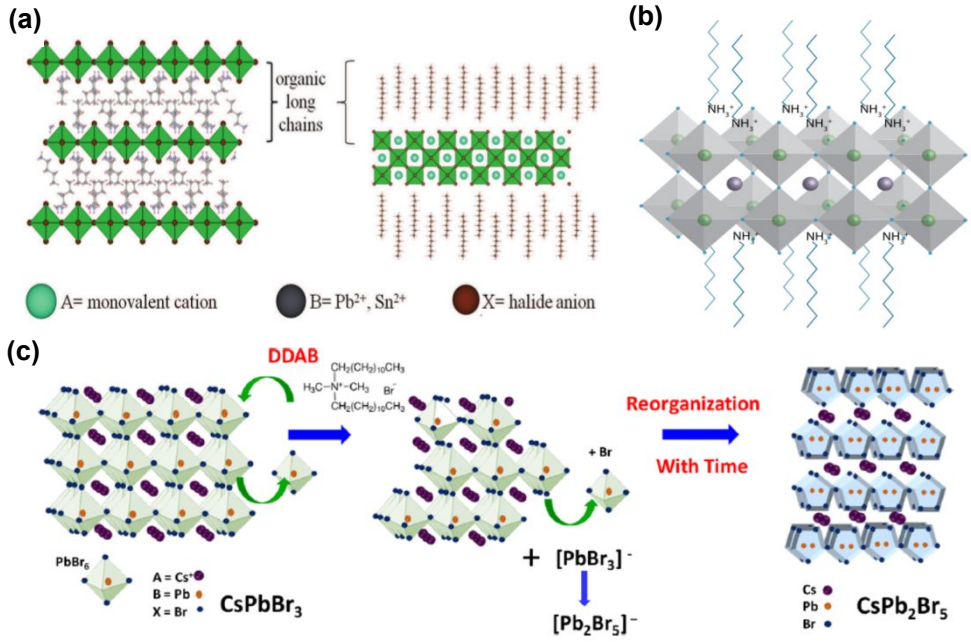

Figure 6. (a) 2D layered perovskite crystal structures (lateral view and top view). Reproduced from ref. [84] with permission from John Wiley and Sons, copyright 2017. (b) 2D perovskite nanoplatelets one unit cell thick. Reproduced from ref. [85] with permission from American Chemical Society, copyright 2015. (c) Schematic representation of ligand-assisted exfoliation and transformation of cubic $CsPbBr_3$ perovskite nanocrystals to tetragonal $CsPb_2Br_5$ nanosheets.[90] The addition of DDAB into the $CsPbBr_3$ solution induces the formation of $[PbBr_3]^-$ via the reaction $n CsPbBr_3 + DDA^+ \rightarrow (n\text{-}x)\ CsPbBr_3 + x DDA^+[PbBr_3]^- + x Cs^+$. Then, the $[PbBr_3]^-$ complex reorganizes to form the stable $[Pb_2Br_5]^-$ species which combines with Cs^+ to form $CsPb_2Br_5$. Reproduced from ref. [90] with permission from American Chemical Society, copyright 2018.

The former technique can offer conformal and controllable thin film growth whereas the latter enables the vapor phase epitaxial growth of perovskites with mismatched lattice constants.

Compared with liquid phase methods, vapor phase methods synthesize more uniform films over larger areas with improved crystallinity and reduced impurities.[94, 95] However, these methods involve more complex physical and chemical processes, are more energy intensive and are more difficult to scale up.[96, 97]

At present, vapor phase methods are generally used to prepare 2D perovskite materials in either one step[93, 94] or two steps.[59, 95-97] The one-step method directly uses a mixture of all the precursors, such as PbX_2 and CH_3NH_3X for synthesizing $CH_3NH_3PbX_3$, as raw starting materials. Then the perovskite nanosheets are produced under the above precursor vapors in a vacuum quartz tube under reduced pressure. The two-step method involves first the deposition of a PbX_2 film under vacuum which is then placed into a quartz reaction tube. Next, the CH_3NH_3X powder is placed in the middle of the quartz tube. When the reaction begins, CH_3NH_3X under Ar or N_2 airflow reacts with the surface of the PbX_2 film. CH_3NH_3X molecules insert into the PbX_2 layer lead to the formation of 2D perovskite. Shi et al. employed a one-step method to grow thin $CH_3NH_3PbCl_3$ perovskite platelets on a muscovite mica substrate by Van der Waals epitaxy.[93] They simultaneously placed all the inorganic and organic precursors, $PbCl_2$, CH_3NH_3Cl powders and the muscovite mica substrate, in an alumina tube followed by heating in argon. To control the reaction process, the positions of the precursors and muscovite mica substrate were carefully placed to ensure uniform deposition.[93] As a result, ultrathin (sub 10 nm) and largescale (a few tens of micrometers in length and width) crystalline 2D perovskite thin films were obtained on layered muscovite mica. Xiong et al. synthesized $CH_3NH_3PbX_3$ perovskite nanoplatelets using a two-step vaporphase process beginning with the growth of lead halide nanoplatelets via Van der Waals

epitaxy followed by a gas-solid heterogeneous reaction with methylammonium halide vapor to convert the as-grown platelets into perovskite.[95] The experimental setup is shown in **Figure 7**. The thicknesses of the PbI_2 and $CH_3NH_3PbI_3$ platelets have a linear relationship as they grow. This is consistent with the c lattice ratio.[95]

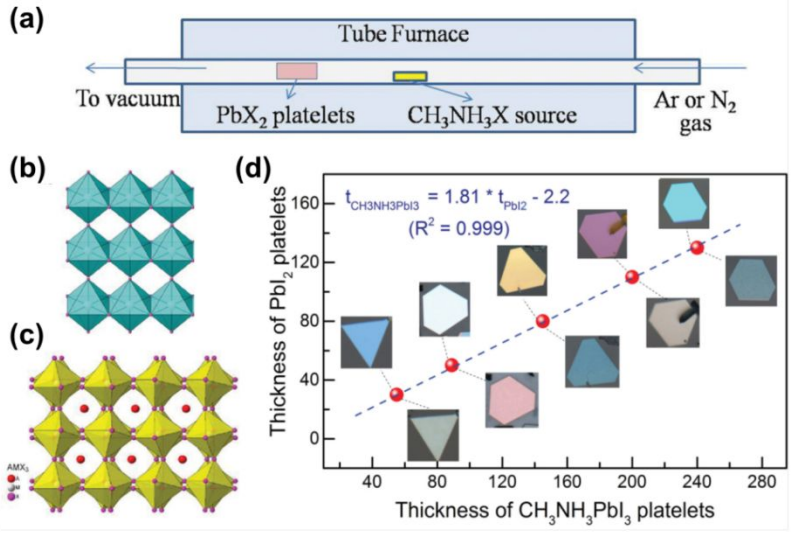

Figure 7. (a) Schematic showing the setup for synthesizing methyl ammonium lead halide perovskite ($CH_3NH_3PbX_3$, X = Cl, Br, I) using a vapor-transport system. (b) Structure of the PbI_2 in which the Pb atoms are at the center of the halide octahedron. (c) Structure of $CH_3NH_3PbX_3$ in which the $CH_3NH_3^+$ groups (red spheres) are located within the center of eight lead halide octahedron. (d) Thickness of PbI_2 platelets before (images above data line) and after (images below data line) being converted to $CH_3NH_3PbI_3$. Reproduced from ref. [95] with permission from John Wiley and Sons, copyright 2014.

Different synthesis methods for TDMs and 2D perovskites greatly impact their performance in PSC devices due to their distinct optical and electronic properties.[59, 98, 99] TDMs have been reported as electrodes and charge transport layers (i.e. HTL, ETL and buffer layer) in PSCs because they can separate and collect photo-generated charge carriers

produced in perovskite absorbers which affects the performance (the open circuit voltages V_{OC}, the short circuit current density J_{SC} and fill factor FF) of PSCs. In addition, 2D layered perovskite absorbers have also been widely studied due to their impact on PSC performance. **Table 2** summarizes the performance of TDMs/2D perovskite-incorporated PSCs reported in recent studies which are addressed in this review. In the next sections, the effect of TDMs or 2D perovskites on the charge-carrier dynamics, efficiency and stability of PSCs is reviewed and discussed.

Table 2. Performance of TDMs/2D perovskite-incorporated PSCs.

No.	Function	2D materials	Synthesis method	Device structure	V_{OC} (V)	J_{SC} (mA/cm^{-2})	FF	PCE (%)	Ref.
1	Electrode	Graphite	Exfoliation	n-i-p Mesoscopic	0.90	23.0	0.68	14.1	[100]
2	Electrode	Graphene	CVD	n-i-p Planar	0.95	17.8	0.72	12.0	[57]
3	Electrode	Graphene	CVD	p-i-n Planar	1.00	21.7	0.78	16.8	[99]
4	Electrode	$AuCl_3$-doped graphene	Photolithography patterning	p-i-n Planar	1.09	21.0	0.78	17.9	[101]
5	Electrode	NdS_2	Exfoliation	n-i-p Mesoscopi	1.05	14.3	0.53	8.3	[102]
6	ETL	Graphene/TiO_2	Exfoliation	n-i-p Mesoscopic	1.04	21.9	0.73	15.6	[103]
7	ETL	Graphene/ZnO	Commercially available	N-i-p planar	0.93	20.0	0.56	10.3	[77]
8	ETL	Graphene /$SrTiO_3$	Exfoliation	n-i-p Mesoscopic	1.00	18.1	0.58	9.4	[104]
9	ETL	Graphene /polymer	Exfoliation	n-i-p Mesoscopic	0.95	19.3	0.64	13.4	[105]
10	ETL	rGO/TiO_2	Exfoliation	n-i-p Mesoscopic	0.93	22.0	0.71	14.5	[106]
11	ETL	rGO/TiO_2	Exfoliation	n-i-p Mesoscopic	0.84	16.5	0.67	9.3	[107]
12	ETL	rGO/TiO_2-Li	Exfoliation	n-i-p Mesoscopic	1.11	22.0	0.80	19.5	[108]

13	ETL	Graphene-TiO_2/GO-Li	Exfoliation	n-i-p Mesoscopic	1.03	22.6	0.69	16.2	[109]
14	ETL	rGO/Zn_2SnO_4	Exfoliation	n-i-p Mesoscopic	1.05	22.5	0.76	17.9	[110]
15	ETL	naphthalene diimide-graphene/SnO_2	Exfoliation	n-i-p Planar	1.08	22.7	0.82	20.2	[111]
16	ETL	GD /PCBM	Exfoliation	p-i-n Planar	0.97	23.4	0.65	14.8	[23]
17	ETL	GD /Fullerene	Exfoliation	n-i-p Planar	1.11	23.3	0.78	20.2	[112]
18	ETL	PCBM(GD) /ZnO(GD)	Exfoliation	n-i-p Planar	1.05	24.1	0.79	20.0	[113]
19	ETL	TiS_2	Exfoliation	n-i-p Planar	1.00	24.7	0.75	18.8	[114]
20	ETL	SnO_2 nanosheet	Hydrothermal method	n-i-p Mesoscopic	1.08	22.6	0.71	17.3	[115]
21	HTL	GO	Exfoliation	p-i-n Planar	0.94	13.7	0.52	6.6	[18]
22	HTL	PEDOT/GO	Exfoliation	p-i-n Planar	1.02	21.6	0.82	18.1	[116]
23	HTL	GO/PEDOT:PSS	Commercially available	p-i-n Planar	0.84	15.8	0.74	9.7	[117]
24	HTL	GO/PEDOT:PSS	Exfoliation	p-i-n Planar	0.96	18.0	0.76	13.1	[118]
25	HTL	rGO	Exfoliation	p-i-n Planar	0.95	14.8	0.71	10.0	[119]
26	HTL	rGO/ PEDOT:PSS	Exfoliation	p-i-n Planar	0.95	17.1	0.64	10.6	[120]
27	HTL	GD/P3HT	Exfoliation	n-i-p Mesoscopic	0.94	19.6	0.71	13.2	[121]
28	HTL	GD/P3CT-K	Exfoliation	p-i-n Planar	1.06	22.8	0.81	19.5	[122]
29	HTL	BP	Exfoliation	n-i-p Mesoscopic	1.06	20.2	0.76	16.4	[25]
30	HTL	MoS_2	Exfoliation	p-i-n Planar	1.01	20.7	0.78	16.4	[123]
31	HTL	WS_2	CVD	p-i-n Planar	0.82	15.9	0.64	8.1	[124]
32	HTL	1T-rich MoS_2	Exfoliation	p-i-n Planar	0.87	20.3	0.77	13.6	[125]
33	HTL	1T-rich WS_2	Exfoliation	p-i-n Planar	0.93	20.6	0.72	13.8	[125]

34	Buffer layer between Perov./ETL	GO-Li	Exfoliation	n-i-p Mesoscopic	1.02	20.0	0.70	14.3	[20]
35	Buffer layer between ETL/electrode	GO-Li /TiO_x sol	Exfoliation	p-i-n Planar	0.91	15.6	0.72	10.2	[72]
36	Buffer layer between Perov./HTL	MoS_2	Exfoliation	n-i-p Mesoscopic	0.93	21.5	0.67	13.3	[126]
37	Buffer layer between Perov./HTL	rGO/4FPH	Exfoliation	n-i-p Planar	1.11	21.5	0.79	18.7	[22]
38	Buffer layer between HTL/electrode	rGO	Exfoliation	n-i-p Mesoscopic	1.11	23.2	0.78	20.4	[127]
39	Absorber	GO/$MAPbI_3$	Exfoliation	n-i-p Planar	1.07	23.7	0.69	17.6	[128]
40	Absorber	$(BA)_2(MA)_2Pb_3I_{10}$	Liquid Phase Method	p-i-n Planar	1.01	16.7	0.74	12.5	[129]
41	Absorber	$(PEA)_2(MA)_2[Pb_3I_{10}]$	Liquid Phase Method	n-i-p Planar	1.18	6.7	0.60	4.7	[130]
42	Absorber	$MAI(PbI_2)_{1-x}(FeCl_2)_x$	Liquid Phase Method	n-i-p Planar	1.10	22.2	0.71	17.3	[131]
43	Absorber	$(PEA)_2FA_8Sn_9I_{28}$	Liquid Phase Method	p-i-n Planar	0.58	14.2	0.62	5.1	[132]
44	Absorber	$(HOOC(CH_2)_4NH_3)_2PbI_4/MAPbI_3$	Commercially available	n-i-p Mesoscopic	1.03	18.8	0.75	14.6	[133]

Perov.: perovskite active layer; GO: Graphene oxide; rGO: Reduced graphene oxide; GD: Graphdiyne; BP: Black phosphorus; P3HT: poly(3-hexylthiophene); 4-FPH: 4-fluorophenyl; MA: methylammonium; FA: formamidinium; BA: n-butylammonium; PEA: phenylethylammonium.

Devices labelled No. 1-5 are discussed in Section 3.1; No. 6-20 are discussed in Section 3.2; No. 21-33 are discussed in Section 3.3; No.34-38 are discussed in Section 3.4; No.39-44 are discussed in Section 4.

3. Two-Dimensional Material-based Perovskite Solar Cells

3.1 Conductivity, Transmittance and Stability of Graphene Electrode Charge Carrier Collectors

Transparent electrodes are critical to high-performance PSCs. An ideal transparent

electrode should be highly conductive, inexpensive, stable, and an effective charge collector. Transparent electrodes in PSCs have been prepared mainly with indium tin oxide (ITO) or poly(3,4-ethylenedioxythiophene):poly(styrenesulfonate) (PEDOT:PSS). However, conventional transparent ITO electrodes are fragile (essentially metal doped glass) and the PEDOT: PSS-based transparent electrodes are hydroscopic (absorb moisture from the atmosphere) leading to the destruction of the perovskite layers which are water soluble.[134] Consequently, more suitable flexible transparent electrode materials are urgently needed for PSCs. Graphene is one promising material for PSC electrodes due to its composition of earth abundant carbon, excellent electrical and optical properties, and mechanical toughness.[98] Large-area graphene grown by CVD was implemented as a transparent electrode in PSCs.[28] Graphene-based PSCs showed high optical transmission below the perovskite energy bands leading to superior charge collection efficiency.[98] Graphene bottom electrodes in flexible inverted PSCs can enhance the photovoltaic performance of the PSC owing to their improved morphology and higher transparency as compared to other carbon allotropes such as carbon nanotubes.[98] However, the transfer step for depositing graphene electrodes into PSC devices has lower reproducibility, which can significantly affect the conductivity of graphene electrodes. Thus, a more consistent graphene transfer method is required to improve its reproducibility and justify the use of highly conductive graphene electrodes in PSC devices. Yan et al. first reported the fabrication of semi-transparent PSCs by laminating stacked multi-layer graphene prepared by CVD as the top transparent electrode.[57] To improve the reproducibility of the graphene electrodes, graphene films was first coated with a layer of poly(methyl methacrylate) (PMMA). Subsequently, a poly(dimethylsiloxane) (PDMS) film

was deposited to the PMMA film to improve the mechanical strength of the graphene electrode. The PDMS/PMMA/graphene film can be easily transferred and laminated onto a solar cell. As the sheet resistance of graphene film (1050 ± 150 Ω sq^{-1}) is high, a thin layer of poly-(3,4-ethylenedioxythiophene): poly(styrenesulfonate) (PEDOT:PSS) was employed as an adhesion layer (sticky coating) on the perovskite layer to improve the conductivity of the graphene electrode. The layer and band structures of devices are shown in **Figures 8a** and **8b**. Multilayer graphene films can decrease transmittance, and affect the light absorption of the active layers in PSCs. The use of two-layered graphene doped with PEDOT:PSS as the electrode offered lower sheet resistance (140 ± 35 Ω sq^{-1}, **Figure 8c**) and higher transmittance

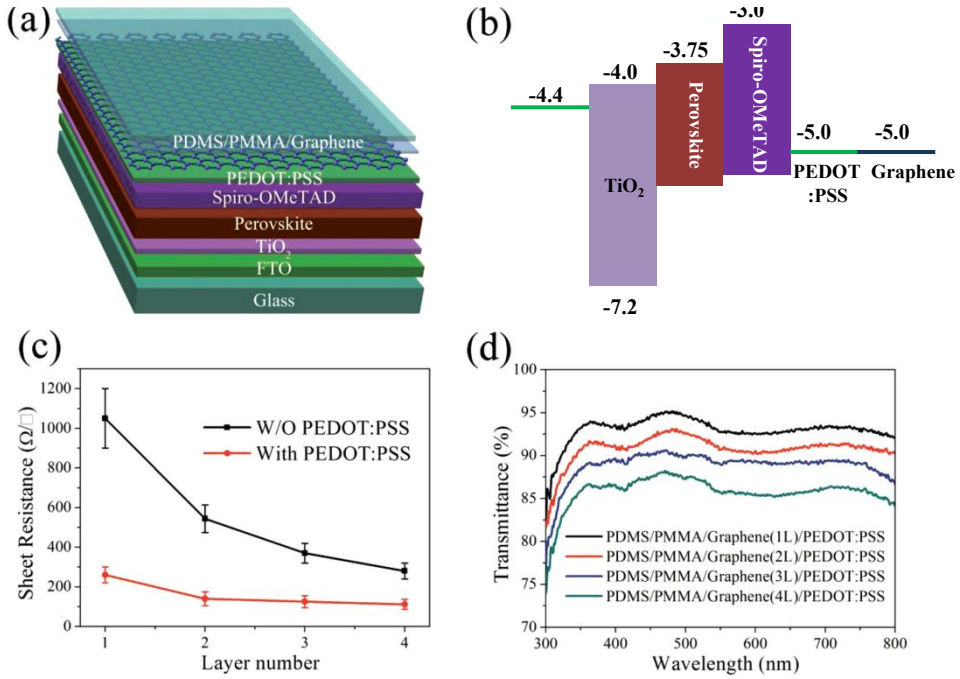

Figure 8. (a) Layer and (b) band structures of a PSC. (c) Sheet resistance of graphene films before and after PEDOT:PSS doping. (d) UV-vis spectra of PEDOT:PSS doped graphene electrodes with graphene. Reproduced from ref. [57] with permission from John Wiley and

Sons, copyright 2015.

(>90% in the visible region, **Figure 8d**) in the visible region.[57] The average PCE of the optimized device with double-layer graphene electrodes reached 12.02% and 11.65% when illuminated from the bottom (FTO side) and top (graphene side), respectively.

Despite high conductivity of graphene electrodes achieved, one major difficulty in the preparation of graphene electrodes is that the transfer polymers such as PMMA cannot be completely removed on graphene surface. The residual transfer polymers can affect the quality of carrier transport layers and perovskite layers coated on the electrode surface. Poly(3-hexylthiophene) (P3HT) is found to be a good candidate as the supporting polymer of graphene electrode.[58] The P3HT-transferred graphene film is cleaner than PMMA. As P3HT is a p-type semiconductor, it can induce a p-type doping in graphene and consequently increase the conductivity of graphene. The graphene film prepared with the P3HT exhibits a lower sheet resistance (~300 Ω sq^{-1}) than that prepared with PMMA (~500 Ω sq^{-1}).[58] With the P3HT-transferred transparent graphene electrode, a PSC with the structure of ITO/graphene/P3HT/$MAPbI_3$/$PC_{71}BM$/Ag can achieve the best PCE of 14.6%. In addition, PSCs using graphene electrodes show good bending durability due to the high flexibility of the electrodes.[58] The resistance of the graphene electrode was unchanged after 500 bending tests (bending radius of 0.175 cm).[58] Jung, Chio et al. fabricated flexible PSCs utilizing graphene as the bottom transparent electrode and analyzed their bending durability (**Figures 9a and 9b**).[99] The terms “Gr-Mo/PEN device’’ and ‘‘ITO/PEN device’’ refer to PSC devices fabricated on polyethylene naphthalate (PEN) substrates containing a MoO_3/graphene electrode or ITO electrode, respectively. The MoO_3 layer was used to optimize the wettability

of graphene surface which enables the formation of uniform PEDOT:PSS layers.[135] Moreover,

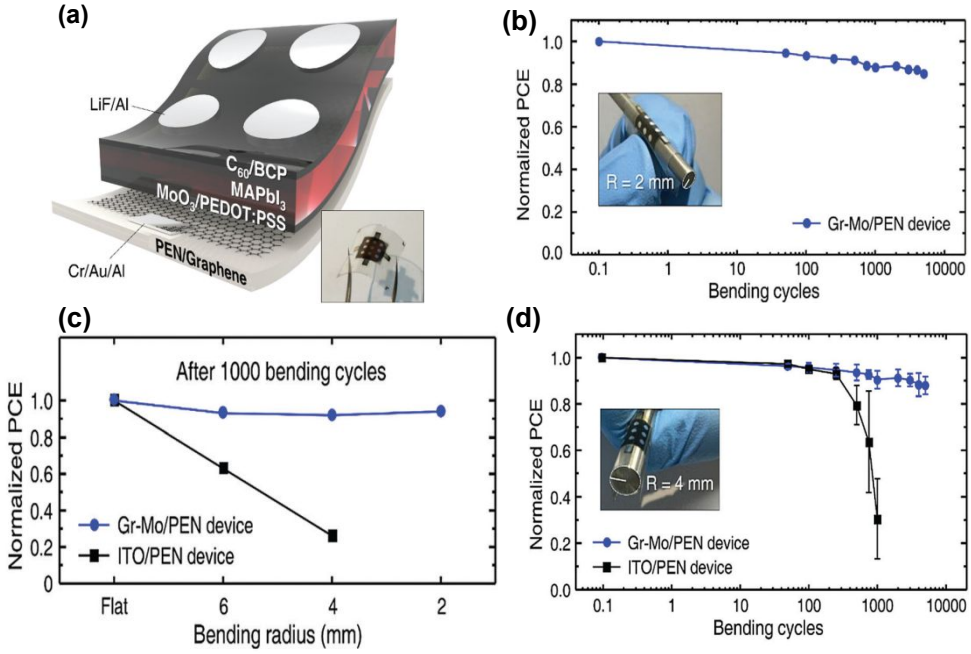

Figure 9. (a) Structure of graphene-based PSCs (inset: A photograph). (b) Bending stability test of graphene-based PSCs. (c) Normalized PCEs measured after 1000 bending cycles. (d) Normalized PCEs at a bending radius (R) of 4 mm (inset: the Gr-Mo/PEN device bent at R=4 mm. Reproduced from ref. [99] with permission from The Royal Society of Chemistry, copyright 2016.

the MoO_3 layer can decrease the sheet resistance of the single layer graphene by over 50% from 1260 Ω sq^{-1} to 552 Ω sq^{-1} due to the p-type doping of MoO_3 on graphene.[99] This behavior is similar to the function of the P3HT polymer previously mentioned.[58] Interestingly, despite the higher sheet resistance of the MoO_3/graphene electrode (552 Ω sq^{-1}) versus the ITO electrode (13.3Ω sq^{-1}), the PSC devices using these two electrodes showed similar J_{SC} values due to the fact that graphene transmitted more light (>97% transmittance) than ITO

(>89% transmittance).[99] The PSC device with the Gr/Mo electrode reached PCE of 16.8% with no hysteresis and exhibited improved stability under bending deformation, maintaining PCEs > 90% of peak efficiency after 1000 bending cycles (**Figures 9c and 9d**).[99] However, the ITO/PEN device decreased to only 40% of its initial value after 1000 bending cycles. This could be attributed to a significantly higher failure strain of graphene (~25%)[136] than that of ITO (~1%).[137] Graphene could withstand more severe mechanical deformation than ITO before generating cracks on the surfaces. The excellent mechanical toughness of the Gr-Mo/PEN device strongly suggests that perovskite photovoltaics with graphene electrodes can pave the way to flexible photovoltaic applications.

Ultimately, the graphene electrode is sufficiently transparent to possess significant light transmittance (> 97%), thus allowing it to overcome the drawbacks of the higher sheet resistance and lower charge collection efficiency with respect to traditional anode materials such as ITO. Graphene is exceedingly ductile, and the failure strain of graphene is about 25 times greater than that of ITO.[136, 137] Consequently, the use of graphene electrodes in flexible PSC devices reduce the change of crack formation under bending conditions, leading to stable electrical performance under significant degrees of deformation. This unique combination of stable performance while bending makes such devices particularly apt for portable and wearable electronics.

Although graphene is a promising electrode material in PSCs, the sheet resistance of current prepared graphene thin films remains high. Also, the high tensile strength of graphene leads to fracturing at low strain. This makes it challenging to take advantage of its extraordinary electronic properties in PSCs.[138] It is important to reduce the sheet resistance

while maintaining the high light transmissivity of the graphene thin film to ensure good performance of graphene-based PSC devices. Doping of graphene with materials such as P3HT[58] and MoO_3[99] has proven to be an efficient method to reduce the sheet resistance of the graphene electrode in PSCs. This is because the doping optimizes the work function of graphene to minimize the energy barrier between the electrode and charge transport layers to enable efficient charge collection. For example, the work function was elevated from 4.23 eV to 4.71 eV and from 4.29 eV to 4.72 eV by hole-doping of MoO_3 into graphene and ITO anodes, respectively.[135] A MoO_3 interfacial layer with a thickness of 2 nm achieved a desirable energy level alignment between the graphene anode and the HTL.[135] As a result, a peak PCE of 17.1% was realized.[135] $AuCl_3$ can also be used to improve the resistance of the graphene electrode by p-type doping. As the work function of Au (5.1 eV) is larger than that of pristine graphene (4.5 eV), the electrons are transferred from graphene to the Au^+ during the doping process, resulting in the downward shift of the Fermi level below the Dirac point.[139] Owing to the p-type $AuCl_3$ doping, the work function monotonically increased from 4.52 to 4.86 eV with increasing concentration of $AuCl_3$.[101] The $AuCl_3$-doped graphene anode showed an improved sheet resistance (~70 Ω/cm^2) compared to pristine transparent graphene conducting electrodes (~890 Ω/cm^2).[101] P-type doping aims primarily to reduce the sheet resistance of the graphene anode. While the extensive work on graphene anodes has proven fruitful with respect to device performance and stability, the graphene cathode in PSCs is rarely reported due to the large work function of graphene. N-Type doping is an efficient method to decrease the work function and sheet resistance of the graphene cathode. Relevant studies have been reported in other photovoltaic applications apart from PSCs. The formation

of n-type graphene can be rendered by doping with ethylene diamine, diethylene triamine, and triethylene tetramine containing two, three, and four amine groups, respectively.[140] As the number of amine groups is increased, the sheet resistance of the doped graphene was reduced from ~700 Ω sq^{-1} to ~205Ω sq^{-1} with a corresponding decrease in transmittance of only 1%. The work function was gradually reduced from ~4.60 eV to ~4.46 eV.[140] N-Type graphene doped with (4-(1,3-dimethyl-2,3-dihydro-1H-benzoimidazol-2-yl)phenyl) dimethylamine was employed as a cathode in inverted polymer light-emitting diodes.[141] Such n-doping reduced a work function of graphene by ~0.45 eV without significant reduction of optical transmittance.[141] The sheet resistance of graphene was reduced by ~35% after n-type doping.[141] On the basis of these studies, to achieve highly conductive graphene anodes and cathodes for high performance PSCs, greater effort must be dedicated to the development of additional favorable hole and electron dopants.

3.2 Effect of Two Dimensional Material-Based Electron Transporting Layers on Carrier Dynamics and Performance of Perovskite Solar Cells

The ETL is one of the most important components in high-performance PSCs. It extracts photo-generated electrons from the perovskite active layer and transports these charges to the electrodes. Simultaneously, the ETL serves as a hole blocking layer to suppress charge recombination.[142] Ideally, ETLs should efficiently transport electrons to minimize the series resistance of PSC devices. Optimizing the characteristics of the ETL, especially the charge mobility, morphology, energy level alignment, and related interfacial properties, is essential for high-performance PSCs.[142] It has been reported that the work functions of TDMs are

tunable, and the electrical conductivity is easily adjusted through functionalization and specific treatment methods.[143-145] Owing to their useful processing-property relationship, TDMs are highly promising alternatives to traditional ETL materials in PSCs.

3.2.1 Electron Extraction and Transport Efficiency of Graphene Derivatives and Their Effect on Device Performance

Since monolayer graphene was first successfully fabricated by Novoselov et al. in 2004, the electrical and optical properties of graphene have been significantly enhanced.[146] Being an ambipolar material capable of efficient transport of both holes and electrons, reduced graphene oxide (rGO) and other solution processable graphene derivatives with tunable energy levels (by functionalization) exhibit remarkably high carrier mobility, a wide spectral absorption range, and high optical transparency.[145, 147] Recently, graphene-based ETLs have found success in scalable fabrication processes by achieving optimized charge carrier dynamics compared to the conventional ETL materials.[109, 148] Incorporation of graphene into the ETLs reduces the series resistance in solar cells, leading to an increase in overall device efficiency.[149]

3.2.1.1 Electron Extraction and Transport efficiency of Graphene Derivative/Inorganic Material Composites and Their Effect on Device Performance

TiO_2 is widely used as an ETL in PSC devices. It has an electron mobility of approximately 1 $cm^2\ V^{-1}\ s^{-1}$ with a conduction band minimum of 4.2 eV vs. vacuum level.[150] However, pristine TiO_2 still has a relatively low electrical conductivity limiting its application

as an ETL. To address this problem, graphene derivatives doped with metal oxides have been employed as ETLs for improving the electron extraction and transport efficiency. As graphene has a work function between that of the typical FTO cathode and the conduction band of TiO_2 ETL, it may reduce the formation of energy barriers at the interfaces, thereby functioning as a mediator of electron transfer.[151] The mobility of a TiO_2 compact ETL after incorporating graphene can be improved from 0.7×10^{-3} $m^2v^{-1}s^{-1}$ to 6.3×10^{-3} $m^2v^{-1}s^{-1}$, more than 8 times that of the pure TiO_2 ETL.[152] The enhanced mobility improves electron transport and collection efficiency, leading to improved device performance (15.4% with graphene and 11.2% without graphene).[152] The high mobility of the ETL reduces its resistivity as well as the series resistance of PSC devices. In the case of rGO/TiO_2 nanocomposite films, the resistivity was reduced from 3.03×10^5 Ω·cm to 4.94×10^4 Ω·cm after adding rGO into TiO_2. A decrease in the series resistance from 10.1 Ω cm^{-2} to 4 Ω cm^{-2} was also observed when incorporating graphene flakes with a TiO_2 ETL in PSCs.[103] This suggests an increase in the conductivity and a reduction in the contact resistance. To further improve the electron dynamics of graphene (G)/TiO_2 ETL in PSCs, a lithium-neutralized graphene oxide (GO-Li) interlayer between the ETL and perovskite layers was added (**Figure 10**). The carrier extraction efficiency of the ETL composites increased by a factor of one and two, respectively, relative to devices using graphene/TiO_2 and standard TiO_2 ETLs.[109] In addition, the ETL composed of G + mTiO_2 + GO-Li significantly improved the crystallinity of the $MAPbI_3$ active layer with a trap density about one order of magnitude lower.[109] Consequently, Jsc was enhanced significantly from 19.7 to 22.8 mA/cm^2.

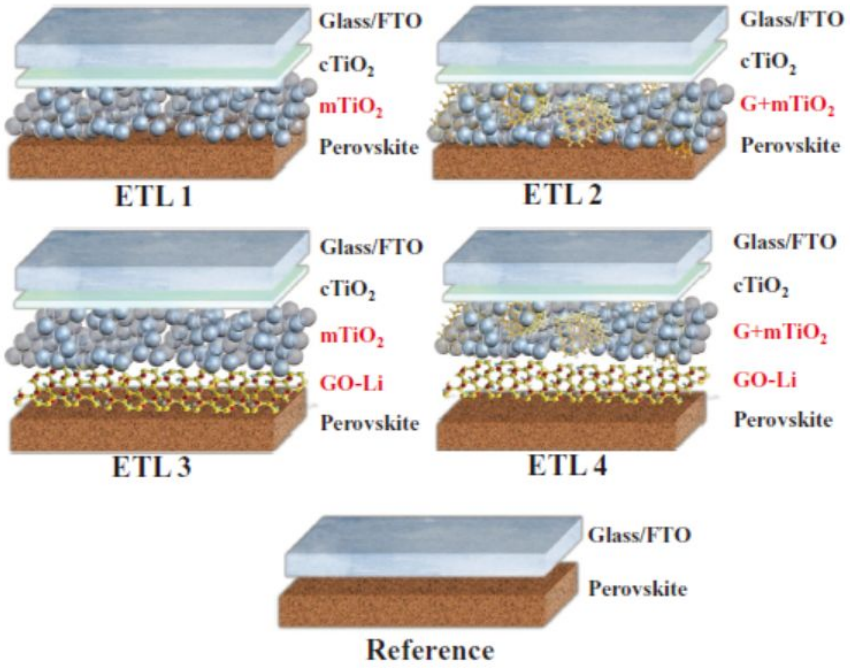

Figure 10 Layer structures of the investigated samples. The ETLs are indicated in red. ETL 1: $mTiO_2$, ETL 2: G + $mTiO_2$, ETL 3: $mTiO_2$ + GO-Li, ETL 4: G + $mTiO_2$ + GO-Li, Reference Sample: no ETL. Reproduced from ref. [109] with permission from John Wiley and Sons, copyright 2017.

Although incorporation of graphene into ETLs does improve the carrier dynamics of devices with TiO_2 ETL, TiO_2-based PSCs degrade rapidly when exposed to UV light. Such devices also typically require a high-temperature sintering process to achieve TiO_2 crystallization, thus restricting the fabrication of PSCs on flexible substrates.[153] ZnO has a band structure similar to TiO_2 (approximately -3.6 to -4.4 eV below vacuum level for the conduction band and -7 to -7.5 eV for the valence band).[154] However, the electron mobility of ZnO is 200 $cm^2\ V^{-1}\ s^{-1}$; two orders of magnitude higher than that of TiO_2.[150] In addition, a sintering process is not necessary to achieve highly crystalline ZnO. The use of graphene

ETLs in ZnO-based PSC devices may be viable for enhancing electron extraction and transport. It has been reported that the addition of GO into ZnO ETLs lowered the series resistance of PSCs by 75% due to the higher electron mobility and lower resistivity for the ZnO-GO nanocomposite (6.7×10^{-3} Ω·m vs 1.9×10^{2} Ω·m for pristine ZnO ETL).[149] With a ZnO-GO nanoparticle ETL, electron transport was increased due to improved conductivity. The interfacial resistance between the graphene/ZnO ETL and perovskite film was reduced, thereby enhancing charge extraction efficiency.[77] In contrast, pristine ZnO ETL-based PSCs typically exhibited low efficiencies due to low temperature annealing during the formation of perovskite crystals. High temperature (>70 ^{o}C) can lead to a chemical reaction between the perovskite absorber and ZnO.[155] Thus, the grain size of the perovskite in pristine ZnO ETL-based PSCs is usually small. The insertion of graphene between the ZnO ETL and perovskite absorber can prevent such interactions. The annealing temperature can increase up to 150 ^{o}C, resulting in larger perovskite grains.[155] Moreover, the addition of graphene can decrease the root mean square roughness of the perovskite film due to the easier infiltration of perovskite precursors into the surface of the graphene/ZnO ETL.[77] As a result, the interfacial modification of ZnO with graphene leads to a significant increase in the J_{SC} and PCE because of the enhanced charge extraction and transport efficiency as well as the improved perovskite film.[77] In addition to the improvement of efficiency, graphene can also improve the stability of PSCs due to its hydrophobic nature. A graphene-SnO_2 ETL-based PSC retained ~90% performance after aging in ambient conditions with a relative humidity of 40 ± 5% for 300 h.[156]

In contrast to widely studied binary oxides, ternary oxides used in ETLs are rarely

reported. $SrTiO_3$ (E_g is 3.25 eV with a conduction band of -3.65 eV below vacuum level and valence band of -6.9 eV) has a band gap similar to TiO_2,[157] but its band structure is more compatible with $MAPbI_3$ whose valence band and conduction band are -3.88 eV and -5.43 eV, respectively.[158] The electron mobility of $SrTiO_3$ at room temperature is 5-8 $cm^2 \cdot V \cdot s^{-1}$; a value larger than that of TiO_2. Furthermore, its high dielectric constant is helpful for increasing the charge lifetime and suppressing trap-assisted recombination at the interface due to the small electron-hole binding energy.[159] The crystallization of $MAPbI_3$ grown on a $SrTiO_3$ ETL is improved when compared to $MAPbI_3$ grown on a pristine TiO_2 layer due to the similar crystal structure shared by $MAPbI_3$ and $SrTiO_3$.[104] The use of pristine $SrTiO_3$ as the ETL in PSCs led to a high V_{OC} but low J_{SC} due to low electron extraction and transport efficiency.[104] Graphene can be introduced into the ETL to improve the electron dynamics due to the high charge mobility and electronic conductivity. Graphene/$SrTiO_3$ nanocomposites as ETL improved the J_{SC} of devices from 12.42 to 18.08 mA cm^{-2} after loading with graphene.[104] With a PCE of 10%, this is the highest reported efficiency for $SrTiO_3$-based PSCs.[104]

3.2.1.2 Electron Extraction and Transport Efficiency of Graphene Derivative/Organic Material Composites and Their Effect on Device Performance

Organic semiconductors are highly desirable as ETLs in PSC devices because of their low temperature fabrication, suitable energy level alignment, and decent electron mobility.[142] Pinhole-free films of organic semiconductors (e.g. fullerene,[160] graphene,[103] and ionic liquids[161]) are typically applied in an inverted p-i-n configuration since its fabrication is difficult to produce in a conventional n-i-p type device.[153] Fullerene and its derivatives, such

as [6,6]-Phenyl-C_{61}-butyric acid methyl ester ($PC_{61}BM$), indene-C_{60} bisadduct (ICBA) and [6,6]-Phenyl-C_{71}-butyric acid methyl ester ($PC_{71}BM$), are the most widely used n-type materials for ETLs in inverted PSCs due to their efficient electron extraction.[142] The conductivity of $PC_{61}BM$ (0.109 ± 0.005 mS cm^{-1}) is significantly increased after the incorporation of rGO as the ETLs in PSCs compared to that without rGO (0.495 ± 0.001 mS cm^{-1}). Thus, the photogenerated charge carriers in perovskite are more efficiently transported to the rGO:$PC_{61}BM$ electron conductor than to the pristine $PC_{61}BM$, leading to higher Jsc and FF values.[160] The rGO additive functions as a bridge for charge injection from the perovskite to the $PC_{61}BM$ ETL. On the other hand, rGO stabilizes the $PC_{61}BM$/perovskite interface with the suppressed degradation rate, making the PSC devices stable under continuous solar illumination.[160] The perovskite film becomes smoother when it is coated by rGO:PCBM ETL compared to that coated by pure PCBM ETL.[160] The traps on the perovskite surface are reduced and passivated, thereby resulting in a higher Voc.[160] The architecture of the fabricated planar inverted rGO:$PC_{61}BM$ ETL-based PSCs is shown in **Figure 11a**. The device exhibited an average hysteresis-free PCE of 14.5%. This value was larger than that of pristine PCBM-based devices at 12.9% (**Figures 11b** and **11c**) due to the enhanced rate of carrier extraction and transport at the rGO:PCBM/perovskite interface (**Figure 11d**) as well as improved perovskite films.[160]

Due to their high electron mobility, graphene derivatives are promising alternatives to incorporate with inorganic and organic electron conductors such as TiO_2 and PCBM, respectively, as composite ETLs in PSCs. They can not only enhance the electron extraction and transport efficiency but also improve the crystal size and film morphology of perovskite.

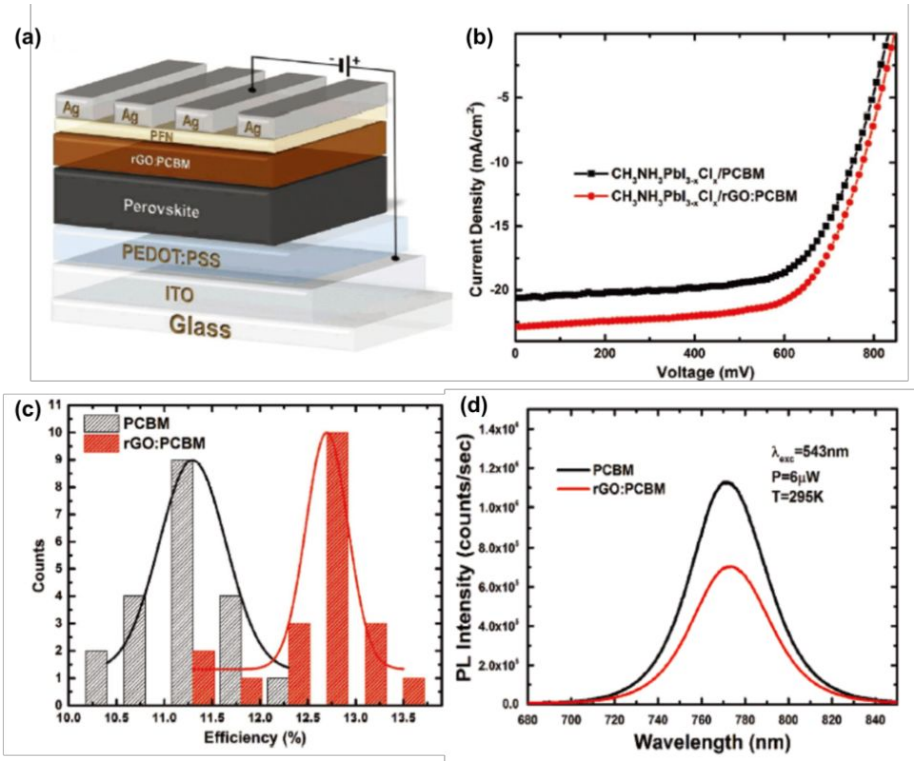

Figure 11. (a) Schematic of the layered structure of a fabricated planar inverted PSC. (b) The J-V curves of PSCs containing a 5% rGO-doped PCBM and pure PCBM ETL. (c) PCE distribution of devices with and without rGO in the PCBM ETL. (d) Photoluminescence (PL) spectra (excitation at 543 nm) of $CH_3NH_3PbI_{3-x}Cl_x$/PCBM and rGO:PCBM/glass substrates. Reproduced from ref. [160] with permission from John Wiley and Sons, copyright 2016.

However, the insertion of these graphene derivatives inevitably decreases the transmittance of devices. The graphene derivatives, such as rGO, can absorb light in the wavelength range of 200-800 nm. The light absorption by the perovskite absorber is reduced with the increase in the density of graphene derivatives, which can reduce the amount of photo-generated carriers and eventually decrease the photocurrent density.[106] In addition, the dimension of the graphene derivatives prepared is usually much larger than the thickness of the perovskite. There is unavoidable direct contact between graphene derivatives and perovskites. Thus,

conductive graphene derivatives create new recombination centers inducing lower photocurrent and fill factor.[103, 104] In order to achieve high performance PSCs, it is critical to find a good balance between the transmittance, carrier extraction and conductivity of graphene derivative-based ETLs.

3.2.2 Electron Extraction and Transport Efficiency of Graphdiyne-Based Composites and Their Effect on Device Performance

The success of graphene-based ETLs in PSC devices has encouraged the development of ETLs based on other TDMs. However, highly conductive graphene has no energy band gap, limiting its application in semiconductor fields.[162] In addition, it is generally difficult to control the functionalization of pure sp^2–carbon materials such as graphene because of its tendency to aggregate.[163] Graphdiyne (GD), a novel kind of 2D carbon allotrope composed of sp- and sp^2-hybridized carbon atoms forming a network of delocalized π electrons, possesses characteristics similar to graphene but with the added benefit of easier functionalization due to improved dispersion.[164] First principle calculations have shown that graphdiyne possesses a natural band-gap in contrast with graphene whose band-gap is zero. Owing to these superior properties, GD is an attractive candidate for use as an ETL in PSCs.

As mentioned above, PCBM is the most widely used ETL material in p-i-n type planar PSCs. However, pristine PCBM-based PSC devices show unsatisfactory photovoltaic performance due to the low coverage area of pristine PCBM ETLs on the perovskite layer, leakage currents, and interfacial charge recombination.[165, 166] In 2015, an ETL composed of PCBM doped with GD was first employed in a planar heterojunction PSC device with an

inverted structure (i.e. ITO/PEDOT:PSS/$CH_3NH_3PbI_{3-x}Cl_x$/PCBM:Graphdiyne/C_{60}/Al).[23] The device architecture of the PSC is shown in **Figure 12a**. Based on the c-AFM measurements, the PCBM:GD film showed significantly increased vertical current, suggesting that the electrical conductivity of PCBM:GD increases upon GD doping.[23] The electron mobility of PCBM:GD based electron-only device increased from 2.98×10^{-4} $cm^2/(V\ s)$ to 5.32×10^{-4} $cm^2/(V\ s)$.[23] A significant quenching effect of PL was resulted in when the perovskite layer was coated with the PCBM:GD ETL.[23, 113] The GD doping enhanced electron transport from perovskite to PCBM and reduced the electron accumulations that usually occur at the interlayer of perovskite devices due to the relatively strong π-π stacking interaction between GD and PCBM.[113] Moreover, the perovskite layer coated by PCBM:GD film becomed smoother than that coated by the pure PCBM film. The grain-boundary of the perovskite was passivated after the addition of GD, thereby reducing the trap states of the perovskite surface and suppressing carrier recombination.[23, 113] The introduction of GD led to improved performance with the PCE increasing from 13.5 to 14.8% and the J_{SC} increasing from 22.3 to 23.4 mA cm^{-2} (**Figure 12b**).[23] A steady-state PCE was obtained, as shown in **Figure 12c**. The enhanced performance can be attributed to the improved electrical conductivity, strong electron mobility, efficient charge extraction and transport, and improved coverage area of the PCBM:GD ETL on the perovskite layer.[23] GD has also been integrated into a solution-processable cross-linked fullerene [6,6]-phenyl-C_{61}-butyric styryl dendron ester (PCBSD) ETL.[112] The structure of the perovskite planar heterojunction solar cells is shown in **Figure 13**. After GD doping, face-on stacked PCBSD molecules were assembled due to the π-π stacking interaction between GD and cross-linkable PCBSD. This orientation is favorable

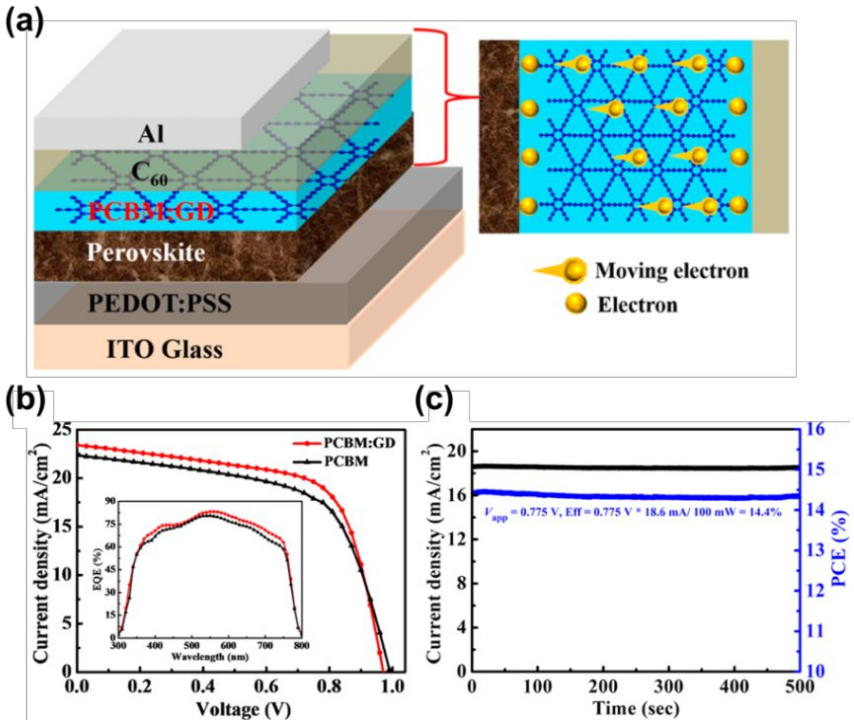

Figure 12. (a) Layer structure of a PSC device with graphdiyne; (b) J-V curves of pure PCBM and PCBM:GD based PSCs (Inset shows the corresponding EQE spectra of the devices); (c) Steady-state efficiency (blue) with the J_{SC} (black) of the PCBM:GD based PSC. Reproduced from ref. [23] with permission from American Chemical Society, copyright 2015.

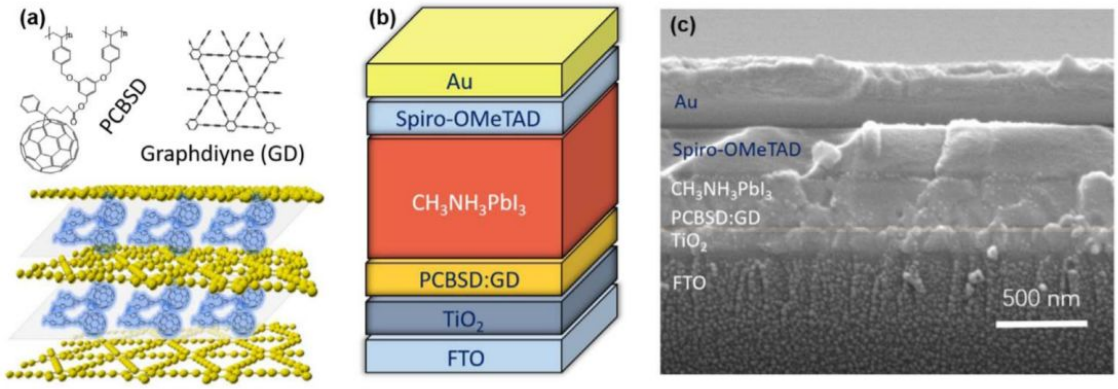

Figure 13. (a) Chemical structure of PCBSD and GD, and schematic illustration of the face-on stacked cross-linkable PCBSD (C-PCBSD) film. (b) Structure of planar heterojunction PSC devices. (c) Cross-section SEM image of a typical PSC with a C-PCBSD: GD based ETL. Reproduced from ref. [112] with permission from Elsevier, copyright 2017.

for the growth and crystallization of subsequent perovskite films. The cross-linkable PCBSD-graphdiyne composite ETL layer demonstrated superior electron mobility, energy-level tailoring, and efficient charge extraction. Consequently, these PSCs attained a maximum PCE of 20.19% with improved cell stability in air (dark).[112] When ZnO replaces the organic electron transporters such as PCBM and PCBSD as ETLs in PSCs, it was found that the doping of GD increases the electrical conductivity and the electron mobility of ZnO and improves perovskite film morphology.[111] Doping GD passivates the traps in organic and inorganic ETLs such as PCBM and ZnO films, respectively, thus suppressing carrier recombination at the interface of PSCs and consequently reducing the J-V hysteresis and improving FF.[23, 113]

Thus, we conclude that GD is a cost-effective and superior alternative to prevalent carbon materials such as graphene and carbon nanotubes for several applications in photovoltaics. Due to its excellent intrinsic electrical properties, it can greatly enhance the electron extraction and transport when combined with traditional ETL materials such as ZnO and PCBM in PSCs, bridging the gaps at interfaces by providing good electrical contact and low interfacial resistance. GD can passivate the grain boundaries of perovskite films and reduce the trap states on the surface to eliminate carrier recombination. Despite these advantages, the study on GD-based ETLs is still in its infancy. The large scale fabrication of high-quality and defect-free ultrathin GD still remains challenging which limits its application in PSCs. Moreover, the studies on chemical functionalization of GD with other elements or functional materials are needed to produce the desired bandgap structure.

3.2.3 Electron Extraction and Transport Efficiency of Two-Dimensional Metal Oxides and Their Effect on Device Performance

Two-dimensional (2D) metal oxide nanosheets can enhance the electrical contact at the perovskite interface to facilitate electron extraction and transport.[44] It can provide direct pathways for electron transport, shortened pathways for carrier diffusion, and high specific surface area offering more transport channels. The interlayer spacing in 2D nanosheets is beneficial for the intercalation of perovskite particles in bi-layer PSC configurations. Therefore, it is viable to use 2D metal oxides as ETLs in PSCs. To date, several 2D metal oxides that have been used in ETLs for PSCs including SnO_2 nanosheets,[43, 44] TiO_2 nanosheets,[45, 46] WO_3 nanosheets,[47] and ZnO nanosheets.[48] Current research on 2D metal oxide-based ETLs remains sparse. TiO_2 nanosheet ETLs containing high levels of exposed (001) facets were reported in a hole-conductor-free mesoscopic TiO_2/ $MAPbI_3$ heterojunction solar cell device, as shown in **Figure 14a**.[45] Owing to the high ionic charge concentration of the (001) facets in TiO_2 nanosheet, the attachment of the perovskite onto the TiO_2 surface is stronger than that to the nanoparticle layer. This stronger anchoring further facilitates electron injection from the perovskite layer into the TiO_2 ETL, resulting in improved device performance.[167] When employing ZnO nanosheets as ETLs in $MAPbI_3$ PSCs (**Figure 14b**),[48] 2D ZnO nanosheets encouraged electron transfer leading to an improvement in PCE comparable to that of PSCs based on ZnO nanoparticles.[48] This improvement is also attributed to the increased interfacial contact between the ZnO nanosheet and perovskite layer. In addition, the PbI_2 could form on the ZnO nanosheet surfaces due to the alkaline behavior, leading to reduced charge recombination and improved electron collection at the interface of

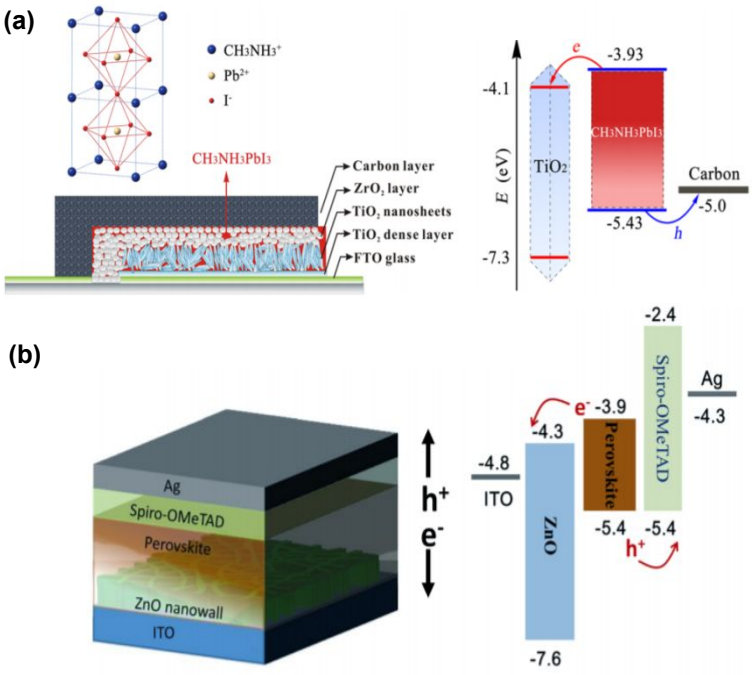

Figure 14. (a) Schematic and energy level diagram of a PSC based on an anatase TiO_2 nanosheet ETL and carbon counter electrodes. Reproduced from ref. [45] with permission from American Chemical Society, copyright 2014. (b) Device structure and energy band diagram of the ZnO nanosheet ETL-based device. Reproduced from ref. [48] with permission from Elsevier, copyright 2016.

ZnO and perovskite.[168] A type I band alignment between PbI_2 and perovskite forms energy barriers to prevent excitons from the surface defects and traps states.[168] Thus, a carrier transport route with less non-radiative channels is presented in the film. The self-induced conversion of PbI_2 effectively passivates the grain locally, resulting in a high quality perovskite film.[168] It has been demonstrated that 2D metal oxide based ETLs are superior to other types of metal oxide nanostructures in PSCs. [47] The PSC devices using WO_3 nanosheet arrays as ETLs showed enhanced photovoltaic performance (PCE=11.24%) compared to

devices using one-dimensional nanorods (PCE=9.10%) and zero-dimensional nanoparticles (PCE=6.08%) as the ETLs. Single crystalline growth of monoclinic WO_3 nanosheets with dominant facet (002) formed perpendicular to the substrate surface. Such highly oriented crystals improve the diffusion of electrons for longer distance diffusion and enhance the charge transport.[47] On the other hand, optimized perovskite absorber infiltration in the porous scaffold of WO_3 nanoseheet is achieved, which may be additional main cause of enhanced photovoltaic performance as compared to nanoparticles and nanorod arrays. In addition to enhancing electron extraction and transport efficiency, 2D metal oxide ETLs can also improve the stability of PSCs. A hierarchical ETL containing a thin compact SnO_2 layer and a mesoporous layer of 2D SnO_2 nanosheets was reported which provides efficient electron diffusion from SnO_2 to perovskite for enhanced electron collection.[43] This hierarchical SnO_2 layer can protect the perovskite layer from moisture in the air, leading to improved device lifetime. It was found that almost no change occurs for the perovskite/ SnO_2 ETL after 1500 h under 20% humidity. Even after pushing to the limit by testing for 10 h under 95% humidity, virtually no change was observed. Consequently, 90% of the initial device efficiency (16.17%) was retained after storage in ambient atmosphere for 130 days without encapsulation.[43]

Therefore, 2D nanosheet arrays of metal oxides as ETLs open up new opportunities in the development of highly efficient perovskite solar cells. They can be vertically aligned with respect to the substrate surface in PSC devices and present an open structure which favors rapid electron extraction and transport as well as excellent perovskite infiltration to form high quality perovskite film. The nanosheet ETLs can improve the stability of PSC devices by

protecting the perovskite layer from moisture. Nevertheless, there is still a lack of sufficient understanding of the intrinsic relationship between the ETL nanostructures and their PSC performance. Controlled synthesis is of great importance in improving the performance and understanding the intrinsic mechanisms. The morphology, optical and electronic properties, band structures and charge transfer processes can be designed via controlled synthesis. Density functional theory calculations can be adopted as an effective method to simulate the electronic structures of these metal oxide nanostructures, rendering purposeful design of PSC devices.

3.3 Effect of Two Dimensional Material-Based Hole Transporting Layers on Carrier Dynamics and Performance of Perovskite Solar Cells

In addition to the ETL, the HTL is another important layer whose development can significantly improve the PCE and stability of PSCs. The ideal HTL should have a proper work function to ensure an ohmic contact with the donor material and the ability to exclusively extract holes effectively from a light absorber (such as $MAPbI_3$) and quickly transport them to the electrodes. Furthermore, the reliability and chemical compatibility of HTLs should also be taken into account to guarantee the long-term stability of PSC devices. Spiro-OMeTAD 2,2',7,7'-Tetrakis-(N,N-di-4-methoxyphenylamino)-9,9'-spirobifluorene) and PEDOT:PSS are widely used as HTLs in n-i-p- and p-i-n-type PSCs, respectively. However, the stability of these materials is uncertain.[169] They are sensitive to oxygen and even more sensitive to moisture than their inorganic counterparts.[170] Attempts to substitute them with other HTL materials have been made. Some of the alternatives that have been realized include

organic phthalocyanines[171] and inorganic copper(I) iodide.[172] Traditional TDMs, such as graphene and its derivatives, have suitable work functions and good film-forming properties, which make them useful as efficient HTLs.[173] With the various strategies developed for improving graphene-based material properties in PSCs, several highly efficient and stable PSCs have been reported using graphene-based HTLs. Details of graphene-based HTLs are reviewed in the following section.

3.3.1 Hole Extraction and Transport Efficiency of Graphene Derivatives and Their Effect on Device Performance

In 2014, Sun et al. first reported the use of graphene oxide (GO) as a HTL in an inverted planar heterojunction PSC with $CH_3NH_3PbI_{3-x}Cl_x$ as the active layer (**Figure 15a**).[174] GO was applied as an HTL due to its suitable work function (~4.9 eV) and acceptable vertical resistivity which is an order of magnitude lower ($\sim 10^3-10^4$ Ω/cm) than the lateral resistivity.[173] Holes can be easily extracted and transported via the sp^2 clusters of GO. The sp^2 clusters are isolated laterally but are in contact with the electrodes. In addition, GO can dope the surface of active layers.[175] The presence of carboxylic acid and phenolic and enolic groups in GO leads to a high proton density of one exchangeable proton per 8.7 carbon rings,[175] resulting in the p-type doping of the active absorber and high conductivity at the interfaces. The increased proton mobility can be attributed to the stabilized negative charge on the surface oxygen because of the delocalization of the 2p electrons of functional oxygen into the π-conjugated system.[176] When a thin GO layer was deposited onto a P3HT HTL, the electrical conductivity of P3HT increased by six orders of magnitude to reach as high as 3.70 S m^{-1}

with a metallic-like characteristic.[175] Charge transfer absorption peaks in near infrared regions

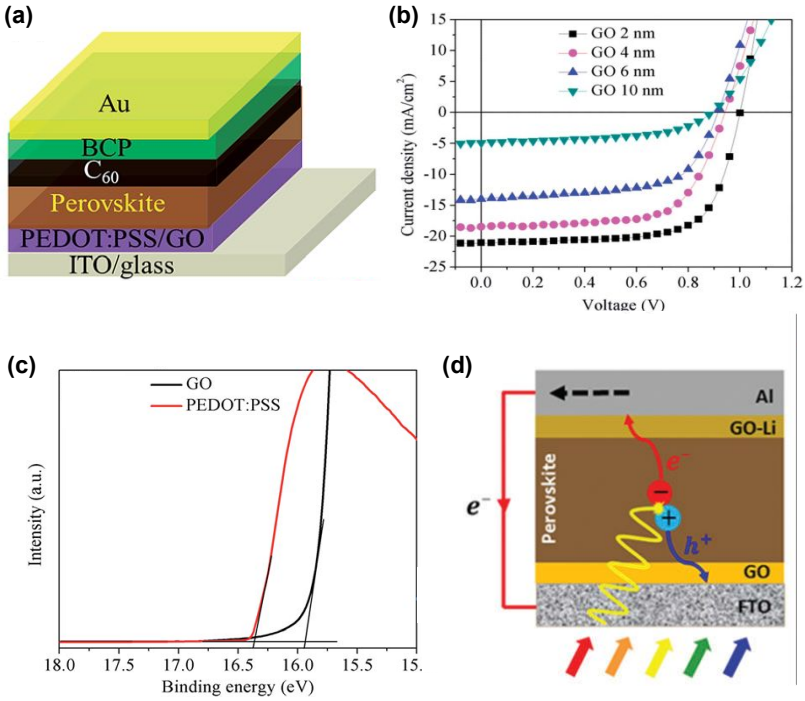

Figure 15. (a) Device architecture of PSC with PEDOT:PSS or GO as the HTL, (b) J-V curve of PSCs with different thicknesses of the GO layer, (c) UPS spectra of PEDOT:PSS and GO on an ITO. Reproduced from ref. [24] with permission from The Royal Society of Chemistry, copyright 2017. (d) Schematic illustration of a inverted planar PSC with GO as the HTL and lithium-modified GO as the ETL. Reproduced from ref. [72] with permission from The Royal Society of Chemistry, copyright 2017.

were observed due to the conductivity increase.[175] Thus, the GO layer can efficiently extract and transport the photo-generated holes from the $CH_3NH_3PbI_{3-x}Cl_x$ perovskite active layer to the electrode resulting in GO HTL-based PSC devices with efficiencies of over 12%.[174] In addition, the perovskite film grown on GO exhibited enhanced crystallization with preferred orientation of the (110) plane, leading to more carriers generated in perovskite layer.[174] Based

on these results, researchers have further optimized the fabrication process. A balance of high work function and conductivity was achieved by controlling the thickness of the GO layer.[24] By optimizing the thickness of GO, GO HTL-based PSCs can achieve a PCE as high as 16.5% with no hysteresis (**Figure 15b)**. The devices exhibited better hole extraction efficiency due to the higher work function of GO (5.2 eV) than that of PEDOT:PSS (4.9 eV) as shown in **Figure 15c**. Under high humidity and continuous light irradiation, the PSC devices retained > 80% of their initial efficiency after 2000 h. This performance was better than the reference device using a PEDOT:PSS HTL.[24] The performance improvement is due to the enhanced charge extraction efficiency stemming from the better alignment of band energies and higher optical absorption due to a higher work function of GO and the larger grain size of perovskite grown on the GO film. Mohammadi, Lianos et al. prepared GO-based PSCs with GO as the HTL, Li-modified GO as the ETL, and Al as the counter electrode in p-i-n type PSCs (**Figure 15d**).[72] A maximum solar conversion efficiency of 10.2% was achieved.

Despite these achievements of GO HTL, the photovoltaic performance of GO HTL-based PSCs remains low due to insulating properties of GO and the high degree of oxygen contents such as -C-O-C, -C-OH, and -C-COOH on the surface. Holes are efficiently extracted from perovskite to GO but also trapped on the localized oxygen atoms of GO, leading to electron-hole recombination at the interfaces. rGO is a carbon material which is formed by eliminating a significant fraction of the oxygenated moieties in GO via reduction. rGO exhibits semi-metal characteristics with a work function of 4.9 eV, hole conductivity of 0.05-4 S cm^{-1}, and hole mobility of 2-200 cm^2 V^{-1} s^{-1}, which is higher than GO (0.25 cm^2 V^{-1}

s^{-1}), yet 2-4 orders of magnitude lower than graphene due to the presence of residual groups and defects.[177]As oxygen-containing groups are reduced, the delocalized holes on the rGO ring can transport freely to the ITO substrate, leading to a larger photocurrent in the rGO device versus the GO device (**Figure 16a**).[178] The contact angle of rGO becomes larger due to the decrease of oxygenated moieties, which induces lower surface energy. It has been verified that the low surface energy of a HTL in PSC can suppress heterogeneous nucleation, facilitating the perovskite crystal grain growth and the formation of a uniform perovskite film.[179] An average grain size of $MAPbI_3$ on GO was 183 nm, while becoming over 200 nm with more centralized grain size distributions when the perovskite was coated on rGO.[180] A preferred (220) grain growth of $MAPbI_3$ was obtained when the perovskite was deposited on rGO which was not observed for deposition on ITO or GO.[180] The (220) crystallographic plane has small surface energy and interfacial energy, which can reduce recombination in the bulk or at interfaces.[181] The hole trap density was calculated to be 7.72×10^{15} cm^{-3} and 5.99×10^{15} cm^{-3} for perovskites on GO and rGO, respectively.[180] The decrease in trap density can enhance V_{OC} by improving the extraction efficiency of holes at the interfaces of HTLs and perovskites. It is important to note that rGO HTL-based PSCs showed improved stability not only under illumination but also during bending tests. Carlo et al. demonstrated mesoscopic PSCs using rGO as a HTL (**Figure 16b).**[182] Although the PCE was 40% lower than that of Spiro-OMeTAD-based devices due to the smaller J_{SC}, the rGO-based PSCs retained a PCE of 6.6% after testing for 1987 h, an improvement over conventional devices using a Spiro-OMeTAD HTL (PCE = 6.5%). After a 120 h light endurance test, the rGO-based PSC retained 26% of its pristine PCE whereas the Spiro-OMeTAD-based PSC

retained roughly 10% of its pristine PCE.[182] The improved stability of rGO-based PSCs in comparison to the Spiro-OMeTAD counterpart is because some additives (i.e. 4-TBP) corrode

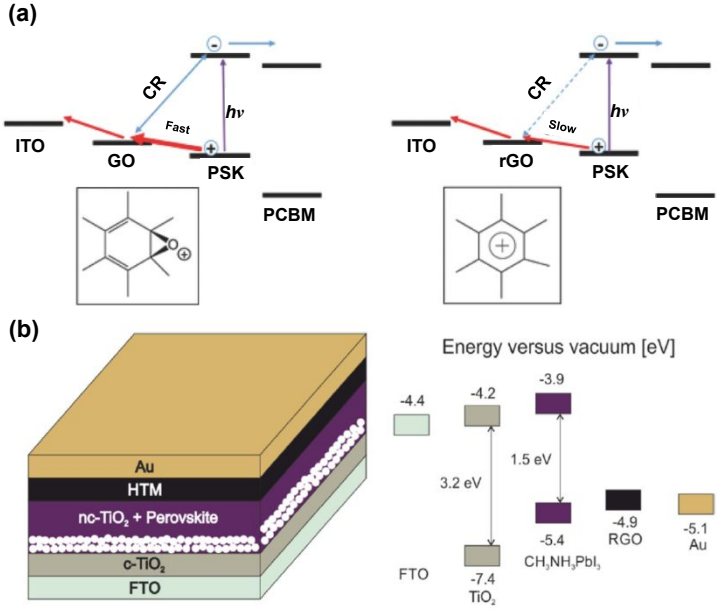

Figure 16. (a) Diagram of the charge recombination (CR) and transfer mechanism for GO and rGO used to rationalize the observed hole extraction kinetics at the HTL/perovskite (PSK) interface. The box in insets represent the localized holes on the oxygen atoms and the delocalized holes in the benzene ring of GO and rGO, respectively. Reproduced from ref. [178] with permission from John Wiley and Sons, copyright 2017. (b) Device architecture and energy band alignment of a PSC device containing a rGO HTL. Reproduced from ref. [182] with permission from Elsevier, copyright 2016.

the perovskite layer. Fortunately, these additives are not necessary in rGO HTLs.[183] A flexible device with rGO HTL on a ITO/polyethylene 2,6-naphthalate substrate showed a PCE 13.8% and retained 70% of the original performance after continuous bending for more than 150 cycles,[178] demonstrating the good bending durability of rGO due to its excellent flexibility.

One major challenge of using graphene derivatives such as GO and rGO nanosheetes as HTLs in PSCs is that they generally do not completely cover the ITO surface when applied by spin coating due to their 2D nanosheet structure and minimal interaction with the ITO surface.[173, 184] It has been demonstrated that the quality of the carbon nanosheet film is strongly related to the amount of hydrophilic groups on its surface. These groups favor the formation of a stable nanosheet suspension during spin coating.[178] Compared to -BH groups, $-SO_3H$ and -NH- groups on the surface can produce a more stable nanosheet suspension with less aggregation, which facilitate the formation of a more uniform HTL film in PSCs.[178] Another problem is that the increased reduction time may decrease the work function of carbon nanosheets such as rGO due to the shift of the surface ionization potential,[180] increasing the mismatch of the energy band level between the perovskite and HTL. This leads to an acceleration in radiative carrier recombination. In addition, the properties of the solvents for nanosheets are important in preventing corrosion of the perovskite layer as the spin coating of the nanosheets is carried out directly on the perovskite layer. The solvents with low boiling point, such as isopropyl alcohol and chlorobenzene, are required to permit its evaporation before reaching the substrates.[182] Thus, the high performance of graphene derivative HTL-based PSCs is highly dependent on the preparation procedure, which directly dictates the morphological, electrical and optical properties of the carbon nanosheets. Even though GO and rGO are promising hole extraction and transport materials, the reported results are still unclear as to which is more suitable as an HTL for PSC devices. The high proton density of GO facilitates the proton doping of perovskite. The unique 2D structure of GO prevents it from penetrating into the bulk of the active absorber, making it an ideal material

for surface doping to increase conductivity.[174] The existence of ample oxygen-containing functional groups attached to the tetrahedral-coordinated carbon atoms (-Cs_{p3}-O-C_{sp3}, -C_{sp3}-OH, -C_{sp3}-COOH, etc.) may induce efficient hole extraction and transport.[178] However, the localized holes on oxygen atoms may increase the possibility for charge recombination at the HTL/perovskite interface.[183]In addition, the epoxy and hydroxyl groups, which disrupt the sp^2 conjugation of the graphene lattice, result in the insulating property of pristine GO which is detrimental for hole collection.[185, 186] In contrast, when these oxygen-containing groups are reduced in rGO, the hole injection from perovskite to HTL occurs most likely at the C=C double bonds of the carbon rings in rGO, which can reduce hole injection at the interface. Further, the delocalized holes in the benzene rings of rGO retard charge recombination and improve performance.[178] Thus, there exists both advantages and disadvantages for each with respect to hole extraction and transport. Systematic investigations of these graphene derivatives are required to better understand their optoelectronic properties and to optimize their photovoltaic performance.

3.3.2 Hole Extraction and Transport Efficiency of Graphene Derivative-Based Composites and Their Effect on Device Performance

Since pristine GO as an HTL in PSCs has some drawbacks such as its insulating properties and charge recombination induced by oxygen-containing groups, a composite of GO and PEDOT:PSS as HTLs is expected to compensate for the drawbacks of pure GO.[116-118, 120, 187-190] A well-matched work-function between graphene oxide (4.9 eV) and PEDOT:PSS (5.1 eV) resulted in more efficient charge extraction and transport to the ITO

electrode (4.7 eV) as well as an overall decrease in the series resistance (R_S) as shown in **Figures 17a** and **17b**.[117] GO suppresses carrier recombination, leading to an increase in shunt

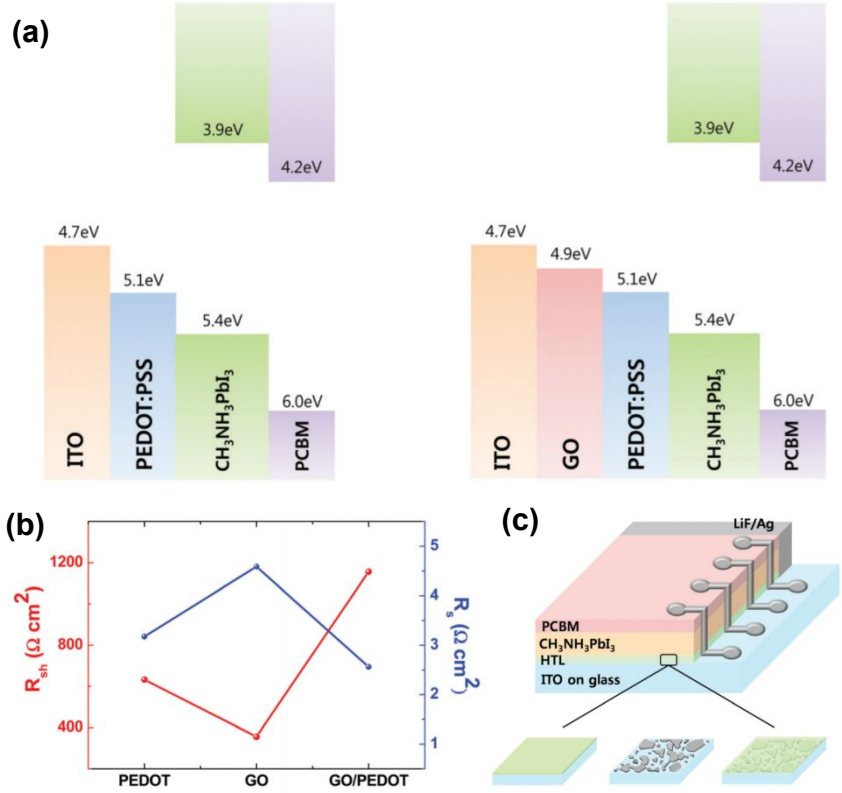

Figure 17. (a) Schematic of energy levels for PSC architectures with PEDOT:PSS (left) and GO/PEDOT:PSS (right) HTLs, (b) R_{Sh} and R_S evaluated from J-V curves, and (c) the structure of the layered PSC device. Reproduced from ref. [117] with permission from The Royal Society of Chemistry, copyright 2015.

resistance (R_{Sh}).[117] When a conventional PEDOT:PSS HTL was doped with GO, the hole mobility increased from 5.55×10^{-5} to 1.57×10^{-4} cm^2 V^{-1} s^{-1}.[191] The GO/PEDOT:PSS HTL fabricated by sequential spin-coating of GO and PEDOT:PSS in a planar heterojunction PSC (**Figure 17c**)[117] can reduce the impact of single component GO HTLs and conventional

PEDOT:PSS. For example, the insulating properties of a pure GO HTL induced a low PCE of 6.4%, whereas a conventional PEDOT:PSS based PSC showed an improved PCE of 8.23%. In contrast, PSCs with a GO/PEDOT:PSS composite HTL exhibited a higher PCE of 9.7%.[117] Devices with GO exhibited relatively wide variations due to the low uniformity of GO caused by its 2D nanosheet nature and minimal interaction with the ITO surface, as noted in Section 3.2.1.[173, 184] Large morphological deviations of the perovskite active layers occurred in p-i-n PSC devices. In contrast, GO/PEDOT:PSS based devices showed highly reproducible performance due to the optimized compatibility of the composite HTL with the ITO substrate. The long-term stability of such PSCs under atmospheric conditions was also improved when compared to a conventional PEDOT:PSS or pristine GO system. The PCE of PSCs fabricated with the GO-modified PEDOT:PSS as a HTL retained 83.5% of their initial efficiency after aging for 39 days under 15% relative humidity.[187] GO prevented direct contact between ITO and the highly acidic PEDOT:PSS layer leading to improved stability. In addition, the $MAPbI_3$ films grown on GO/PEDOT:PSS were highly homogeneous pin-hole free with large crystalline domains and a preferential in-plane orientation of the (110) plane, whereas the films on pristine GO HTLs exhibited pin-holes which may act as defects to induce severe degradation and reduction in the performance.[117] The superior wettability of GO-modified PEDOT:PSS surface compared to pristine GO was observed which may account for the formation of a high-quality perovskite layer with better crystallinity and reduced pin holes.[187] Another reason for the improved efficiency and stability of the GO/PEDOT:PSS-based devices is that the hygroscopic and low-conductive PSS at the PEDOT:PSS surface was partly removed during spin-coating with the GO solution, thereby improving the moisture resistance

and decreasing the contact barrier between the GO/PEDOT:PSS HTL and perovskite for enhanced hole-extraction.[192, 193]

For the PEDOT:PSS HTL in PSCs, the poly(styrene sulfonate) (PSS) templates are generally dispersed in water, which can dissolve the underlying perovskite films.[194] Snaith et al. and Brabec et al. introduced a water-free toluene-dispersed PEDOT HTL into the PSCs, which demonstrated improved performance.[195, 196] However, the relatively low performance of the PEDOT HTL-based PSCs remains an issue. The composite interfacial HTLs based on graphene derivatives have shown synergetic effects on charge-collection.[117, 197] Yeo et al. first applied this strategy in the n-i-p PSCs with a double interlayer HTL consisting of water-free PEDOT and fluorinated reduced graphene oxide (FrGO) (**Figure 18a)**.[29] Different from rGO or GO which cannot completely cover substrates with the spin-coating method,[173, 184] the FrGO layer can be uniformly deposited onto the PEDOT film via spin-coating due to the orthogonal solubility of the PEDOT in 2-propanol, which is also used to disperse FrGO.[29] The PEDOT-FrGO HTL-based devices showed higher internal quantum efficiency with broader photo-response from 300 nm to 800 nm.[29] The resulting fluorinated surfaces of the HTL led to more hydrophobic surfaces and higher work functions of the HTL with the average work function enhanced by ~0.2 eV compared to pristine PEDOT film. The change of the work function can be attributed to the reduced surface potential after incorporating FrGO in the HTL. The different surface potentials between PEDOT and FrGO induce interfacial dipoles at the PEDOT/FrGO interface pointing outward from FrGO.[198] Such dipoles can prevent undesirable recombination and accelerate hole transport by providing energy barriers and reinforcing the built-in potential across the device.[199, 200] Thus, enhanced V_{OC} and FF were

achieved.[29] The PEDOT-FrGO interlayer-based PSC exhibited a significantly improved PCE of 14.9%, a value larger than that measured for PEDOT HTL-based devices (PCE=10.3%).[29]

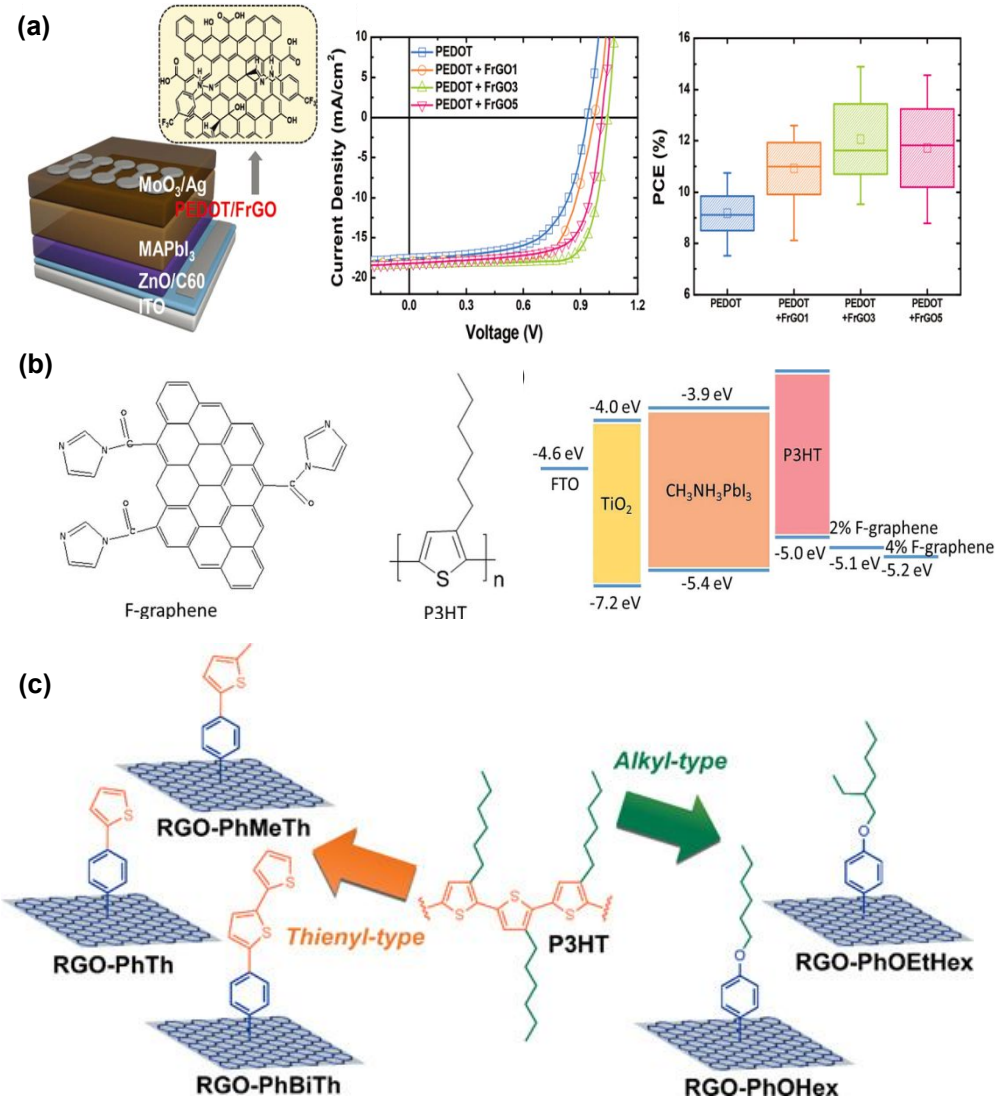

Figure 18. (a) Schematic architecture of a PEDOT/FrGO HTL-based PSC, and the chemical structure of FrGO; J-V curves of PSCs with different HTLs, and the corresponding PCE data. Reproduced from ref. [29] with permission from The Royal Society of Chemistry, copyright 2017. (b) The chemical structures of F-graphene and P3HT and the corresponding schematic energy diagram of PSCs using different amounts of F-graphene. Reproduced from ref. [201] with permission from The Royal Society of Chemistry, copyright 2016. (c) Schematic

illustration of the five types of functionalized RGO species. Reproduced from ref. [202] with permission from John Wiley and Sons, copyright 2018.

The more hydrophobic surface of PEDOT-FrGO HTL due to the graphitic 2-dimensional structure of the FrGO induced enhanced device stability. Devices maintained 70% of their initial PCE after 30 days of exposure to ambient atmosphere.[29]

P3HT is another HTL material that widely used in organic photovoltaic devices owing to its free dopant and facile processing without an extra oxidation step.[203] However, the conductivity of pure P3HT limited the hole transport of PSCs. Thus, it is necessary to enhance the hole mobility and conductivity of P3HT HTLs. Ye et al. dispersed functional graphene (F-graphene, GO modified by imidazole as shown in **Figure 18b**) in P3HT as the HTL in PSCs.[201] The F-graphene showed high mobility and conductivity which is favorable for HTLs in PSCs. According to the space-charge limited current test, the device with bare P3HT displayed a low hole mobility with a slope of 0.07, and was enhanced with a slope of 1.42 after incorporating F-graphene in the HTL. The work function changed from 5.0 eV to 5.2 eV when P3HT was modified with F-graphene.[201] This work function shift creates Ohmic contact between P3HT/F-graphene HTL and $MAPbI_3$ perovskite. $MAPbI_3$ readily crystallized with the (110) and (220) crystal planes of the F-graphene HTL-based PSCs.[201] As a result, PCEs up to 13.82% were achieved.[201] Compared to devices with a pure P3HT HTL, the incorporation of F-graphene led to a longer device lifetime. Due to the hydrophobicity of graphene composites, F-graphene-based PSCs contained nearly 70% of the pristine PCE after storage in atmosphere with a humidity of 20-40% for 8 weeks compared with only 35% of the original PCE remaining for bare P3HT-based devices.[201] Composites of rGO with P3HT have

been employed to greatly improve efficiency and stability in PSCs due to good hole mobility of rGO.[16] rGO and P3HT have the potential to establish π–π stacking interactions between their individual delocalized π electron clouds,[204] making the resulting composites stable. Unfortunately, this does not often occur due to the self-aggregation of pristine rGO. In this regard, chemical functionalization of rGO without disrupting the native electronic structure is useful to improve the dispersion of rGO composites.[205] Gatti and Menna et al. investigated the effect of the covalent functionalization of rGO flakes with different organic functional groups (**Figure 18c**) on the stability and homogeneity of their dispersion on the surface of P3HT HTL.[202] The five functional groups are 4-the (thien-2-yl)phenyl (PhTh), 4-(5-methylehien-2-yl)phenyl (PhMeTh), 4-[(2-2′-bithiophene)-5-yl]phenyl (PhBiTh), 4-(hexyloxy)phenyl (PhOHex) and 4-[(2-ethyl)hexyloxy]phenyl (PhOEtHex). The alkyl chain-contained PhOHex-functionalized P3HT exhibited the best dispersion, whereas rGO-PhBiTh@P3HT showed the highest surface roughness with graphene cluster, which acted as carrier recombination sites to diminish the extracted photocurrent.[202] The hexyl chain in PhOHex allows rGO to form a homogeneous film on the surface of the P3HT layer, yielding few protrusions on the HTL surface. In contrast, the bithienyl groups bound to the surface of rGO-PhBiTh@P3HT are prone to the formation of single flakes through the forming intramolecular π-stacking interactions to produce aggregated rGO flakes, resulting in short circuits between the perovskite and electrode and thus a low J_{SC}.[202] This work demonstrated the possibility to control the morphology of graphene derivatives dispersed within polymer HTLs by modifying the covalently grafted functional groups.

Graphene derivative-based composite HTLs carry enhanced mechanical, electrical and

optical properties over polymer HTLs as well as bare graphene derivative HTLs due to the large surface area for effective electrical conduction and carrier transfer, and the 2D functional surfaces enabling strong graphene derivative/polymer interaction. The superior properties of the HTL composites improve hole extraction and transport in PSCs. However, pristine graphene derivatives are usually incompatible with organic HTLs such as PEDOT and P3HT during actual operation. This leads to inferior optical and electrical properties of the composites. In order to improve the properties of the graphene derivative-based composite HTL, techniques aiming to improve the dispersion of graphene derivatives in polymer HTL need to be explored. Surface modification of graphene derivatives such as nucleophilic addition of organic molecules to the surface of graphene derivatives represents a promising route to achieve modified graphene with solvent dispersible properties, which will assist the preparation of graphene-based HTL composites.[206]

3.3.3 Hole Extraction and Transport Efficiency of Graphdiyne-Based Composites and Their Effect on Device Performance

As noted above, the conductivity of pure P3HT semiconductor is limited for hole transportation. Owing to its fascinating properties including excellent semiconducting properties, superior electrical properties and stability, graphdiyne (GD) has been reported to enhance the hole mobility and conductivity of P3HT HTL.[121] The structure of the GD-doped P3HT composite HTL is shown in **Figure 19a**. Strong π–π stacking interaction occurs between graphdiyne and P3HT. The HOMO level of the graphdiyne-P3HT HTL layer can be lowered while interchain hopping between the polymer chains and graphdiyne can be

enhanced due to the π–π stacking interaction.[121] In this way, electrons can be partially transferred from P3HT to GD (**Figure 19b)**. Furthermore, the addition of GD enhanced light

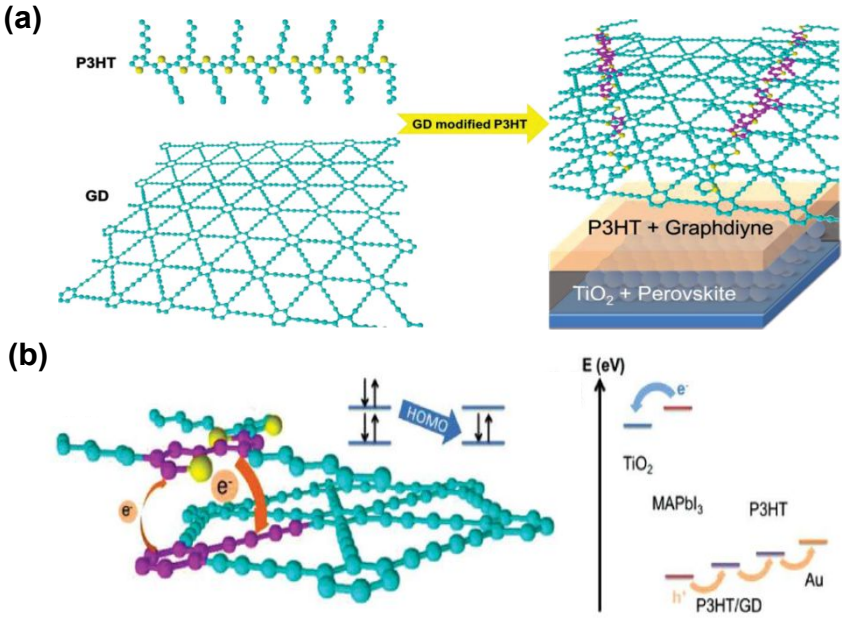

Figure 19. (a) Schematic of PSCs with P3HT HTLs modified with GD. (b) The atomic-level interaction between GD, P3HT and charge carriers, and the energy levels in P3HT/GD-based PSCs. Reproduced from ref. [121] with permission from John Wiley and Sons, copyright 2015.

absorption in PSCs because of the improved scattering nature of graphdiyne. The PCE and stability of GD/P3HT-based devices are superior to pristine P3HT-based devices.[121] It is proposed that doping of GD into polymer HTLs renders uniform heterogeneous nucleation of perovskite and thus facilitates perovskite crystal growth by improving the surface wettability of HTLs.[207] When GD was doped into a polymer P3CT-K HTL, a decreased contact angle measured by using DMF and DMSO as solvent at V_{DMF} and V_{DMSO} of 4:1 was observed from 12° to 4°,[207] which is beneficial to the flow and spread of the perovskite precursors to yield uniform perovskite films.[179]

As a new carbon allotrope, GD exhibits an attractive structure and physical properties, as well as greater potential than many other carbon materials for applications in solar cells. However, GD-based PSCs are rarely reported. One major challenge is the preparation of a large amount of GDs with high purity.[208] The development and optimization of the processing methods to create well-defined GD nanostructures is still in its infancy. The ability to achieve well-defined GD or GD-based nanostructures with competitive optical and electrical properties and clarify the underlying operating mechanisms may significantly impact both fundamental study and further potential applications of GD.

3.3.4 Hole Extraction and Transport Efficiency of Transition Metal Dichalcogenides and Their Effect on Device Performance

Unlike graphene's single atomic layer of carbon, transition metal dichalcogenides (TMDs), such as molybdenum disulfide (MoS_2), tungsten disulfide (WS_2), molybdenum diselenide ($MoSe_2$), and tungsten diselenide (WSe_2), consist of a "sandwich" structure of a transition metal layer between two chalcogen layers. This unique structure determines their distinctive optical and electro-catalytic characteristics as well as chemical stability.[41] The electronic and optical properties significantly change depending on the number of layers. For example, the band energy of MoS_2 increases from 1.29 (multilayer MoS_2) to 1.9 eV (monolayer MoS_2), and the band gap goes from being indirect to direct as the layer number decreases.[209] Furthermore, TMDs possess superior charge carrier capabilities making them applicable in next generation HTLs for use in high-performance PSCs. However, currently only limited work has been done on the incorporation of TMDs into PSCs.

The work functions of MoS_2 and WS_2 are similar to GO with values of 5.0, 4.95, and 5.1 eV, respectively.[124] When using MoS_2, WS_2, and GO as HTLs in an inverted $CH_3NH_3PbI_{3-x}Cl_x$ PSC, the PCEs of the MoS_2 and WS_2-based PSCs are comparable to those obtained from GO or PEDOT:PSS-based devices.[124] The lone-pair electrons of the chalcogen atoms in the isolated monolayer structure of TMDs allow for significantly enhanced transport which can improve carrier mobility in devices.[210] Furthermore, the energy levels of TMD layers can be modulated by simple surface treatments. These results indicate that TMDs such as MoS_2 and WS_2 can be promising candidates as HTLs in PSCs. It is well known that 2D MoS_2 and WS_2 have two phases, the semiconducting trigonal prismatic (2H phase) and the metallic octahedral (1T phase).[211] The effect of the crystal structure has been previously discussed elsewhere.[212] Zhou, Song et al. used MoS_2 and WS_2 as HTLs in p-i-n type PSCs.[125] It was found that the content of 1T phase in the HTLs significantly contributed to the improved PCEs. The 1T-rich (2H-poor) TMDs showed improved performance over 1T-poor (2H-rich) TMDs due to the better extraction ability of charge carriers in the 1T phase which exhibited a completely quenched PL.[125] The 1T TMDs possess much higher conductivity than the 2H phase TMDs.[213] The electronic properties of the 1T phase suggested its metallic nature, with an estimated high carrier concentration of $>10^{13}$ cm^{-2}.[213] The highest PCEs for 1T-rich MoS_2 and WS_2-based PSCs were 14.35% and 15.00%, respectively. The small difference between the PCE of MoS_2 and WS_2 is due to the latter showing a higher work function of 5.18 compared to 5.13 for MoS_2; a value closer to the valence band of perovskite. Thus, a higher V_{OC} is achieved.[125] Compared with PEDOT:PSS, these 1T-rich TMD HTLs can further enhance the performance and the stability of PSCs because of the improved

moisture resistance.[125] Another reason for the inferior performance of the 2H phase-TMD HTL-based PSCs compared with that of 1T phase-TMD HTL-based PSCs may be due to the formation of a type-I band-alignment (straddling gap) with $MAPbI_3$ as shown in **Figure 20a**.[214, 215] According to band edge analysis using ultraviolet photoelectron spectroscopy, the valence band maximum (VBM) of $MAPbI_3$ films is -5.79 eV; a value higher than the VBM of the MoS_2 monolayer (-6.28 eV). [214, 215] This prevented the efficient extraction and transport of holes from the perovskite to the MoS_2 HTL. To deepen the work function of MoS_2 and form a type-II heterojunction (staggered gap) between MoS_2 and $MAPbI_3$, mild UV ozone (UVO) treatment is an efficient method which can create sulfur vacancies within MoS_2 and form p-type doping to lower the Fermi level of MoS_2.[216] The band edge state-filling in perovskite slows when the photo-induced holes in perovskite are transferred into the sulfur vacancy-engineered MoS_2.[216] The hole transfer time from $MAPbI_3$ to MoS_2 was estimated to be ~490 ± 50 fs. [216] Thus, the introduction of sulfur vacancies via plasma treatment may open routes to ultrafast hole transfer from $MAPbI_3$ to MoS_2. The PL spectra quenching (**Figure 20b**) suggests efficient hole transfer from the perovskite layer to the UVO-treated MoS_2 layer.[214]

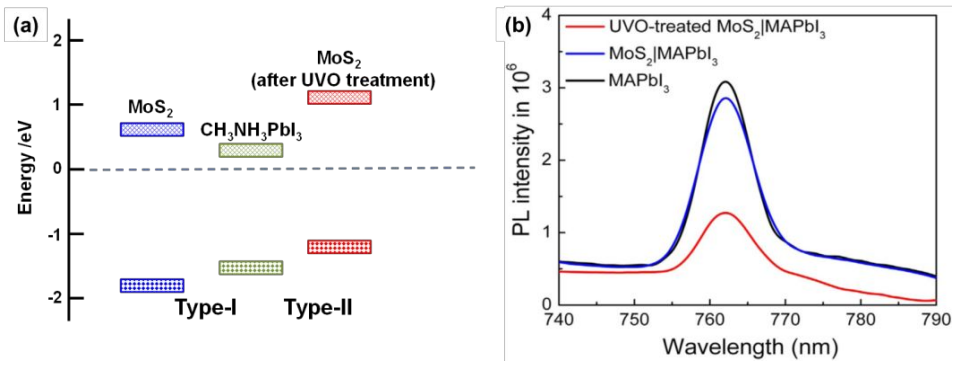

Figure 20. (a) band-diagram of $MoS_2/MAPbI_3$ heterojunctions based on two types of MoS_2

with type I and type II heterojunctions illustrated; Fermi energy after alignment is shown as a dashed line. (b) PL spectra of perovskite layer on quartz, pristine and UVO-treated MoS_2 layers. Reproduced from ref. [214] with permission from Elsevier, copyright 2017.

In addition to MoS_2, TiS_2, another TMD that had been investigated, exhibits a good electrical conductivity (≈ 103 ohm^{-1} cm^{-1}) and a suitable valence band edge, which is only 0.15 eV lower than that of $MAPbI_3$, indicating a favorable energy level alignment.[15, 217] TiS_2 has the added advantage of being $1/30^{th}$ the cost of the widely used spiro-OMeTAD HTL. Nazeeruddin et al. introduced TiS_2 HTLs into n-i-p type mesoposcopic PSCs (**Figures 21a-21c**).[15] The TiS_2-based cell exhibited a high PCE of 13.5% under full sun illumination; comparable to spiro-OMeTAD-based devices (**Figures 21d-21f**). The presence of a TiS_2 layer on perovskite led to a nanostructured perovskite morphology although the average crystal grain size of perovskite remained the same before and after the TiS_2 deposition. It was found that the spin-coating rate had a significant impact on the perovskite morphology. High rates led to improved coverage of the perovskite layer, whereas the roughness of the perovskite film increased significantly due to the large distribution of TiS_2 particles obtained for speeds lower than 5000 rpm.[15]

Although TMDs have promising electrical and optical properties, it remains challenging to mass-produce them. Furthermore, their low solubility in most common solvents makes it difficult to prepare them by simple solution processes. To address these limitations, strategies for functionalizing TMDs were investigated and found to be efficient for enhancing their solubility.[218] After functionalizing 2H-phase MoS_2 with phenyl acetylene silver (PAS), MoS_2 showed good dispersion in polar solvents such as DMF and water.[218] By blending

PEDOT:PSS with MoS_2-PAS to serve as the HTL, planar heterojunction PSCs demonstrated an enhanced PCE and stability. The PCE of the devices increased from 14.69% to 16.47% after incorporating MoS_2-PAS with PEDOT:PSS as the HTL. There was only a 13% reduction

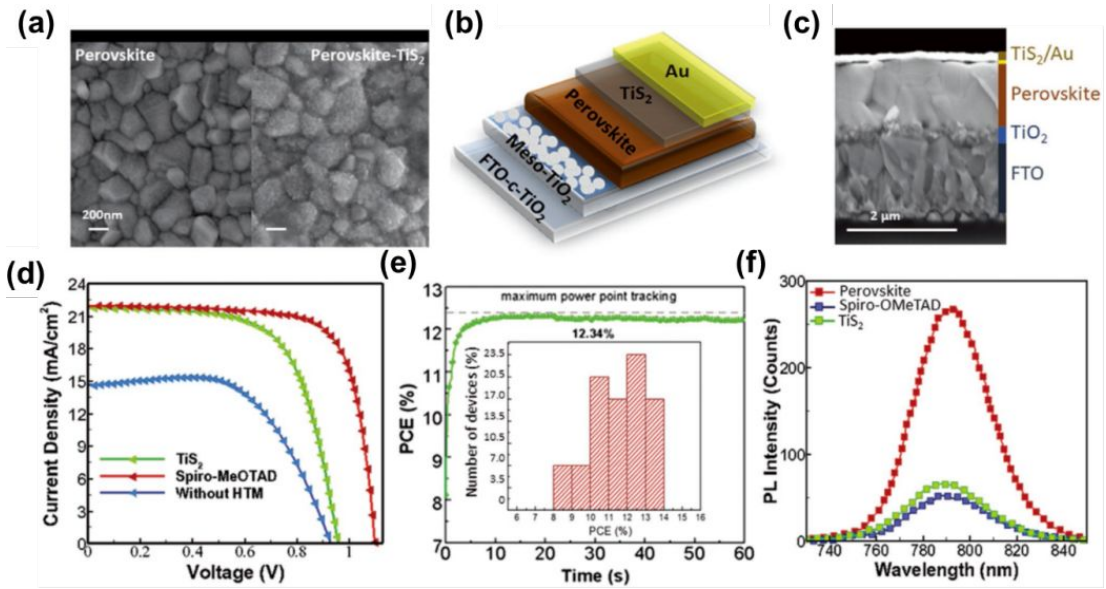

Figure 21. (a) SEM images of perovskite and perovskite-TiS_2 films. (b) Schematic and (c) cross-sectional SEM image of a typical TiS_2 HTL-based PSC device. (d) J-V curves of devices using TiS_2 and spiro-OMeTAD as the HTLs and a device without an HTL for comparison. (e) Maximum power point tracking (MPPT) of one of the best performing TiS_2-based devices. Inset: Histogram of PSC efficiencies obtained from more than 50 TiS_2-containing devices. (f) Steady-state PL spectra of PSCs containing TiS_2, and spiro-OMeTAD as HTLs as well as a device with no HTL for comparison. Reproduced from ref. [15] with permission from John Wiley and Sons, copyright 2017.

in initial PCE after 10 days of storage in ambient atmosphere owing to the hydrophobicity of

MoS_2-PAS. For comparison, there was a 54% decrease in the initial PCE for the device without MoS_2-PAS.[218] Another issue for TMD-based HTL in PSCs (especially in n-i-p devices) is that the choice of deposition method is limited because the perovskite layer is sensitive to a variety of solvents. As such, more efficient functional groups need to be explored to increase the solubility of these TMDs in the solvents such as isopropyl alcohol and chlorobenzene, which have less impact on the degradation of perovskite films.

3.3.5 Hole Extraction and Transport Efficiency of Other Two Dimensional Materials and Their Effect on Device Performance

BP (called phosphorene when in monolayer form) is a promising 2D nanomaterial due to its suitable electronic and optoelectronic properties.[25, 219-221] Similar to graphene and MoS_2, monolayer phosphorene is flexible, stable and can be mechanically exfoliated. Unlike graphene, BP has a direct band gap. The E_g of single-layer phosphorene is ~ 2.0 eV.[222] When the BP layer number increases, the E_g reduces, reaching a limit of 0.33 eV in the bulk[220] thus providing a large range of values for energy level matching in different device configurations. Interestingly, the direct band gap of BP is independent of the layer number due to the strong conduction band wave function overlap.[67, 223] BP exhibits a carrier mobility up to ~1000 cm^2/V-S at room temperature.[224] Thus, it is a promising candidate as a HTL in PSCs. Mhaisalkar, Mathews et al. introduced liquid exfoliated few-layer 2D BP nanosheets as a HTL for mesoscopic PSCs with a device architecture of FTO/blocking layer TiO_2/mesoporous TiO_2/$MAPbI_3$/BP/Au (**Figure 22).**[25] The low valence band of BP nanosheets (-5.2 eV, **Figure 22a**) favors hole injection from $MAPbI_3$ which has a valence band level of -5.4 eV. A PCE of

7.88% was achieved in BP-based PSCs, 4% higher than that observed for HTL-free devices. When using BP nanosheets + spiro-OMeTAD as a HTL, a 25% improvement in PCE from 13.1% (spiro-OMeTAD only) to 16.4% was observed.[25] These early findings strongly suggest that BP nanosheets are a good material for the HTL material in PSCs.

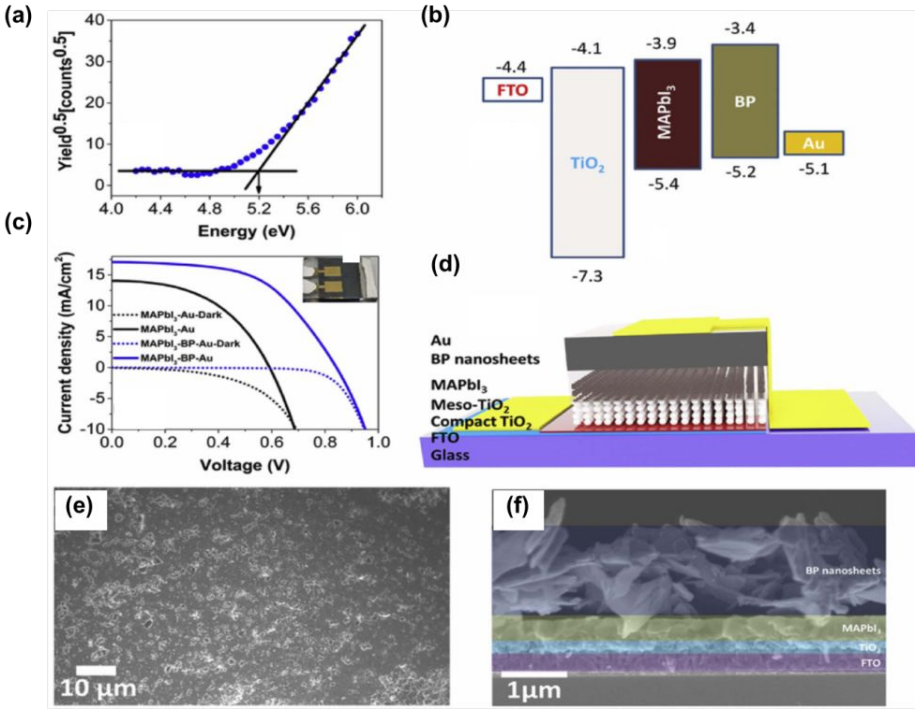

Figure 22. (a) Photo-electron spectroscopy measurement; (b) band alignment of PSCs based on BP HTLs, (c) J-V curve of PSCs with (blue) and without (black) BP HTL. (d) schematic of PSC with BP, (e) FE-SEM image of BP on $MAPbI_3$, and (f) cross-sectional FE-SEM image of a PSC with BP HTL. Reproduced from ref. [25] with permission from Elsevier, copyright 2017.

All-inoganic novel halide perovskite $CsPbI_3$ and BP heterostructures with two kinds of typical van der Waals-type electrical contacts, i.e., the electrical contacts of the Pb-I interface and Cs-I interface with BP, were constructed by first-principle calculations for exploring the structural, electronic, and optical properties of the perovskite/BP interfaces.[225] It was found that the heterostructure of the Pb-I interface contacting with BP showed the type-I band

arrangement. Whereas, the Cs-I interface contacting the BP demonstrated a type-II band arrangement.[225] The energy level shift can be attributed to the work function difference of $CsPbI_3$ slabs relative to the BP monolayer, driving the movement of carriers spontaneously.[225] In view of the energy alignment, the heterostructure of Cs-I interface of $CsPbI_3$ in contact with BP has great potential for PSCs.[225] Light absorption, especially in the infrared region, is enhanced in $CsPbI_3$-BP heterostructures, thereby improving the potential harvesting of infrared photons in PSCs. Similar heterostructures were constructed between 2D perovskites M_2XBr_4 [M = $(C_4H_9NH_3)^+$; X = Pb^{2+}, Sn^{2+}, Ge^{2+}] and BP.[226] The M_2SnBr_4-BP and M_2GeBr_4-BP heterostructures showed type-II band alignment, whereas the M_2PbBr_4-BP heterostructure exhibited type-I band alignment. [226] Among the three perovskites, the BP increased the light absorption of M_2GeBr_4 the most. In consideration of the energy levels, barrier heights, and light absorption, the M_2GeBr_4/BP heterostructure stood out as the best HTL candidate for PSCs.[226] On the basis of these studies, it is clear that heterostructures between perovskite and BP can efficiently tune the optical and electrical properties of the interface. To achieve high-performance BP-based PSCs, it is imperative to tailor the elemental composition of perovskite and types of electrical contacts between perovskite and BP.

A few metal oxide nanosheet materials were also investigated for use as HTLs in PSCs due to their large specific surface area which can enable effective charge diffusion.[227] Yu et al. fabricated $MAPbI_3$ PSCs using mesoscopic TiO_2 nanosheets and NiO nanosheets as ETLs and HTLs, respectively.[228] The nanosheet-based PSC with printable carbon counter electrodes showed higher PCEs than devices using NiO nanoparticles as the HTL under AM 1.5 G

illumination. Clearly, nanosheet-structured PSCs can reduce electron-hole recombination and enhance the collection of charge carriers.[228] Compared with NiO nanoparticle HTLs, the nanosheet structure can supply a direct pathway for charge transfer. In addition, 2D NiO nanosheets possess high porosity and large surface area facilitating perovskite loading and diffusion further leading to increased photo-generated electron-hole pairs.[229] NiO nanosheet-based devices showed a higher J_{SC} of 11.2 mA cm^{-2} and an improved V_{OC} of 1.01 V compared to nanoparticle-based counterparts, leading to an average PCE of 7.50%. A higher FF of 0.66 suggests a smaller series resistance and larger shunt resistance for devices with NiO nanosheet HTLs.[228]

3.4 Effect of Two Dimensional Material-based Buffer Layers on Carrier Dynamics and Performance of Perovskite Solar Cells

PSC device performance is governed not only by the electronic energy levels and charge carrier mobility of the HTL and ETL materials, but also by the effective charge extraction from the perovskite layer and charge collection by the electrodes. An effective approach to improve the latter two aspects is to incorporate additional buffer layers at the ETL/absorber/HTL/electrode interlayers of the PSC structure. These buffer layers can improve the extraction and collection of carriers. The introduction of buffer layer aims to decrease the trap states induced by the large lattice mismatch between the interfaces, suppress charge recombination and enhance photovoltaic performance.[230]

3.4.1 Graphene Oxide Buffer Layers at the Hole Transporting Layer/Electrode Interface for Improved Device Stability

2D GO was chosen as a buffer layer in PSCs because of its high band gap, transparency and mesoporous structure.[21, 91, 127, 231] In addition, carbon nanostructures in PSCs can improve the stability of the cells due to their hydrophobicity.[16] Arora, Dar et al. demonstrated a mesoscopic PSC using a thin and uniform CuSCN layer as the HTL and a $CsFAMAPbI_{3-x}Br_x$ ($MA = CH_3NH_3^+$, $FA= CH(NH_2)_2^+$) perovskite layer as the absorber.[127] CuSCN HTLs have high hole mobility (0.1 $cm^2\ V^{-1}\ s^{-1}$) and well-aligned work functions which facilitate fast carrier extraction and collection.[232] The CuSCN-based PSC achieved an efficiency exceeding 20%. However, due to the degradation of the CuSCN/Au contact induced by reaction between gold and thiocyanate ions and formation of an undesirable barrier layer, the operational stability is poor.[127] The addition of an rGO spacer layer between CuSCN and Au enabled PSCs to retain > 95% of their initial efficiency after aging for 1000 h at 60°C. These graphene-CuSCN-based devices surpass the stability of spiro-OMeTAD-based PSCs.[127] The effect of graphene as an interlayer between the Au electrode and spiro-OMeTAD HTL was also studied in planar PSCs.[61] Stability testing showed that more than 94% of the initial PCE in graphene-based devices was retained after ageing in 45% humid air for 96 h or thermal annealing at 80 °C for 12 h. These performance values clearly support the importance of graphene layers in improving PSC stability across many different material compositions. This graphene interlayer can block the diffusion of air and Au into the perovskite layer after annealing treatment which further reduces carrier recombination.[61]

3.4.2 Graphene Derivative and MoS_2 Buffer Layers at the Perovskite/Hole Transporting Layer Interface for Improved Hole Extraction from Perovskite

The deposition of a buffer layer between the perovskite and HTL can also improve PSC performance. It was found that metal can migrate from the electrode through the HTL and eventually contact the perovskite. This is in part responsible for PSC device degradation. [233] The contact between metal and perovskite leads to a low shunt resistance during aging and in turn the degradation of PSCs.[233] Depositing HTL within a buffer layer can prevent metal migration while blocking the shunt pathway that can arise during aging. The consequence of the introduction of such a buffer layer is a considerable improvement in the V_{OC} and FF as well as the device stability.[21, 91] A thin layer of GO nanosheet employed as a buffer layer sandwiched between the perovskite and the HTL tetra-n-butyl-copper phthalocyanine (CuBuPc) was found to inhibit the formation of shunting pathways and improved HTL morphology.[231] The presence of the GO buffer layer prevented the formation of aggregated structures with voids in CuBuPc and thus blocked the shunt paths. The GO buffer layer facilitated hole transport between the perovskite and the CuBuPc layer. The efficiency of GO-based solar cells increased to a maximum of 14.4%, whereas devices without the GO layer achieved a maximum PCE of 7.3%. It was also found that the GO buffer layer at the perovskite/HTL interface can improve the contact between the absorber layer and the HTL.[21] The surface contact angle of PSCs decreased from 13.4^{o} to zero degrees (fully wetting) after introducing GO as the buffer layer. This can be ascribed to the amphiphilic nature of GO. The decreased contact angle led to an enhancement of the short circuit current due to the improved contact between the perovskite and the HTL.[21]

On the basis of the discussion noted above, GO appears to be a good buffer layer candidate used between perovskite and HTL to improve the efficiency and stability of

devices. However, one major risk is that GO may accelerate the degradation of perovskite once the active layer is decomposed in air. Carlo et al. investigated the stability of PSC devices using graphene-doped mesoporous TiO_2 ($mTiO_2$ + G) as the ETL and GO as the buffer layer between the perovskite active layer and the spiro-OMeTAD HTL.[234] Four cells with different structures were designed (**Figure 23a-24f)**. Device C, using $mTiO_2$ + G as the ETL, showed remarkable stability with 88% retention of the initial PCE value after 16 h of thermal stress testing.[234] Under the same conditions, the perovskite/GO/HTL interface (device B) suffered degradation because the GO layer was reduced upon irradiation.[234] In the presence of O_2 and H_2O, $MAPbI_3$ single crystals can undergo decomposition with the release of $CH_3NH_2^+$ and HI.[235] HI can reduce GO to rGO which may react with photo-generated electrons and further accelerate the decomposition of the perovskite.[236] Thus, rGO may not be a promising alternative as the buffer layer between perovskite and HTL in PSCs. However, the use of a functionalized rGO instead of pristine rGO as a buffer layer in PSCs may change the situation. Wang et al. introduced 4-fluorophenyl-functionalized rGO (rGO-4FPH) as an interfacial layer between the perovskite and HTL.[22] The 4-fluorophenyl functionalization passivated the traps on the surface and at the grain boundaries within the perovskite layer by interacting with the under-coordinated Pb ions in the perovskite layer.[22] As a result, it reduced interfacial recombination and enhanced hole extraction efficiency which further enhanced the V_{OC}. The rGO-4FPH-based PSC achieved a V_{OC} of 1.11 V and a PCE up to 18.75%.[22] Despite similar stability for devices both with and without a buffer layer in air (with humidity at approximately 30%), a slightly higher stability under glovebox illumination was observed after the incorporation of the buffer layer in the devices.[22] A hybrid structure with MoS_2

quantum dot (QDs) and functional rGO (obtained by chemical silanization-induced linkage between rGO and (3-mercaptopropyl)trimethoxysilane) in PSCs was designed as buffer layers between $MAPbI_3$ and spiro-OMeTAD.[237] As shown in **Figure 23g**, the functional molecules anchored onto the rGO enabled f-rGO to interact with MoS_2 QDs.[237] The van der Waals

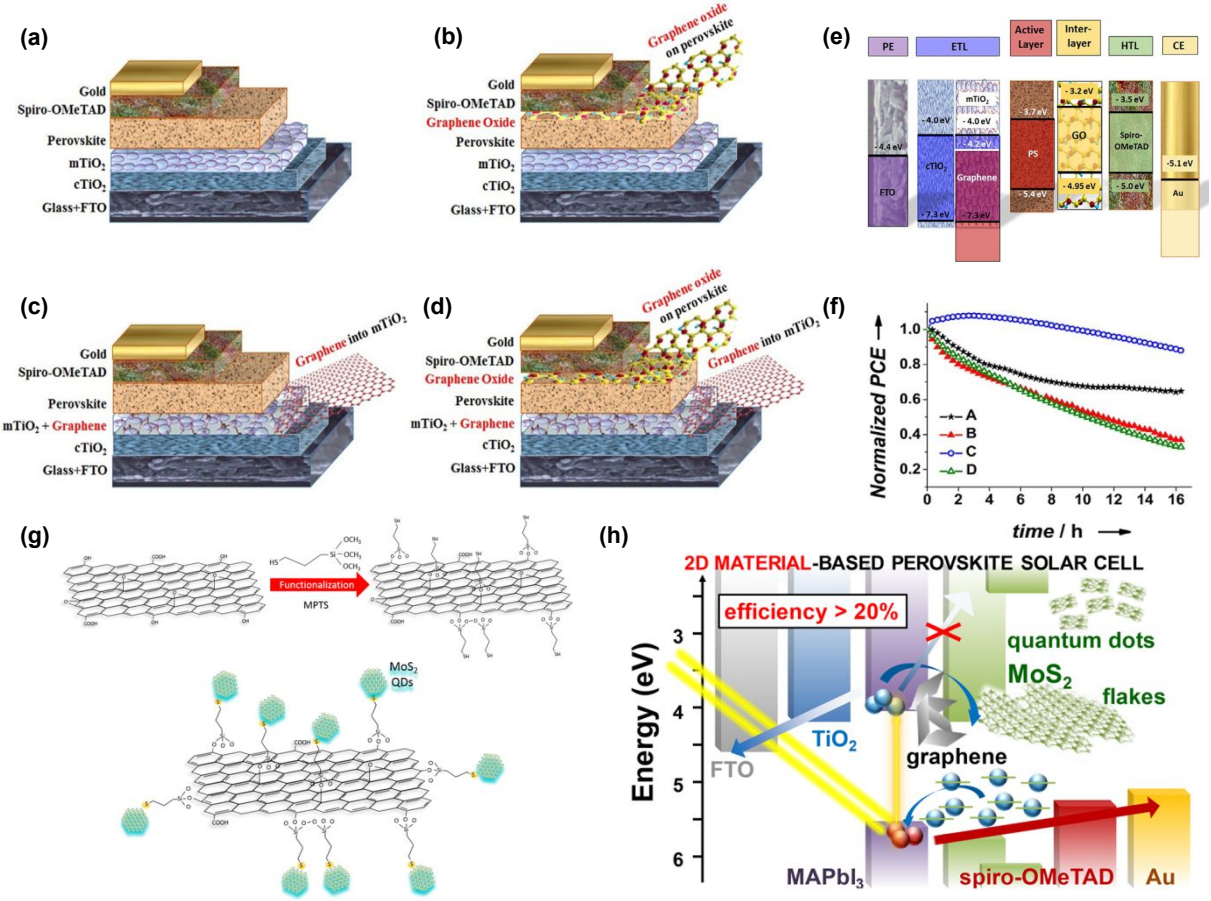

Figure 23. PSC structures (a) without a buffer layer between the perovskite and spiro-OMeTAD layers (device A), (b) with graphene oxide (GO) as an interlayer between the perovskite and spiro-OMeTAD layers (device B), (c) with mesoporous TiO_2 ($mTiO_2$) + graphene (G) interlayer (device C), and (d) combined device with the layer structure FTO/contact TiO_2 ($cTiO_2$)/$mTiO_2$ + G/perovskite/GO/spiro-OMeTAD/Au (device D), and (e) energy band diagram of the different functional layers in a PSC relative to vacuum. The band alignments are not to scale and show only the relative position of the energy levels. (f) PCE

trends versus time under extended 1 sun illumination at maximum power point polarization provided by a calibrated white LED for devices A through D. Reproduced from ref. [234] with permission from John Wiley and Sons, copyright 2016. (g) Schematic illustration of the functionalization of rGO (upper panels) and the hybridization of MoS_2 QDs and rGO (lower panel). (h) Schematic of the energy band edges of materials used in the rGO/MoS_2 QDs buffer layer-based PSC. Reproduced from ref. [237] with permission from American Chemical Society, copyright 2018.

hybridization of MoS_2 QDs with rGO enabled a uniform deposition of HTLs or buffer layers onto the perovskite film owing to the filling of pinholes of the MoS_2 QD films by rGO.[237] MoS_2 QDs provide both hole-extraction and electron-blocking properties due to their suitable energy alignment with perovskite (**Figure 23h**). Effective collection of the photo-generated holes from perovskite towards the anode was achieved, reaching a maximum PCE of 20.12%.[237] The rGO buffer layer-based PSCs exhibited a reduced PCE of only 8.8% after a 1032 h of aging. This is significantly lower than devices without the buffer layer (PCE = 24.6%).[237] The improved stability can be attributed to the surface passivation of the perovskite layer rendered by the rGO buffer layer. A TDM composed of liquid-phase exfoliated few-layer MoS_2 flakes has also been exploited as an active buffer layer in PSCs with a layer structure of glass/FTO/cTiO_2/mTiO_2/$CH_3NH_3PbI_3$/MoS_2/Spiro-OMeTAD/Au.[126] The MoS_2 buffer layer serves two functions; first, it forms a barrier preventing metal electrode migration, second it serves as an energy-matching layer to further ease hole

collection from the spiro-OMeTAD HTL for transport to the electrode. As a result, the MoS_2-incorporated PSCs (0.1 cm^2 active area) achieved a higher PCE (13.3%) and improved stability over a period of 550 h (93% peak PCE retention vs 66% PCE retention for reference cell without the MoS_2 buffer layer.[126]

3.4.3 Graphene Oxide Buffer Layers at the Perovskite/Electron Transporting Layer Interface Lead to Improved Electron Extraction from Perovskite

Modifying the interface between the ETL and perovskite layer is proposed as an effective way to boost PCE of PSCs by limiting the charge losses occurring at the perovskite/ETL interface, simultaneously improving the device stability. Bonaccorso, Carlo et al. introduced the concept of graphene interfacial engineering using lithium-neutralized graphene oxide (GO-Li) flakes as an interlayer between the mesoporous TiO_2 ($mTiO_2$) and perovskite layers to improve charge injection from the perovskite layer into the $mTiO_2$ layer.[20] Graphene flakes were also dispersed into the $mTiO_2$ ETL layer to facilitate electron transport. The fabricated PSC architectures are shown in **Figure 24**. An increased electron injection from the perovskite to the $mTiO_2$ layer and a reduction in back-transfer processes from the $mTiO_2$ to the perovskite layer were observed as a result of the GO-Li buffer layer. A significant improvement in the average J_{SC} (+18%) was observed for device B. Meanwhile, there is a 4.3% loss in V_{OC} due to a downward displacement of the conduction band of TiO_2.[20] In contrast, device D with graphene flakes incorporated into the TiO_2 layer did not show a reduction in V_{OC}. First-principle calculations on graphene/$MAPbI_3$ interfaces suggested that graphene can suppress the octahedral tilt of perovskite, leading to a ferroelectric distortion

with a permanent polarization.[238] Such polarization drives electron extraction from the perovskite into the ETLs. A PCE of 12.6% on an over 50 cm^2 active area of PSCs was achieved in the presence of the GO-Li buffer layer.[20]

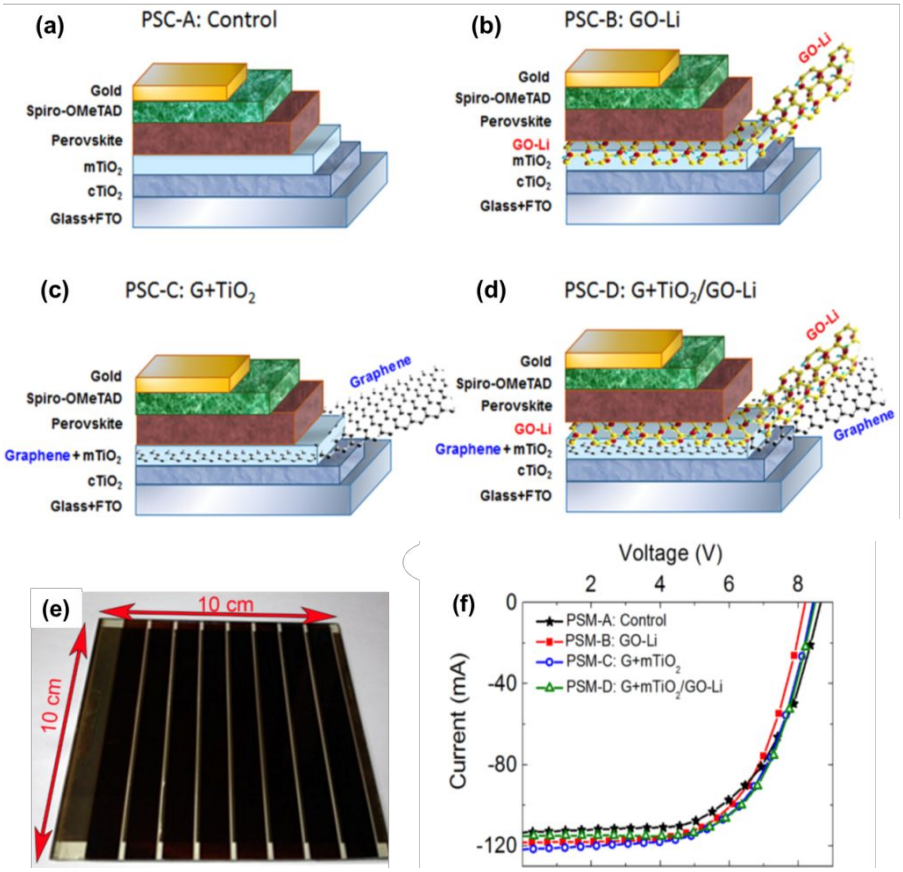

Figure 24. PSC layer structures (a) with the reference mesoscopic structure FTO/$cTiO_2$/$mTiO_2$/perovskite/spiro-OMeTAD/Au, (b) with the GO-Li buffer layer between perovskite and $mTiO_2$ layers, (c) with graphene-doped $mTiO_2$ as the ETL, and (d) with GO-Li as the buffer layer and graphene-doped $mTiO_2$ as the ETL. (e) Photograph of a large-area PSC device (50 cm^2 active area). (f) J−V characteristics of the different modules tested. Reproduced from ref. [20] with permission from American Chemical Society, copyright 2017.

4. Tunable Optoelectronic Properties of 2D Perovskite Absorbers and Their Effect on Device Performance

2D perovskite active layer materials in solar cells exhibit excellent photoelectric conversion efficiencies while maintaining the excellent light absorption properties of three-dimensional perovskites.[239-241] 2D perovskite is a direct band-gap material in which the process of exciton generation is very fast.[80] It was found that the photo-generated holes and electrons in layered 2D perovskites could be transferred in different directions within the perovskite film, and further accumulated at the top and bottom of the film, respectively.[242] Consequently, charge collection at the electrodes became easier. Compared to traditional 3D $MAPbI_3$ perovskite, the layered 2D perovskite structure offers greater tunability at the molecular level for optimizing optical and electrical properties of materials.[130] Single-crystalline $(C_4H_9NH_3)_2PbBr_4$ prepared via separating the individual layers of $PbBr_4^-$ was first reported in 2015.[241] As-grown 2D perovskite sheets exhibited high PL quantum efficiency as well as wide composition and color tunability by changing the perovskite sheet thickness.[241] A slightly increased optical band gap of the 2D hybrid perovskite sheets with respect to the bulk crystal was observed. This is likely induced by the lattice expansion.[241] The larger bandgap of the 2D perovskite structure is also suitable as the higher bandgap absorber in a dual-absorber tandem device.[130]

Garner et al. optimized 2D perovskite structures by varying the length of the organic chain on the diammonium cations.[243] The investigated perovskite materials include $[NH_3(CH_2)_4NH_3]PbI_4$ ($BdAPbI_4$), $[NH_3(CH_2)_6NH_3]PbI_4$ ($HdAPbI_4$), and $[NH_3(CH_2)_8NH_3]PbI_4$ ($OdAPbI_4$) with band gaps of 2.37, 2.44 and 2.55 eV, respectively.[243]

Compared to traditional $MAPbI_3$, these 2D perovskites have larger band gaps and lower photo-conductivity. The performance of PSCs using 2D perovskite materials as the light absorbing layer was investigated as well. As the whole process of solar cell fabrication (except for the silver evaporation process) is performed in ambient air (with a humidity of 55.6%) and at ambient temperature (23.4 ^oC), the moist conditions produce PSCs with overall poor quality. The best performing material was $BdAPbI_4$ with a PCE of 1.08% comparable to that of $MAPbI_3$-based solar cells (2.1%).[243] However, the stabilities of $BdAPbI_4$- and $HdAPbI_4$-based PSCs (PCE drop from 1.082% to 0.798% and 0.592% to 0.339% after 4 days, respectively) are superior to $MAPbI_3$-based devices (PCE drop from 2.11% to 0.03% over the same period). The devices are also thermally stable up to 200 ^oC.[243] Zhou et al. fabricated ternary cation halide quasi-2D perovskite active layer materials such as $(BA)_2(MA,FA)_3Pb_4I_{13}$ (where BA = n-$C_4H_9NH_3$, MA = methylamine, FA = formamidinium), in which MA is gradually replaced by FA.[244] It was found that the incorporation of FA^+ can improve perovskite crystallization to enable the reduction of non-radiative recombination centers. An in-situ PL technique was employed to probe the phase formation sequence wherein the 2D $(BA)_2(MA, FA)_{n-1}Pb_nI_{3n+1}$ phase (n = 2, 3, 4) formed early, followed by the generation of $(MA, FA)PbI_3$ ($n = \infty$) in a quasi-2D perovskite system.[244] A peak efficiency of 12.81% was reported for such 2D perovskite-based solar cells (**Figure 25a)**. In order to further improve the properties of 2D $(BA)_2(MA, FA)_3Pb_4I_{13}$ perovskite, cesium cations (Cs^+) were doped into the structure (**Figure 25b**).[245] These devices exhibited maximum PCE of 13.68% with excellent moisture tolerance and thermal stability.[245] Cs^+ plays a key role in controlling the oriented growth of perovskite crystals and increasing the crystal dimension. As a result, Cs^+

doping improves the optoelectronic properties by reducing trap density, increasing charge-carrier mobility, and increasing charge-transfer kinetics. Docampo et al. developed a facile solution-based cation infiltration process to produce a hybrid 2D/3D perovskite film in which 2D layered perovskite (LPK) is deposited onto methylammonium lead iodide (MAPI)

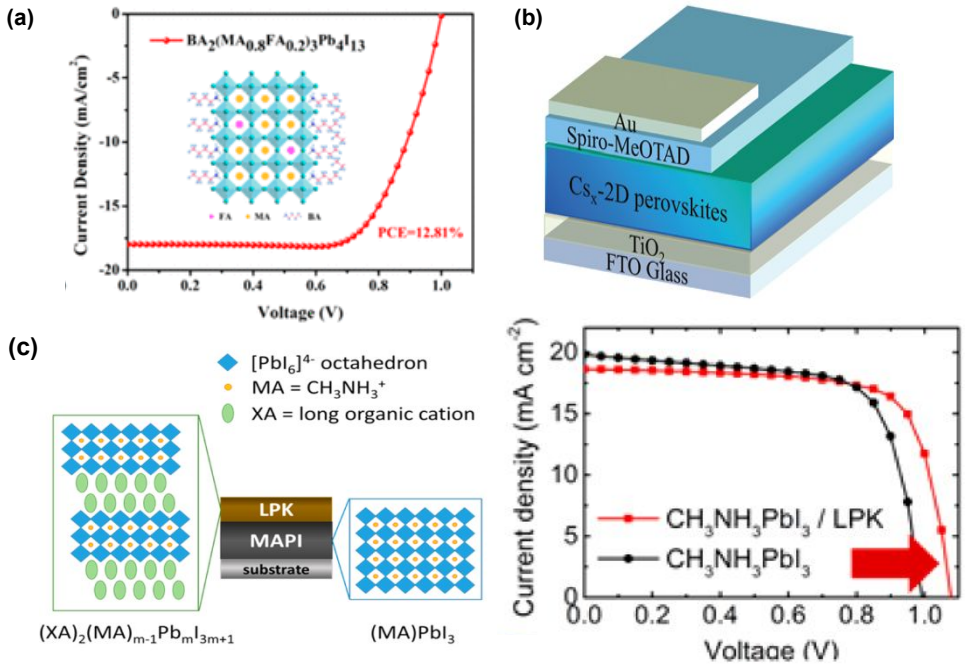

Figure 25. (a) PL measurement for a $(BA)_2(MA, FA)_{n-1}Pb_nI_{3n+1}$ film produced by detecting the emission peak at 585 nm (n = 2), 670 nm (n = 4), and 780 (n = ∞), and the J-V curve of a $(BA)_2(MA_{0.8}FA_{0.2})_3Pb_4I_{13}$-based PSC; inset is the crystal structure of $(BA)_2(MA_{0.8}FA_{0.2})_3Pb_4I_{13}$. Reproduced from ref. [244] with permission from American Chemical Society, copyright 2018. (b) Device architecture of a Cs_x-incorporated 2D perovskite-based PSC. Reproduced from ref. [245] with permission from The Royal Society of Chemistry, copyright 2017. (c) Crystal structures of methylammonium lead iodide (MAPI) and a layered perovskite (LPK) with their performance in solar cells. Reproduced from ref. [246] with permission from American Chemical Society, copyright 2016.

films (**Figure 25c**).[246] The MAPI/LPK heterojunction system incorporating phenylethylammonium has a PCE up to 16.84% due to the increased V_{OC} and FF which are related to a reduction in charge recombination. The top layer of the 2D LPK can act as a selective charge extraction layer for the MAPI perovskite leading to suppressed recombination of photo-generated carriers.[246] These results suggest that the formation of a 2D perovskite interface on top of the $MAPbI_3$ perovskite improves the photovoltaic and optoelectronic properties of the overall PSC device.

The low Young's modulus and unique modular structural sequence of 2D perovskites add additional structural flexibility and enable their use as an active layer in high-performance PSCs.[247] To date, however, the efficiency of 2D-based PSCs is still unsatisfactory due to the suppressed out-of-plane charge transport by the organic cations in 2D perovskites. The properties of the 2D perovskites still depend highly on the inorganic counterpart with only a few exceptions. Functionalization or modification on the organic portion, such as using small organics with strong charge transfer properties to improve the conductivity of 2D perovskite, will open up an avenue for property discovery and development.[247, 248]

5. Stability of Two-Dimensional Material-Based Perovskite Solar Cells

In addition to high efficiency, long-term device stability remains a lingering and essential challenge to overcome in solar cells in order to realize future commercial development. Several reaction pathways involving water, oxygen, light, acid and heat lead to the

degradation of several device materials. Among them, H_2O and O_2 are two significant factors impacting the stability of devices.[29, 61, 116, 126, 234, 249] Perovskites tend to hydrolyze under high humidity because of their high sensitivity to water, leading to the degradation of the active layers in PSCs. The conversion of the perovskite $MAPbI_3$ follows the following equations:[250]

$$CH_3NH_3PbI_3 \leftrightarrow PbI_2 + CH_3NH_3I \quad (1)$$
$$CH_3NH_3I \leftrightarrow CH_3NH_2 + HI \quad (2)$$
$$HI + O_2 \leftrightarrow I_2 + H_2O \quad (3)$$
$$2HI \leftrightarrow H_2 + I_2 \quad (4)$$

In addition, the diffusion of molecular oxygen can be activated by illumination in the presence of organic molecules, promoting the formation of peroxide or superoxide compounds that attack and degrade the active layers. The long-term stability of PSCs in the presence of moisture and oxygen can be improved by an interfacial buffer layer, as note in **Section 3.4**, which can avoid the direct contact between perovskite and moisture.[61, 126, 127] Two dimensional graphene-related materials are well known for being thermally, mechanically and chemically stable. They can be easily processed into uniform ultrathin optically transparent layers which can efficiently transport electronic charge carriers as well.[251] It was reported that an rGO buffer layer between a HTL CuSCN and a Au electrode enabled PSCs to retain > 95% of their initial efficiency after aging for 1000 h at 60^{o}C.[122] A 4-fluorophenyl-functionalized rGO (rGO-4FPH) interfacial layer between the perovskite and HTL was also found to enhance the stability of PSCs.[22] The improvement in stability results from the rGO layer diffusion barrier, which hinders the diffusion of oxygen molecules from the electrode to the active layers. It is known that PEDOT:PSS is typically used as the HTL in PSCs, which is acidic and hygroscopic in nature and thus facilitates the decomposition of active layers in

PSCs. Pristine graphene is hydrophobic, whereas the GO surface consists of hydrophilic regions with hydrophobic islands.[49, 184] Yeo et al. reported that a PEDOT:PSS-based PSC was completely deteriorated and the PCE decreased to 0% after 5 days of exposure to ambient conditions.[119] In comparison, rGO-based solar cell devices retained 62% of their initial PCE (9.95%) after 6 days, suggesting improved stability against oxygen and moisture than conventional PEDOT:PSS-based solar cell devices.[119]

2D perovskites have been recognized as improving the stability of PSCs. Despite this, the underlying mechanism remains unclear.[245] It is reported that the moisture stability of perovskite can be improved by partial substitution of the MA^+ cations with long-chain organic cations which can change the perovskite structure from 3D to 2D.[129, 130, 252, 253] The hydrophobicity of long organic cations prevents direct contact between water and perovskite layer. Tsai, Nie et al. used the Ruddlesden–Popper layered 2D perovskite, $(BA)_2(MA)_2Pb_3I_{10}$ (n=3) and $(BA)_2(MA)_3Pb_4I_{13}$ (n = 4), to produce PSCs with near-single-crystalline active layers (**Figure. 26a**).[129] Stability testing under constant light illumination (AM1.5G) or in a humidity chamber (with a relative humidity of 65%) showed that unprotected 2D perovskite-based devices retained over 60% of their initial efficiency after 2250 h of illumination. These devices also exhibited improved humidity resistance when compared to their 3D equivalents.[129] Similar results are also observed for the encapsulated devices with no degradation occurring in the layered 2D perovskite-based devices under extended illumination (**Figure 26b and 26d**) or humidity exposure (**Figure 26c and 26e**). The 2D perovskite-based devices exhibited enhanced stability in comparison to their 3D counterparts.[129] The slower degradation may be due to the hydrophobic properties of the long organic side groups in the

2D perovskite structure which can prevent direct moisture exposure. Despite their superior stability, the efficiency of 2D-based PSCs is unsatisfactory due to the suppressed out-of-plane charge transport by the organic cations in 2D perovskites.[254] Tsai, Nie et al. fabricated thin hot-cast films of near-single-crystalline quality to optimize the preferential out-of-plane alignment of the inorganic perovskite component which can facilitate efficient charge transport.[129] The crystal domains in the hot-cast films are oriented with their (101) planes parallel to the substrate surface with a 2D in-plane orientation randomness.[129]

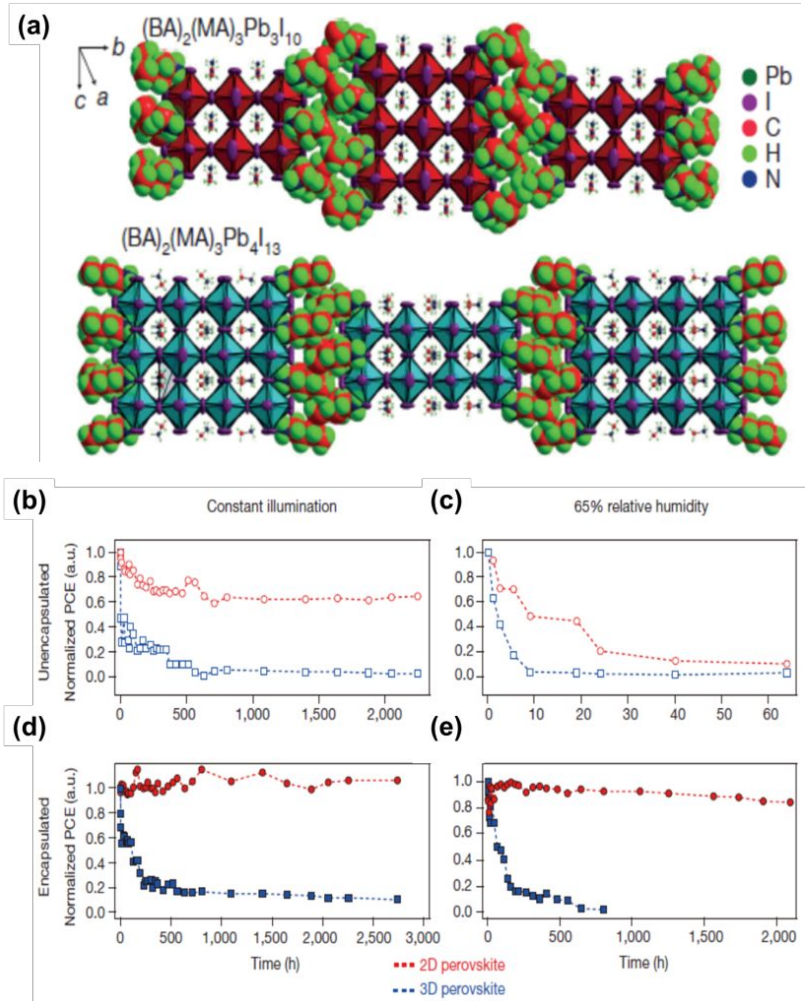

Figure 26. (a) The crystal structures of the $(BA)_2(MA)_2Pb_3I_{10}$ and $(BA)_2(MA)_3Pb_4I_{13}$ layered perovskites. (b) Photo-stability tests under constant AM1.5G illumination for 2D $(BA)_2(MA)_3Pb_4I_{13}$ (red) and 3D $MAPbI_3$ (blue) perovskite devices without (b) and with (d)

encapsulation. Humidity stability tests under 65% relative humidity for 2D $(BA)_2(MA)_3Pb_4I_{13}$ (red) and 3D $MAPbI_3$ (blue) perovskite devices without (c) and with (e) encapsulation. Reproduced from ref. [129] with permission from Springer Nature, copyright 2016.

6. Conclusions and Outlook

Two dimensional materials can serve as conductive electrodes, carrier transporting layers and buffer layers for applications in PSCs. The applications of graphene (and its derivatives), BP, transition metal dichalcogenides, and metal oxide nanosheets in PSCs have led to devices with superior photovoltaic performance. The electrical and optical properties of TDMs can be tuned by controlling the thickness and functionalization process. Furthermore, the Van der Waals interaction between neighboring atomic layers allows for more flexible integration of different materials to control the optical and electrical properties at the atomic scale as needed. The tunable energy-level capabilities of TDMs allow them to pair with a number of donor/acceptor systems in PSCs to form well-matched energy levels for effective carrier extraction, transport and collection. Other unique properties of TDMs including excellent mechanical flexibility and a large specific surface area facilitate charge transfer and light absorption which further improve the performance of TDM-incorporated PSCs. In addition, the incorporation of TDMs in PSCs can improve the morphology of other layers such as the HTL and perovskite layer, thereby increasing carrier generation in perovskite and facilitating carrier extraction at interfaces. 2D active perovskite absorbers in PSCs can be considered a feasible alternative to 3D perovskites. The long alkyl chains contained in the organic cations

of 2D perovskites confer hydrophobicity to the perovskite structure which provides a greater resistance to humidity when compared to 3D perovskites. The optical and electrical properties of 2D perovskites can be tuned by using different organic cations. Thus, the 2D perovskite structure can be electronically designed to fit the selective contacts of various established and emerging PSC architectures.

Although significant progress has been made in TDM-incorporated and 2D perovskite-based PSCs, several challenges remain to be addressed. First, since the surfaces of TDMs are mostly hydrophobic, it is difficult to dissolve them directly in water without additional surface treatments. Finding appropriate solvents to dissolve these TDMs for use in PSCs is a significant problem. A facile method to improve water solubility is through covalent functionalization. Covalent attachment of functional groups is generally achieved by reaction with unsaturated atoms at the edges or defect sites which change their properties and lead to improved solubility of TDMs in common solvents. For example, GO can be tethered to -CH_2OH terminated regioregular P3HT via esterification reaction to exhibit superior solubility due to the presence of an abundant number of hydroxyl groups in the added polymer.[255] For example, conjugated polymer functionalized BP derivatives such as (poly[(1,4-dieth-ynylbenzene)-alt-,9-bis(4-diphenylaminophenyl)fluorene]-(PDDF)-covalentl y grafted BP) showed very good solubility in organic solvents. Second, although CVD methods are commonly used to produce TDM thin films, the as-synthesized single-layer films inevitably have high sheet resistance (i.e. ~1050 ± 150 Ω sq^{-1} for graphene). The prevalent defects such as vacancies, impurities, nanoplatelet edges, and topological defects as well as the defect density in the TDM lattice can increase electron scattering resulting in an increase

in sheet resistance. Finding an efficient way to reduce the sheet resistance of TDMs is of great impantance to enhancing the performance of TDM-based PSCs. One strategy is to stack TDMs to form a multilayer structure which can introduce more channels for charge transport. Preparation techniques need to be optimized in terms of solvent, temperature, time and precursor selection to improve the quality of the TDM lattice and thereby enhance its conductivity. Another strategy is to increase the density of states by shifting the Fermi level of TDMs to raise the conductivity. Surface treatments such as doping and functionalization can improve the sheet resistance of TDMs by moving the Fermi level of TDMs to a region where the resistance is considerably lower due to an increase in the density of states. For example, graphene sheets with electron donating groups, such as -COOR (ester), have relatively lower sheet resistances than those of pristine graphene sheets.[256] Benzyl viologen-doped MoS_2 showed higher electron sheet density and lower resistance than pristine MoS_2.[257] A graphene-conducting-carbon-nanotube hybrid material circumvents electron scattering due to defects in graphene and reduces the sheet resistance by a factor of two relative to the neat graphene. In addition, the resistance can be further reduced by doping the hybrid with nitric acid. Third, the physical processes involved in the incorporation of TDMs into PSCs, such as interface transport, need to be better understood in order to achieve more efficient solar cells. Factors such as crystallization, position and orientation of TDMs also have a significant impact on the performance of PSCs with each requiring further investigation and optimization to improve device efficiency. Another figure of merit for high performance PSCs is the thickness of the layers. Engineering PSCs for achieving the desired performance with various mono- or few-layered TDMs by assembling them into stacks is challenging. The development

of synthesis strategies for TDMs of different layer architectures is essential to produce high-performance devices requiring different performance characteristic for different applications. Fourth, some TDMs, such as graphdiyne and BP, have been shown to enhance the performance of PSCs. However, reports on these TDM-based PSCs are still scarce, and more research should be devoted to these novel TDM materials to further boost their performance in PSCs. For 2D perovskite-based PSCs, the performance is still not comparable to that of 3D perovskite-based devices due to transport problems and the large exciton binding energy. Carrier transport through 2D perovskite films is inhibited due to the presence of long organic cations which act as insulating layers between the conducting inorganic slabs. One way to improve the performance of 2D perovskite-based PSCs is by controlling the preferential out-of-plane alignment of the crystallographic planes of the inorganic perovskite components to enhance charge carrier transport through selective contacts. Another approach is to design 2D perovskite-based PSCs in the form of a bulk heterojunction (i.e. an interpenetrating network at layer junctions) where the diffusion length of the exciton can be decreased to facilitate charge carrier separation.

The development of 2D materials will provide a new promising resource for incorporation into high-performance PSCs. Once the feasibility and benefits of TDMs are maximized to improve device efficiency, the promise of low-cost solar cells will be that much closer to being realized and commercialized.

Acknowledgements

This work was financially supported by the AFOSR (FA9550-19-1-0317), NSF (CMMI 1914713, ECCS 1914562, and CBET 1803495), National Natural Science Foundation of China (21603098, 61728403, 21471116 and 51772219), Natural Science Foundation of Jiangsu Province (BK20150580), and Zhejiang Provincial Natural Science Foundation of China (LZ18E030001 and LY17E020002). B.W. gratefully acknowledges financial support from the China Scholarship Council.

References

1. M. Acik and S. B. Darling, *J Mater Chem A*, 2016, **4**, 6185-6235.
2. V. M. Goldschmidt, *Naturwissenschaften*, 1926, **14**, 477-485.
3. Y. Tsujimoto, K. Yamaura and E. Takayama-Muromachi, *Appl Sci-Basel*, 2012, **2**, 206-219.
4. C. J. Bartel, C. Sutton, B. R. Goldsmith, R. Ouyang, C. B. Musgrave, L. M. Ghiringhelli and M. Scheffler, *Sci Adv*, 2018, **5**, eaav0693.
5. D. Lee and H. N. Lee, *Materials*, 2017, **10**, 368.
6. P. Gao, A. R. Bin Mohd Yusoff and M. K. Nazeeruddin, *Nat Commun*, 2018, **9**, 5028.
7. L. L. Mao, H. Tsai, W. Y. Nie, L. Ma, J. Im, C. C. Stoumpos, C. D. Malliakas, F. Hao, M. R. Wasielewski, A. D. Mohite and M. G. Kanatzidis, *Chem Mater*, 2016, **28**, 7781-7792.
8. H. L. Wang, W. Z. Lv, X. X. Tang, L. F. Chen, R. F. Chen and W. Huang, *Prog Chem*, 2017, **29**, 859-869.
9. H. Lai, B. Kan, T. Liu, N. Zheng, Z. Xie, T. Zhou, X. Wan, X. Zhang, Y. Liu and Y.

Chen, *J Am Chem Soc*, 2018, **140**, 11639-11646.

10. G. C. Xing, B. Wu, X. Y. Wu, M. J. Li, B. Du, Q. Wei, J. Guo, E. K. L. Yeow, T. C. Sum and W. Huang, *Nat Commun*, 2017, **8**, 14558.

11. P. F. Cheng, T. Wu, J. W. Zhang, Y. J. Li, J. X. Liu, L. Jiang, X. Mao, R. F. Lu, W. Q. Deng and K. L. Han, *J Phys Chem Lett*, 2017, **8**, 4402-4406.

12. A. Kojima, K. Teshima, Y. Shirai and T. Miyasaka, *J Am Chem Soc*, 2009, **131**, 6050-6051.

13. H. S. Kim, C. R. Lee, J. H. Im, K. B. Lee, T. Moehl, A. Marchioro, S. J. Moon, R. Humphry-Baker, J. H. Yum, J. E. Moser, M. Gratzel and N. G. Park, *Sci Rep-Uk*, 2012, **2**, 591.

14. F. Hao, C. C. Stoumpos, D. H. Cao, R. P. H. Chang and M. G. Kanatzidis, *Nat Photonics*, 2014, **8**, 489-494.

15. A. J. Huckaba, S. Gharibzadeh, M. Ralaiarisoa, C. Roldan-Carmona, N. Mohammadian, G. Grancini, Y. H. Lee, P. Amsalem, E. J. Plichta, N. Koch, A. Moshaii and M. K. Nazeeruddin, *Small Methods*, 2017, **1**, 1700250.

16. T. Gatti, S. Casaluci, M. Prato, M. Salerno, F. Di Stasio, A. Ansaldo, E. Menna, A. Di Carlo and F. Bonaccorso, *Adv Funct Mater*, 2016, **26**, 7443-7453.

17. J. S. Yeo, C. H. Lee, D. Jang, S. Lee, S. M. Jo, H. I. Joh and D. Y. Kim, *Nano Energy*, 2016, **30**, 667-676.

18. X. Sun, T. Lin, Q. G. Song, Y. Fu, Y. Wang, F. M. Jin, H. F. Zhao, W. L. Li, Z. S. Su and B. Chu, *Rsc Adv*, 2017, **7**, 45320-45326.

19. Y. X. Zhao, A. M. Nardes and K. Zhu, *J Phys Chem Lett*, 2014, **5**, 490-494.

20. A. Agresti, S. Pescetelli, A. L. Palma, A. E. D. Castillo, D. Konios, G. Kakavelakis, S. Razza, L. Cina, E. Kymakis, F. Bonaccorso and A. Di Carlo, *Acs Energy Lett*, 2017, **2**, 279-287.

21. W. Z. Li, H. P. Dong, X. D. Guo, N. Li, J. W. Li, G. D. Niu and L. D. Wang, *J Mater Chem A*, 2014, **2**, 20105-20111.

22. H. Li, L. M. Tao, F. H. Huang, Q. Sun, X. J. Zhao, J. B. Han, Y. Shen and M. K. Wang, *Acs Appl Mater Inter*, 2017, **9**, 38967-38976.

23. C. Y. Kuang, G. Tang, T. G. Jiu, H. Yang, H. B. Liu, B. R. Li, W. N. Luo, X. D. Li, W. J. Zhang, F. S. Lu, J. F. Fang and Y. L. Li, *Nano Lett*, 2015, **15**, 2756-2762.

24. Q. D. Yang, J. Li, Y. H. Cheng, H. W. Li, Z. Q. Guan, B. B. Yu and S. W. Tsang, *J Mater Chem A*, 2017, **5**, 9852-9858.

25. S. K. Muduli, E. Varrla, S. A. Kulkarni, G. F. Han, K. Thirumal, O. Lev, S. Mhaisalkar and N. Mathews, *J Power Sources*, 2017, **371**, 156-161.

26. F. Giustino and H. J. Snaith, *Acs Energy Lett*, 2016, **1**, 1233-1240.

27. National Renewable Energy Laboratory, Best Research-Cell Efficiencies, 2019.

28. F. Lang, M. A. Gluba, S. Albrecht, J. Rappich, L. Korte, B. Rech and N. H. Nickel, *J Phys Chem Lett*, 2015, **6**, 2745-2750.

29. J. H. Yu, C. H. Lee, H. I. Joh, J. S. Yeo and S. I. Na, *Nanoscale*, 2017, **9**, 17167-17173.

30. Y. C. Hsiao, T. Wu, M. X. Li, Q. Liu, W. Qin and B. Hu, *J Mater Chem A*, 2015, **3**, 15372-15385.

31. J. M. Frost, K. T. Butler, F. Brivio, C. H. Hendon, M. van Schilfgaarde and A. Walsh,

Nano Lett, 2014, **14**, 2584-2590.

32. Y. S. Liu, Z. R. Hong, Q. Chen, W. H. Chang, H. P. Zhou, T. B. Song, E. Young, Y. Yang, J. B. You, G. Li and Y. Yang, *Nano Lett*, 2015, **15**, 662-668.

33. M. H. Li, P. S. Shen, K. C. Wang, T. F. Guo and P. Chen, *J Mater Chem A*, 2015, **3**, 9011-9019.

34. T. Salim, S. Y. Sun, Y. Abe, A. Krishna, A. C. Grimsdale and Y. M. Lam, *J Mater Chem A*, 2015, **3**, 8943-8969.

35. Z. K. Liu, S. P. Lau and F. Yan, *Chem Soc Rev*, 2015, **44**, 5638-5679.

36. K. S. Novoselov, V. I. Fal'ko, L. Colombo, P. R. Gellert, M. G. Schwab and K. Kim, *Nature*, 2012, **490**, 192-200.

37. A. J. Mannix, X. F. Zhou, B. Kiraly, J. D. Wood, D. Alducin, B. D. Myers, X. L. Liu, B. L. Fisher, U. Santiago, J. R. Guest, M. J. Yacaman, A. Ponce, A. R. Oganov, M. C. Hersam and N. P. Guisinger, *Science*, 2015, **350**, 1513-1516.

38. M. E. Davila, L. Xian, S. Cahangirov, A. Rubio and G. Le Lay, *New J Phys*, 2014, **16**, 095002.

39. D. Golberg, Y. Bando, Y. Huang, T. Terao, M. Mitome, C. C. Tang and C. Y. Zhi, *Acs Nano*, 2010, **4**, 2979-2993.

40. H. Liu, Y. C. Du, Y. X. Deng and P. D. Ye, *Chem Soc Rev*, 2015, **44**, 2732-2743.

41. Q. H. Wang, K. Kalantar-Zadeh, A. Kis, J. N. Coleman and M. S. Strano, *Nat Nanotechnol*, 2012, **7**, 699-712.

42. S. Z. Butler, S. M. Hollen, L. Y. Cao, Y. Cui, J. A. Gupta, H. R. Gutierrez, T. F. Heinz, S. S. Hong, J. X. Huang, A. F. Ismach, E. Johnston-Halperin, M. Kuno, V. V.

Plashnitsa, R. D. Robinson, R. S. Ruoff, S. Salahuddin, J. Shan, L. Shi, M. G. Spencer, M. Terrones, W. Windl and J. E. Goldberger, *Acs Nano*, 2013, **7**, 2898-2926.

43. Q. Liu, M. C. Qin, W. J. Ke, X. L. Zheng, Z. Chen, P. L. Qin, L. B. Xiong, H. W. Lei, J. W. Wan, J. Wen, G. Yang, J. J. Ma, Z. Y. Zhang and G. J. Fang, *Adv Funct Mater*, 2016, **26**, 6069-6075.

44. W. Q. Wu, D. H. Chen, Y. B. Cheng and R. A. Caruso, *Sol Rrl*, 2017, **1**, 1700117.

45. Y. G. Rong, Z. L. Ku, A. Y. Mei, T. F. Liu, M. Xu, S. G. Ko, X. Li and H. W. Han, *J Phys Chem Lett*, 2014, **5**, 2160-2164.

46. C. Li, Y. H. Li, Y. J. Xing, Z. L. Zhang, X. F. Zhang, Z. Li, Y. T. Shi, T. L. Ma, R. Z. Ma, K. L. Wang and J. Q. Wei, *Acs Appl Mater Inter*, 2015, **7**, 15117-15122.

47. K. Mahmood, B. S. Swain, A. R. Kirmani and A. Amassian, *J Mater Chem A*, 2015, **3**, 9051-9057.

48. J. F. Tang, Z. L. Tseng, L. C. Chen and S. Y. Chu, *Sol Energ Mat Sol C*, 2016, **154**, 18-22.

49. E. Singh and H. S. Nalwa, *Rsc Adv*, 2015, **5**, 73575-73600.

50. T. Mueller, F. N. A. Xia and P. Avouris, *Nat Photonics*, 2010, **4**, 297-301.

51. O. Lopez-Sanchez, D. Lembke, M. Kayci, A. Radenovic and A. Kis, *Nat Nanotechnol*, 2013, **8**, 497-501.

52. F. Bonaccorso, Z. Sun, T. Hasan and A. C. Ferrari, *Nat Photonics*, 2010, **4**, 611-622.

53. M. Z. Cai, D. Thorpe, D. H. Adamson and H. C. Schniepp, *J Mater Chem*, 2012, **22**, 24992-25002.

54. G. L. Li, G. Liu, M. Li, D. Wan, K. G. Neoh and E. T. Kang, *J Phys Chem C*, 2010,

114, 12742-12748.

55. C. M. Hill, Y. Zhu and S. Pan, *Acs Nano*, 2011, **5**, 942-951.

56. J. Kim, S. Kwon, D. H. Cho, B. Kang, H. Kwon, Y. Kim, S. O. Park, G. Y. Jung, E. Shin, W. G. Kim, H. Lee, G. H. Ryu, M. Choi, T. H. Kim, J. Oh, S. Park, S. K. Kwak, S. W. Yoon, D. Byun, Z. Lee and C. Lee, *Nat Commun*, 2015, **6**, 8294.

57. P. You, Z. K. Liu, Q. D. Tai, S. H. Liu and F. Yan, *Adv Mater*, 2015, **27**, 3632-3638.

58. Z. K. Liu, P. You, C. Xie, G. Q. Tang and F. Yan, *Nano Energy*, 2016, **28**, 151-157.

59. J. Y. Liu, Y. Z. Xue, Z. Y. Wang, Z. Q. Xu, C. X. Zheng, B. Weber, J. C. Song, Y. S. Wang, Y. R. Lu, Y. P. Zhang and Q. L. Bao, *Acs Nano*, 2016, **10**, 3536-3542.

60. Y. H. Lee, X. Q. Zhang, W. J. Zhang, M. T. Chang, C. T. Lin, K. D. Chang, Y. C. Yu, J. T. W. Wang, C. S. Chang, L. J. Li and T. W. Lin, *Adv Mater*, 2012, **24**, 2320-2325.

61. X. H. Hu, H. Jiang, J. Li, J. X. Ma, D. Yang, Z. K. Liu, F. Gao and S. Z. Liu, *Nanoscale*, 2017, **9**, 8274-8280.

62. A. Kumar and C. H. Lee, *Advances in Graphene Science*, 2013, DOI: 10.5772/55728, 55-75.

63. D. Akinwande, *Proc Spie*, 2014, **9083**, 90831N-90831.

64. S. Y. Lee and S. J. Park, *Carbon Lett*, 2012, **13**, 73-87.

65. S. Pari, A. Cuellar and B. M. Wong, *J Phys Chem C*, 2016, **120**, 18871-18877.

66. R. Roldan, A. Castellanos-Gomez, E. Cappelluti and F. Guinea, *J Phys-Condens Mat*, 2015, **27**, 313201.

67. J. S. Qiao, X. H. Kong, Z. X. Hu, F. Yang and W. Ji, *Nat Commun*, 2014, **5**, 4475.

68. J. W. Gong, H. Qiao, S. Sigdel, H. Elbohy, N. Adhikari, Z. P. Zhou, K. Sumathy, Q.

F. Wei and Q. Q. Qiao, *Aip Adv*, 2015, **5**, 067134

69. J. H. Park, G. S. Kang, S. I. Kwon, D. G. Lim, Y. J. Choi, K. J. Choi and J. G. Park, *J Nanosci Nanotechno*, 2008, **8**, 4658-4661.

70. X. Li and H. W. Zhu, *J Materiomics*, 2015, **1**, 33-44.

71. A. Capasso, A. E. D. Castillo, L. Najafi, V. Pellegrini, F. Bonaccorso, F. Matteocci, L. Cina and A. Di Carlo, *2015 Ieee 15th International Conference on Nanotechnology (Ieee-Nano)*, 2015, 1138-1141.

72. E. Nouri, M. R. Mohammadi and P. Lianos, *Chem Commun*, 2017, **53**, 1630-1633.

73. G. Yoon, D. H. Seo, K. Ku, J. Kim, S. Jeon and K. Kang, *Chem Mater*, 2015, **27**, 2067-2073.

74. M. P. Lavin-Lopez, J. L. Valverde, L. Sanchez-Silva and A. Romero, *Ind Eng Chem Res*, 2016, **55**, 845-855.

75. B. C. Brodie, *Ann. Chim. Phys*, 1860, **59**, 466-472.

76. S. Gambhir, R. Jalili, D. L. Officer and G. G. Wallace, *Npg Asia Mater*, 2015, **7**, e186.

77. P. S. Chandrasekhar and V. K. Komarala, *Rsc Adv*, 2017, **7**, 28610-28615.

78. D. B. Mitzi, S. Wang, C. A. Feild, C. A. Chess and A. M. Guloy, *Science*, 1995, **267**, 1473-1476.

79. M. C. Weidman, M. Seitz, S. D. Stranks and W. A. Tisdale, *Acs Nano*, 2016, **10**, 7830-7839.

80. C. C. Stoumpos, D. H. Cao, D. J. Clark, J. Young, J. M. Rondinelli, J. I. Jang, J. T. Hupp and M. G. Kanatzidis, *Chem Mater*, 2016, **28**, 2852-2867.

81. F. O. Saouma, C. C. Stoumpos, J. Wong, M. G. Kanatzidis and J. I. Jang, *Nat*

Commun, 2017, **8**, 742.

82. K. Kikuchi, Y. Takeoka, M. Rikukawa and K. Sanui, *Curr Appl Phys*, 2004, **4**, 599-602.

83. J. J. Peng, Y. N. Chen, K. B. Zheng, T. Pullerits and Z. Q. Liang, *Chem Soc Rev*, 2017, **46**, 5714-5729.

84. C. X. Huo, B. Cai, Z. Yuan, B. W. Ma and H. B. Zeng, *Small Methods*, 2017, **1**, 1600018.

85. P. Tyagi, S. M. Arveson and W. A. Tisdale, *J Phys Chem Lett*, 2015, **6**, 1911-1916.

86. K. Yao, X. F. Wang, Y. X. Xu, F. Li and L. Zhou, *Chem Mater*, 2016, **28**, 3131-3138.

87. K. Meng, S. S. Gao, L. L. Wu, G. Wang, X. Liu, G. Chen, Z. Liu and G. Chen, *Nano Lett*, 2016, **16**, 4166-4173.

88. J. Z. Song, L. M. Xu, J. H. Li, J. Xue, Y. H. Dong, X. M. Li and H. B. Zeng, *Adv Mater*, 2016, **28**, 4861-4869.

89. J. Shamsi, Z. Y. Dang, P. Bianchini, C. Canale, F. Di Stasio, R. Brescia, M. Prato and L. Manna, *J Am Chem Soc*, 2016, **138**, 7240-7243.

90. S. K. Balakrishnan and P. V. Kamat, *Chem Mater*, 2018, **30**, 74-78.

91. S. K. Pathak, A. Abate, T. Leijtens, D. J. Hollman, J. Teuscher, L. Pazos, P. Docampo, U. Steiner and H. J. Snaith, *Adv Energy Mater*, 2014, **4**, 1301667.

92. A. Ng, Z. W. Ren, Q. Shen, S. H. Cheung, H. C. Gokkaya, S. K. So, A. B. Djurisic, Y. Y. Wan, X. J. Wu and C. Surya, *Acs Appl Mater Inter*, 2016, **8**, 32805-32814.

93. Y. P. Wang, Y. F. Shi, G. Q. Xin, J. Lan and J. Shi, *Cryst Growth Des*, 2015, **15**, 4741-4749.

94. Q. Zhang, R. Su, X. F. Liu, J. Xing, T. C. Sum and Q. H. Xiong, *Adv Funct Mater*, 2016, **26**, 6238-6245.

95. S. T. Ha, X. F. Liu, Q. Zhang, D. Giovanni, T. C. Sum and Q. H. Xiong, *Adv Opt Mater*, 2014, **2**, 838-844.

96. S. T. Ha, R. Su, J. Xing, Q. Zhang and Q. H. Xiong, *Chem Sci*, 2017, **8**, 2522-2536.

97. M. Z. Liu, M. B. Johnston and H. J. Snaith, *Nature*, 2013, **501**, 395-398.

98. I. Jeon, J. Yoon, N. Ahn, M. Atwa, C. Delacou, A. Anisimov, E. I. Kauppinen, M. Choi, S. Maruyama and Y. Matsuo, *J Phys Chem Lett*, 2017, **8**, 5395-5401.

99. J. Yoon, H. Sung, G. Lee, W. Cho, N. Ahn, H. S. Jung and M. Choi, *Energ Environ Sci*, 2017, **10**, 337-345.

100. M. Duan, Y. G. Rong, A. Y. Mei, Y. Hu, Y. S. Sheng, Y. J. Guan and H. W. Han, *Carbon*, 2017, **120**, 71-76.

101. J. H. Heo, D. H. Shin, S. Kim, M. H. Jang, M. H. Lee, S. W. Seo, S. H. Choi and S. H. Im, *Chem Eng J*, 2017, **323**, 153-159.

102. F. Shao, Z. L. Tian, P. Qin, K. J. Bu, W. Zhao, L. Xu, D. L. Wang and F. Q. Huang, *Sci Rep-Uk*, 2018, **8**, 7033.

103. J. T. W. Wang, J. M. Ball, E. M. Barea, A. Abate, J. A. Alexander-Webber, J. Huang, M. Saliba, I. Mora-Sero, J. Bisquert, H. J. Snaith and R. J. Nicholas, *Nano Lett*, 2014, **14**, 724-730.

104. C. Wang, Y. Tang, Y. J. Hu, L. Huang, J. X. Fu, J. Jin, W. M. Shi, L. J. Wang and W. G. Yang, *Rsc Adv*, 2015, **5**, 52041-52047.

105. S. W. Tong, J. Balapanuru, D. Y. Fu and K. P. Loh, *Acs Appl Mater Inter*, 2016, **8**,

29496-29503.

106. G. S. Han, Y. H. Song, Y. U. Jin, J. W. Lee, N. G. Park, B. K. Kang, J. K. Lee, I. S. Cho, D. H. Yoon and H. S. Jung, *Acs Appl Mater Inter*, 2015, **7**, 23521-23526.

107. T. Umeyama, D. Matano, J. Baek, S. Gupta, S. Ito, V. Subramanian and H. Imahori, *Chem Lett*, 2015, **44**, 1410-1412.

108. K. T. Cho, G. Grancini, Y. Lee, D. Konios, S. Paek, E. Kymakis and M. K. Nazeeruddin, *Chemsuschem*, 2016, **9**, 3040-3044.

109. F. Biccari, F. Gabelloni, E. Burzi, M. Gurioli, S. Pescetelli, A. Agresti, A. E. D. Castillo, A. Ansaldo, E. Kymakis, F. Bonaccorso, A. Di Carlo and A. Vinattieri, *Adv Energy Mater*, 2017, **7**, 1701349.

110. S. S. Mali, C. S. Shim, H. Kim and C. K. Hong, *J Mater Chem A*, 2016, **4**, 12158-12169.

111. X. J. Zhao, L. M. Tao, H. Li, W. C. Huang, P. Y. Sun, J. Liu, S. S. Liu, Q. Sun, Z. F. Cui, L. J. Sun, Y. Shen, Y. Yang and M. K. Wang, *Nano Lett*, 2018, **18**, 2442-2449.

112. M. Li, Z. K. Wang, T. Kang, Y. G. Yang, X. Y. Gao, C. S. Hsu, Y. L. Li and L. S. Liao, *Nano Energy*, 2018, **43**, 47-54.

113. J. S. Li, T. G. Jiu, C. H. Duan, Y. Wang, H. N. Zhang, H. M. Jian, Y. J. Zhao, N. Wang, C. S. Huang and Y. L. Li, *Nano Energy*, 2018, **46**, 331-337.

114. P. Huang, L. G. Yuan, K. C. Zhang, Q. Y. Chen, Y. Zhou, B. Song and Y. F. Li, *Acs Appl Mater Inter*, 2018, **10**, 14796-14802.

115. G. Yang, H. W. Lei, H. Tao, X. L. Zheng, J. J. Ma, Q. Liu, W. J. Ke, Z. L. Chen, L. B. Xiong, P. L. Qin, Z. Chen, M. C. Qin, X. H. Lu, Y. F. Yan and G. J. Fang, *Small*,

2017, **13**, 1601769.

116. J. C. Yu, J. A. Hong, E. D. Jung, D. Bin Kim, S. M. Baek, S. Lee, S. Cho, S. S. Park, K. J. Choi and M. H. Song, *Sci Rep-Uk*, 2018, **8**, 1070.

117. D. Y. Lee, S. I. Na and S. S. Kim, *Nanoscale*, 2016, **8**, 1513-1522.

118. D. Li, J. Cui, H. Li, D. K. Huang, M. K. Wang and Y. Shen, *Sol Energy*, 2016, **131**, 176-182.

119. J. S. Yeo, R. Kang, S. Lee, Y. J. Jeon, N. Myoung, C. L. Lee, D. Y. Kim, J. M. Yun, Y. H. Seo, S. S. Kim and S. I. Na, *Nano Energy*, 2015, **12**, 96-104.

120. X. Huang, H. Guo, J. Yang, K. Wang, X. B. Niu and X. B. Liu, *Org Electron*, 2016, **39**, 288-295.

121. J. Y. Xiao, J. J. Shi, H. B. Liu, Y. Z. Xu, S. T. Lv, Y. H. Luo, D. M. Li, Q. B. Meng and Y. L. Li, *Adv Energy Mater*, 2015, **5**, 1401943.

122. J. Z. Li, M.; Zhao, C.; Jian, H.; Wang N.; Yao, L.; Huang, C.; Zhao, Y.; Jiu, T.,, *ACS Appl Mater Interfaces*, 2018, **11**, 2626-26311.

123. G. Kakavelakis, I. Paradisanos, B. Paci, A. Generosi, M. Papachatzakis, T. Maksudov, L. Najafi, A. E. D. Castillo, G. Kioseoglou, E. Stratakis, F. Bonaccorso and E. Kymakis, *Adv Energy Mater*, 2018, **8**, 1702287.

124. Y. G. Kim, K. C. Kwon, Q. Van Le, K. Hong, H. W. Jang and S. Y. Kim, *J Power Sources*, 2016, **319**, 1-8.

125. P. Huang, Z. W. Wang, Y. F. Liu, K. C. Zhang, L. G. Yuan, Y. Zhou, B. Song and Y. F. Li, *Acs Appl Mater Inter*, 2017, **9**, 25323-25331.

126. A. Capasso, F. Matteocci, L. Najafi, M. Prato, J. Buha, L. Cina, V. Pellegrini, A. Di

Carlo and F. Bonaccorso, *Adv Energy Mater*, 2016, **6**, 1600920.

127. N. Arora, M. I. Dar, A. Hinderhofer, N. Pellet, F. Schreiber, S. M. Zakeeruddin and M. Gratzel, *Science*, 2017, **358**, 768-771.

128. X. N. Zhang, G. W. Ji, D. B. Xiong, Z. H. Su, B. Zhao, K. C. Shen, Y. G. Yang and X. Y. Gao, *Rsc Adv*, 2018, **8**, 987-993.

129. H. H. Tsai, W. Y. Nie, J. C. Blancon, C. C. S. Toumpos, R. Asadpour, B. Harutyunyan, A. J. Neukirch, R. Verduzco, J. J. Crochet, S. Tretiak, L. Pedesseau, J. Even, M. A. Alam, G. Gupta, J. Lou, P. M. Ajayan, M. J. Bedzyk, M. G. Kanatzidis and A. D. Mohite, *Nature*, 2016, **536**, 312-316.

130. I. C. Smith, E. T. Hoke, D. Solis-Ibarra, M. D. McGehee and H. I. Karunadasa, *Angew Chem Int Edit*, 2014, **53**, 11232-11235.

131. Q. B. Cai, H. T. Li, Y. X. Jiang, L. M. Tu, L. Ma, X. J. Wu, S. E. Yang, Z. F. Shi, J. H. Zang and Y. S. Chen, *Sol Energy*, 2018, **159**, 786-793.

132. Y. Q. Liao, H. F. Liu, W. J. Zhou, D. W. Yang, Y. Q. Shang, Z. F. Shi, B. H. Li, X. Y. Jiang, L. J. Zhang, L. N. Quan, R. Quintero-Bermudez, B. R. Sutherland, Q. X. Mi, E. H. Sargent and Z. L. Ning, *J Am Chem Soc*, 2017, **139**, 6693-6699.

133. G. Grancini, C. Roldan-Carmona, I. Zimmermann, E. Mosconi, X. Lee, D. Martineau, S. Narbey, F. Oswald, F. De Angelis, M. Graetzel and M. K. Nazeeruddin, *Nat Commun*, 2017, **8**, 15684.

134. A. Abate, J. P. Correa-Baena, M. Saliba, M. S. Su'ait and F. Bella, *Chem-Eur J*, 2018, **24**, 3083-3100.

135. H. Sung, N. Ahn, M. S. Jang, J. K. Lee, H. Yoon, N. G. Park and M. Choi, *Adv*

Energy Mater, 2016, **6**, 1501873.

136. C. Lee, X. D. Wei, J. W. Kysar and J. Hone, *Science*, 2008, **321**, 385-388.

137. Z. Chen, B. Cotterell and W. Wang, *Eng Fract Mech*, 2002, **69**, 597-603.

138. N. Liu, A. Chortos, T. Lei, L. H. Jin, T. R. Kim, W. G. Bae, C. X. Zhu, S. H. Wang, R. Pfattner, X. Y. Chen, R. Sinclair and Z. A. Bao, *Sci Adv*, 2017, **3**, e1700159.

139. D. H. Shin, S. Kim, J. M. Kim, C. W. Jang, J. H. Kim, K. W. Lee, J. Kim, S. D. Oh, D. H. Lee, S. S. Kang, C. O. Kim, S. H. Choi and K. J. Kim, *Adv Mater*, 2015, **27**, 2614-2620.

140. J. M. Kim, S. Kim and S. H. Choi, *Acs Sustain Chem Eng*, 2019, **7**, 734-739.

141. S. J. Kwon, T. H. Han, Y. H. Kim, T. Ahmed, H. K. Seo, H. Kim, D. J. Kim, W. Xu, B. H. Hong, J. X. Zhu and T. W. Lee, *Acs Appl Mater Inter*, 2018, **10**, 4874-4881.

142. G. Yang, H. Tao, P. L. Qin, W. J. Ke and G. J. Fang, *J Mater Chem A*, 2016, **4**, 3970-3990.

143. K. C. Kwon, K. S. Choi and S. Y. Kim, *Adv Funct Mater*, 2012, **22**, 4724-4731.

144. J. M. Yun, Y. J. Noh, J. S. Yeo, Y. J. Go, S. I. Na, H. G. Jeong, J. Kim, S. Lee, S. S. Kim, H. Y. Koo, T. W. Kim and D. Y. Kim, *J Mater Chem C*, 2013, **1**, 3777-3783.

145. G. Jo, S. I. Na, S. H. Oh, S. Lee, T. S. Kim, G. Wang, M. Choe, W. Park, J. Yoon, D. Y. Kim, Y. H. Kahng and T. Lee, *Appl Phys Lett*, 2010, **97**, 213301.

146. K. S. Novoselov, A. K. Geim, S. V. Morozov, D. Jiang, Y. Zhang, S. V. Dubonos, I. V. Grigorieva and A. A. Firsov, *Science*, 2004, **306**, 666-669.

147. G. V. Dubacheva, C. K. Liang and D. M. Bassani, *Coordin Chem Rev*, 2012, **256**, 2628-2639.

148. J. Liu, M. Durstock and L. M. Dai, *Energ Environ Sci*, 2014, **7**, 1297-1306.

149. M. I. Ahmed, Z. Hussain, M. Mujahid, A. N. Khan, S. S. Javaid and A. Habib, *Aip Adv*, 2016, **6**, 065303.

150. P. Tiwana, P. Docampo, M. B. Johnston, H. J. Snaith and L. M. Herz, *Acs Nano*, 2011, **5**, 5158-5166.

151. H. J. Snaith and M. Gratzel, *Adv Mater*, 2006, **18**, 1910-1914.

152. P. Yang, Z. J. Hu, X. C. Zhao, D. Chen, H. Lin, X. C. Lai and L. J. Yang, *Chemistryselect*, 2017, **2**, 9433-9437.

153. M. F. M. Noh, C. H. Teh, R. Daik, E. L. Lim, C. C. Yap, M. A. Ibrahim, N. A. Ludin, A. B. Yusoff, J. Jang and M. A. M. Terid, *J Mater Chem C*, 2018, **6**, 682-712.

154. R. L. Z. Hoye, K. P. Musselman and J. L. MacManus-Driscoll, *Apl Mater*, 2013, **1**, 060701.

155. M. M. Tavakoli, R. Tavakoli, P. Yadav and J. Kong, *J Mater Chem A*, 2019, **7**, 679-686.

156. M. H. Zhu, W. W. Liu, W. J. Ke, L. S. Xie, P. Dong and F. Hao, *Acs Appl Mater Inter*, 2019, **11**, 666-673.

157. J. I. Fujisawa, T. Eda and M. Hanaya, *Chem Phys Lett*, 2017, **685**, 23-26.

158. J. H. Qiu, Y. C. Qiu, K. Y. Yan, M. Zhong, C. Mu, H. Yan and S. H. Yang, *Nanoscale*, 2013, **5**, 3245-3248.

159. S. Y. Shao, M. Abdu-Aguye, L. Qiu, L. H. Lai, J. Liu, S. Adjokatse, F. Jahani, M. E. Kamminga, G. H. ten Brink, T. T. M. Palstra, B. J. Kooi, J. C. Hummelen and M. A. Loi, *Energ Environ Sci*, 2016, **9**, 2444-2452.

160. G. Kakavelakis, T. Maksudov, D. Konios, I. Paradisanos, G. Kioseoglou, E. Stratakis and E. Kymakis, *Adv Energy Mater*, 2017, **7**, 1602120.

161. D. Yang, R. X. Yang, X. D. Ren, X. J. Zhu, Z. Yang, C. Li and S. Z. Liu, *Adv Mater*, 2016, **28**, 5206-5213.

162. M. J. Zhang, X. X. Wang, H. J. Sun, N. Wang, Q. Lv, W. W. Cui, Y. Z. Long and C. S. Huang, *Sci Rep-Uk*, 2017, **7**, 11535.

163. J. J. Zheng, X. Zhao, Y. L. Zhao and X. F. Gao, *Sci Rep-Uk*, 2013, **3**, 1271.

164. F. Chang, L. J. Huang, Y. R. Li, C. Z. Guo and Q. Z. Diao, *Int J Electrochem Sc*, 2017, **12**, 10348-10358.

165. A. Savva, I. Burgues-Ceballos and S. A. Choulis, *Adv Energy Mater*, 2016, **6**, 1600285.

166. M. D. Ye, C. F. He, J. Iocozzia, X. Q. Liu, X. Cui, X. T. Meng, M. Rager, X. D. Hong, X. Y. Liu and Z. Q. Lin, *J Phys D Appl Phys*, 2017, **50**, 373002.

167. L. Etgar, P. Gao, Z. S. Xue, Q. Peng, A. K. Chandiran, B. Liu, M. K. Nazeeruddin and M. Gratzel, *J Am Chem Soc*, 2012, **134**, 17396-17399.

168. Q. Chen, H. P. Zhou, T. B. Song, S. Luo, Z. R. Hong, H. S. Duan, L. T. Dou, Y. S. Liu and Y. Yang, *Nano Lett*, 2014, **14**, 4158-4163.

169. A. K. Jena, Y. Numata, M. Ikegami and T. Miyasaka, *J Mater Chem A*, 2018, **6**, 2219-2230.

170. J. B. You, L. Meng, T. B. Song, T. F. Guo, Y. Yang, W. H. Chang, Z. R. Hong, H. J. Chen, H. P. Zhou, Q. Chen, Y. S. Liu, N. De Marco and Y. Yang, *Nat Nanotechnol*, 2016, **11**, 75-81.

171. L. Calio, J. Follana-Berna, S. Kazim, M. Madsen, H. G. Rubahn, A. Sastre-Santos and S. Ahmad, *Sustain Energ Fuels*, 2017, **1**, 2071-2077.

172. G. A. Sepalage, S. Meyer, A. Pascoe, A. D. Scully, F. Z. Huang, U. Bach, Y. B. Cheng and L. Spiccia, *Adv Funct Mater*, 2015, **25**, 5650-5661.

173. S. S. Li, K. H. Tu, C. C. Lin, C. W. Chen and M. Chhowalla, *Acs Nano*, 2010, **4**, 3169-3174.

174. Z. W. Wu, S. Bai, J. Xiang, Z. C. Yuan, Y. G. Yang, W. Cui, X. Y. Gao, Z. Liu, Y. Z. Jin and B. Q. Sun, *Nanoscale*, 2014, **6**, 10505-10510.

175. Y. Gao, H. L. Yip, K. S. Chen, K. M. O'Malley, O. Acton, Y. Sun, G. Ting, H. Z. Chen and A. K. Y. Jen, *Adv Mater*, 2011, **23**, 1903-1908.

176. V. Strelko, D. J. Malik and M. Streat, *Carbon*, 2002, **40**, 95-104.

177. X. Z. Gong, G. Z. Liu, Y. S. Li, D. Y. W. Yu and W. Y. Teoh, *Chem Mater*, 2016, **28**, 8082-8118.

178. E. Jokar, Z. Y. Huang, S. Narra, C. Y. Wang, V. Kattoor, C. C. Chung and E. W. G. Diau, *Adv Energy Mater*, 2018, **8**, 1701640.

179. C. Bi, Q. Wang, Y. C. Shao, Y. B. Yuan, Z. G. Xiao and J. S. Huang, *Nat Commun*, 2015, **6**, 7747.

180. X. W. Yin, Y. Zhou, J. H. Han, H. Nan, M. Q. Tai, Y. C. Gu, J. B. Li and H. Lin, *J Mater Chem A*, 2018, **6**, 20702-20711.

181. Q. F. Dong, Y. B. Yuan, Y. C. Shao, Y. J. Fang, Q. Wang and J. S. Huang, *Energ Environ Sci*, 2015, **8**, 2464-2470.

182. A. L. Palma, L. Cina, S. Pescetelli, A. Agresti, M. Raggio, R. Paolesse, F. Bonaccorso

and A. Di Carlo, *Nano Energy*, 2016, **22**, 349-360.

183. W. Z. Li, H. P. Dong, L. D. Wang, N. Li, X. D. Guo, J. W. Li and Y. Qiu, *J Mater Chem A*, 2014, **2**, 13587-13592.

184. J. M. Yun, J. S. Yeo, J. Kim, H. G. Jeong, D. Y. Kim, Y. J. Noh, S. S. Kim, B. C. Ku and S. I. Na, *Adv Mater*, 2011, **23**, 4923-4928.

185. V. Singh, D. Joung, L. Zhai, S. Das, S. I. Khondaker and S. Seal, *Prog Mater Sci*, 2011, **56**, 1178-1271.

186. D. W. Johnson, B. P. Dobson and K. S. Coleman, *Curr Opin Colloid In*, 2015, **20**, 367-382.

187. H. Luo, X. H. Lin, X. Hou, L. K. Pan, S. M. Huang and X. H. Chen, *Nano-Micro Lett*, 2017, **9**, 39.

188. K. Ahmad and S. M. Mobin, *New J Chem*, 2017, **41**, 14253-14258.

189. S. Y. Wang, X. N. Huang, H. X. Sun and C. Y. Wu, *Nanoscale Res Lett*, 2017, **12**, 619.

190. A. Giuri, S. Masi, S. Colella, A. Listorti, A. Rizzo, A. Kovtun, S. Dell'Elce, A. Liscio and C. E. Corcione, *Polym Eng Sci*, 2017, **57**, 546-552.

191. J. Z. Niu, D. Yang, X. D. Ren, Z. Yang, Y. C. Liu, X. J. Zhu, W. G. Zhao and S. Z. Liu, *Org Electron*, 2017, **48**, 165-171.

192. D. A. Mengistie, M. A. Ibrahem, P. C. Wang and C. W. Chu, *Acs Appl Mater Inter*, 2014, **6**, 2292-2299.

193. Z. Y. Jiang, X. H. Chen, X. H. Lin, X. K. Jia, J. F. Wang, L. K. Pan, S. M. Huang, F. R. Zhu and Z. Sun, *Sol Energ Mat Sol C*, 2016, **146**, 35-43.

194. J. S. Yeo, J. M. Yun, D. Y. Kim, S. Park, S. S. Kim, M. H. Yoon, T. W. Kim and S. I. Na, *Acs Appl Mater Inter*, 2012, **4**, 2551-2560.

195. J. W. Liu, S. Pathak, T. Stergiopoulos, T. Leijtens, K. Wojciechowski, S. Schumann, N. Kausch-Busies and H. J. Snaith, *J Phys Chem Lett*, 2015, **6**, 1666-1673.

196. Y. Hou, H. Zhang, W. Chen, S. Chen, C. O. R. Quiroz, H. Azimi, A. Osvet, G. J. Matt, E. Zeira, J. Seuring, N. Kausch-Busies, W. Lovenich and C. J. Brabec, *Adv Energy Mater*, 2015, **5**, 1500543.

197. A. Giuri, S. A. Masi, S. Colella, A. Kovtun, S. Dell'Elce, E. Treossi, A. Liscio, C. E. Corcione, A. Rizzo and A. Listorti, *Adv Funct Mater*, 2016, **26**, 6985-6994.

198. Z. C. He, C. M. Zhong, X. Huang, W. Y. Wong, H. B. Wu, L. W. Chen, S. J. Su and Y. Cao, *Adv Mater*, 2011, **23**, 4636-4643.

199. T. H. Han, M. R. Choi, S. H. Woo, S. Y. Min, C. L. Lee and T. W. Lee, *Adv Mater*, 2012, **24**, 1487-1493.

200. K. G. Lim, S. Ahn, Y. H. Kim, Y. B. Qi and T. W. Lee, *Energ Environ Sci*, 2016, **9**, 932-939.

201. J. Ye, X. L. Li, J. J. Zhao, X. L. Mei and Q. Li, *Rsc Adv*, 2016, **6**, 36356-36361.

202. T. Gatti, F. Lamberti, P. Topolovsek, M. Abdu-Aguye, R. Sorrentino, L. Perino, M. Salerno, L. Girardi, C. Marega, G. A. Rizzi, M. A. Loi, A. Petrozza and E. Menna, *Sol Rrl*, 2018, **2**, 1800013.

203. G. J. Zhao, Y. J. He and Y. F. Li, *Adv Mater*, 2010, **22**, 4355-4358.

204. N. Boulanger, V. Yu, M. Hilke, M. F. Toney and D. R. Barbero, *Phys Chem Chem Phys*, 2017, **19**, 8496-8503.

205. T. Gatti, N. Vicentini, M. Mba and E. Menna, *Eur J Org Chem*, 2016, DOI: 10.1002/ejoc.201501411, 1071-1090.

206. T. Kuilla, S. Bhadra, D. H. Yao, N. H. Kim, S. Bose and J. H. Lee, *Prog Polym Sci*, 2010, **35**, 1350-1375.

207. J. S. Li, M. Zhao, C. J. Zhao, H. M. Jian, N. Wang, L. L. Yao, C. S. Huang, Y. J. Zhao and T. G. Jiu, *Acs Appl Mater Inter*, 2019, **11**, 2626-2631.

208. C. S. Huang, Y. J. Li, N. Wang, Y. R. Xue, Z. C. Zuo, H. B. Liu and Y. L. Li, *Chem Rev*, 2018, **118**, 7744-7803.

209. K. F. Mak, C. Lee, J. Hone, J. Shan and T. F. Heinz, *Phys Rev Lett*, 2010, **105**, 136805.

210. A. M. van der Zande, P. Y. Huang, D. A. Chenet, T. C. Berkelbach, Y. M. You, G. H. Lee, T. F. Heinz, D. R. Reichman, D. A. Muller and J. C. Hone, *Nat Mater*, 2013, **12**, 554-561.

211. Y. Wang, R. Fullon, M. Acerce, C. E. Petoukhoff, J. Yang, C. G. Chen, S. N. Du, S. K. Lai, S. P. Lau, D. Voiry, D. O'Carroll, G. Gupta, A. D. Mohite, S. D. Zhang, H. Zhou and M. Chhowalla, *Adv Mater*, 2017, **29**, 1603995.

212. W. J. Zhao, R. M. Ribeiro and G. Eda, *Accounts Chem Res*, 2015, **48**, 91-99.

213. R. Kappera, D. Voiry, S. E. Yalcin, B. Branch, G. Gupta, A. D. Mohite and M. Chhowalla, *Nat Mater*, 2014, **13**, 1128-1134.

214. U. Dasgupta, S. Chatterjee and A. J. Pal, *Sol Energ Mat Sol C*, 2017, **172**, 353-360.

215. B. Peng, G. N. Yu, Y. W. Zhao, Q. Xu, G. C. Xing, X. F. Liu, D. Y. Fu, B. Liu, J. R. S. Tan, W. Tang, H. P. Lu, J. L. Xie, L. J. Deng, T. C. Sum and K. P. Loh, *Acs Nano*,

2016, **10**, 6383-6391.

216. H. P. Komsa and A. V. Krasheninnikov, *Phys Rev B*, 2015, **91**, 125304.

217. Y. Xu and M. A. A. Schoonen, *Am Mineral*, 2000, **85**, 543-556.

218. R. N. Dai, Y. Y. Wang, J. Wang and X. Y. Deng, *Chemsuschem*, 2017, **10**, 2869-2874.

219. H. Liu, A. T. Neal, Z. Zhu, Z. Luo, X. F. Xu, D. Tomanek and P. D. Ye, *Acs Nano*, 2014, **8**, 4033-4041.

220. J. Kim, S. S. Baik, S. H. Ryu, Y. Sohn, S. Park, B. G. Park, J. Denlinger, Y. Yi, H. J. Choi and K. S. Kim, *Science*, 2015, **349**, 723-726.

221. M. Batmunkh, M. Bat-Erdene and J. G. Shapter, *Adv Mater*, 2016, **28**, 8586-8617.

222. A. Jain and A. J. H. McGaughey, *Sci Rep-Uk*, 2015, **5**, 8501.

223. B. C. Deng, V. Tran, Y. J. Xie, H. Jiang, C. Li, Q. S. Guo, X. M. Wang, H. Tian, S. J. Koester, H. Wang, J. J. Cha, Q. F. Xia, L. Yang and F. N. Xia, *Nat Commun*, 2017, **8**, 14474.

224. L. K. Li, Y. J. Yu, G. J. Ye, Q. Q. Ge, X. D. Ou, H. Wu, D. L. Feng, X. H. Chen and Y. B. Zhang, *Nat Nanotechnol*, 2014, **9**, 372-377.

225. B. Liu, M. Q. Long, M. Q. Cai and J. L. Yang, *Appl Phys Lett*, 2018, **112**, 043901.

226. B. Liu, M. Q. Long, M. Q. Cai and J. L. Yang, *J Phys Chem Lett*, 2018, **9**, 4822-4827.

227. X. Tong, F. Lin, J. Wu and Z. M. M. Wang, *Adv Sci*, 2016, **3**, 1500201.

228. D. P. Guo, J. G. Yu, K. Fan, H. Y. Zou and B. W. He, *Sol Energ Mat Sol C*, 2017, **159**, 518-525.

229. Z. H. Liu, M. Zhang, X. B. Xu, L. L. Bu, W. J. Zhang, W. H. Li, Z. X. Zhao, M. K.

Wang, Y. B. Cheng and H. S. He, *Dalton T*, 2015, **44**, 3967-3973.

230. Z. W. Ren, J. Wang, Z. X. Pan, K. Zhao, H. Zhang, Y. Li, Y. X. Zhao, I. Mora-Sero, J. Bisquert and X. H. Zhong, *Chem Mater*, 2015, **27**, 8398-8405.

231. E. Nouri, Y. L. Wang, Q. Chen, J. J. Xu, G. Paterakis, V. Dracopoulos, Z. X. Xu, D. Tasis, M. R. Mohammadi and P. Lianos, *Electrochim Acta*, 2017, **233**, 36-43.

232. N. Wijeyasinghe, A. Regoutz, F. Eisner, T. Du, L. Tsetseris, Y. H. Lin, H. Faber, P. Pattanasattayavong, J. H. Li, F. Yan, M. A. McLachlan, D. J. Payne, M. Heeney and T. D. Anthopoulos, *Adv Funct Mater*, 2017, **27**, 1701818.

233. S. Guarnera, A. Abate, W. Zhang, J. M. Foster, G. Richardson, A. Petrozza and H. J. Snaith, *J Phys Chem Lett*, 2015, **6**, 432-437.

234. A. Agresti, S. Pescetelli, B. Taheri, A. E. D. Castillo, L. Cina, F. Bonaccorso and A. Di Carlo, *Chemsuschem*, 2016, **9**, 2609-2619.

235. B. B. Li, Y. F. Li, C. Y. Zheng, D. Q. Gao and W. Huang, *Rsc Adv*, 2016, **6**, 38079-38091.

236. S. F. Pei, J. P. Zhao, J. H. Du, W. C. Ren and H. M. Cheng, *Carbon*, 2010, **48**, 4466-4474.

237. L. Najafi, B. Taheri, B. Martin-Garcia, S. Bellani, D. Di Girolamo, A. Agresti, R. Oropesa-Nunez, S. Pescetelli, L. Vesce, E. Calabro, M. Prato, A. E. D. Castillo, A. Di Carlo and F. Bonaccorso, *Acs Nano*, 2018, **12**, 10736-10754.

238. G. Volonakis and F. Giustino, *J Phys Chem Lett*, 2015, **6**, 2496-2502.

239. S. J. Zhang, P. Audebert, Y. Wei, A. Al Choueiry, G. Lanty, A. Brehier, L. Galmiche, G. Clavier, C. Boissiere, J. S. Lauret and E. Deleporte, *Materials*, 2010, **3**, 3385-3406.

240. J. Jagielski, S. Kumar, W. Y. Yu and C. J. Shih, *J Mater Chem C*, 2017, **5**, 5610-5627.

241. L. T. Dou, A. B. Wong, Y. Yu, M. L. Lai, N. Kornienko, S. W. Eaton, A. Fu, C. G. Bischak, J. Ma, T. N. Ding, N. S. Ginsberg, L. W. Wang, A. P. Alivisatos and P. D. Yang, *Science*, 2015, **349**, 1518-1521.

242. J. X. Liu, J. Leng, K. F. Wu, J. Zhang and S. Y. Jin, *J Am Chem Soc*, 2017, **139**, 1432-1435.

243. M. Safdari, P. H. Svensson, M. T. Hoang, I. Oh, L. Kloo and J. M. Gardner, *J Mater Chem A*, 2016, **4**, 15638-15646.

244. N. Zhou, Y. H. Shen, L. Li, S. Q. Tan, N. Liu, G. H. J. Zheng, Q. Chen and H. P. Zhou, *J Am Chem Soc*, 2018, **140**, 459-465.

245. X. Zhang, X. D. Ren, B. Liu, R. Munir, X. J. Zhu, D. Yang, J. B. Li, Y. C. Liu, D. M. Smilgies, R. P. Li, Z. Yang, T. Q. Niu, X. L. Wang, A. Amassian, K. Zhao and S. Z. F. Liu, *Energ Environ Sci*, 2017, **10**, 2095-2102.

246. Y. H. Hu, J. Schlipf, M. Wussler, M. L. Petrus, W. Jaegermann, T. Bein, P. Muller-Buschbaum and P. Docampo, *Acs Nano*, 2016, **10**, 5999-6007.

247. L. L. Mao, C. C. Stoumpos and M. G. Kanatzidis, *J Am Chem Soc*, 2019, **141**, 1171-1190.

248. S. Ma, M. L. Cai, T. Cheng, X. H. Ding, X. Q. Shi, A. Alsaedi, T. Hayat, Y. Ding, Z. Tan and S. Y. Dai, *Sci China Mater*, 2018, **61**, 1257-1277.

249. E. Nouri, M. R. Mohammadi and P. Lianos, *Carbon*, 2018, **126**, 208-214.

250. G. D. Niu, X. D. Guo and L. D. Wang, *J Mater Chem A*, 2015, **3**, 8970-8980.

251. G. Volonakis and F. Giustino, *Adv Mater Interfaces*, 2018, **5**, 1800496.

252. D. H. Cao, C. C. Stoumpos, O. K. Farha, J. T. Hupp and M. G. Kanatzidis, *J Am Chem Soc*, 2015, **137**, 7843-7850.

253. A. R. b. M. N. Yusoff, M. K., *Adv. Energy Mater.*, 2017, **8**, 1702073.

254. L. Etgar, *Energ Environ Sci*, 2018, **11**, 234-242.

255. D. S. Yu, Y. Yang, M. Durstock, J. B. Baek and L. M. Dai, *Acs Nano*, 2010, **4**, 5633-5640.

256. M. J. Deka, U. Baruah and D. Chowdhury, *Mater Chem Phys*, 2015, **163**, 236-244.

257. D. Kiriya, M. Tosun, P. D. Zhao, J. S. Kang and A. Javey, *J Am Chem Soc*, 2014, **136**, 7853-7856.